Alma Mater Studiorum · Università di Bologna

Scuola di Scienze
Corso di Laurea Magistrale in Fisica

STUDY OF THE SENSITIVITY OF THE XENON1T EXPERIMENT WITH THE PROFILE LIKELIHOOD METHOD

Relatore:
Dott. Marco Selvi

Presentata da:
Pietro Di Gangi

Correlatori:
Prof.ssa Gabriella Sartorelli
Dott. Fabio Valerio Massoli

Sessione III
Anno Accademico 2013/2014

Studio della sensibilità dell'esperimento XENON1T con il metodo Profile Likelihood

PIETRO DI GANGI

Abstract

Oggi sappiamo che la materia ordinaria rappresenta solo una piccola parte dell'intero contenuto in massa dell'Universo. L'ipotesi dell'esistenza della Materia Oscura, un nuovo tipo di materia che interagisce solo gravitazionalmente e, forse, tramite la forza debole, è stata avvalorata da numerose evidenze su scala sia galattica che cosmologica. Gli sforzi rivolti alla ricerca delle cosiddette WIMPs (Weakly Interacting Massive Particles), il generico nome dato alle particelle di Materia Oscura, si sono moltiplicati nel corso degli ultimi anni.

L'esperimento XENON1T, attualmente in costruzione presso i Laboratori Nazionali del Gran Sasso (LNGS) e che sarà in presa dati entro la fine del 2015, segnerà un significativo passo in avanti nella ricerca diretta di Materia Oscura, che si basa sulla rivelazione di collisioni elastiche su nuclei bersaglio. XENON1T rappresenta la fase attuale del *progetto XENON*, che ha già realizzato gli esperimenti XENON10 (2005) e XENON100 (2008 e tuttora in funzione) e che prevede anche un ulteriore sviluppo, chiamato XENONnT.

Il rivelatore XENON1T sfrutta circa 3 tonnellate di xeno liquido (LXe) e si basa su una Time Projection Chamber (TPC) a doppia fase. Dettagliate simulazioni Monte Carlo della geometria del rivelatore, assieme a specifiche misure della radioattività dei materiali e stime della purezza dello xeno utilizzato, hanno permesso di predire con accuratezza il fondo atteso.

In questo lavoro di tesi, presentiamo lo studio della sensibilità attesa per XENON1T effettuato tramite il metodo statistico chiamato Profile Likelihood (PL) Ratio, il quale nell'ambito di un approccio frequentista permette un'appropriata trattazione delle incertezze sistematiche.

In un primo momento è stata stimata la sensibilità usando il metodo semplificato Likelihood Ratio che non tiene conto di alcuna sistematica. In questo modo si è potuto valutare l'impatto della principale incertezza sistematica per XENON1T, ovvero quella sulla emissione di luce di scintillazione dello xeno per rinculi nucleari di bassa energia, chiamata $\mathcal{L}_{eff}$.

I risultati conclusivi ottenuti con il metodo PL indicano che XENON1T sarà in grado di migliorare significativamente gli attuali limiti di esclusione di WIMPs; la massima sensibilità raggiunge una sezione d'urto $\sigma = 1.2 \times 10^{-47}$ cm^2 per una massa di WIMP di 50 GeV/c^2 e per una esposizione nominale di 2 tonnellate $\cdot$ anno. I risultati ottenuti sono in linea con l'ambizioso obiettivo di XENON1T di abbassare gli attuali limiti sulla sezione d'urto, σ, delle WIMPs di due ordini di grandezza. Con tali prestazioni, e considerando 1 tonnellata di LXe come massa fiduciale, XENON1T sarà in grado di superare gli attuali limiti (esperimento LUX, 2013) dopo soli 5 giorni di acquisizione dati.

Contents

Introduction

The knowledge of the physical reality that surrounds and permeates us has always been paved of intriguing and challenging questions. Astrophysics is definitely one of the most fascinating search fields, not just for physicists, where a lot of topics are still not fully understood.

During last century, early as the measurements of unexpected rotational velocities of the Coma galaxy cluster, we became aware that with the known physics we are able to explain only a minimum part of the whole Universe composition. Nowadays, the scientific community agrees that the ordinary matter can not account for the total mass content of the Universe. Starting from this open question, remarkable efforts have been directed towards the search for the so-called **Dark Matter** (DM), a new "corpuscle" interacting with ordinary matter only through gravitation and, we hope, weak interaction. Indeed the number of experiments aimed at detecting Dark Matter has continuously grown in the last decades.

The present work is dedicated to the evaluation of the experimental sensitivity of one of the most promising DM experiments: **XENON1T**.

In the first part of this thesis, we review the main stages of the search for Dark Matter, along with the present state-of-art of experimental and theoretical achievements. The astrophysical evidences, from both galactic and cosmological scales, which led to the belief in the Dark Matter existence, are described in section 1.1. The composition of Dark Matter is still quite uncertain, even though there are strong indications for DM to be non-baryonic; several candidate particles have been proposed within different theoretical frameworks: Standard Model (SM) and theories beyond SM, such as SUSY and Extra dimensions models (section 1.2).

The experimental research follows two techniques of Dark Matter detection: direct and indirect. The former aims at detecting scatterings of Dark Matter particles off target nuclei, while the indirect strategy relies on DM annihilation products. A general overview of the current Dark Matter experiments and of their main results is provided in section 1.3.

A particular focus is dedicated to the experiments of the *XENON project* (chapter 2). The first one was XENON10, started in 2005; it was replaced in 2008 with XENON100, which obtained the best sensitivity to Dark Matter signals in 2012, and it is still currently in operation at the Laboratori Nazionali del Gran Sasso (LNGS). XENON1T is the upcoming upgrade of XENON100, whose construction started in 2013 and the first science run is expected by the

end of 2015.

The detection principle is based on a dual phase *Time Projection Chamber* (TPC) filled with ultra-pure xenon in liquid phase (LXe), with a small gap of gaseous xenon (GXe) on the top of the TPC (section 2.1). Xenon is an excellent scintillator medium, ideal to detect rare scattering events; the scintillation light is collected by two arrays of Photo Multiplier Tubes (PMTs) placed on the two opposite ends of the TPC. The interactions of particles in xenon produce also ionization; by applying an electric field the electrons can be drifted towards the gas region on the top, and here be extracted and accelerated to produce a second signal through proportional scintillation. This kind of technology has been demonstrated to be the most powerful in the direct search for Dark Matter.

The interaction of DM with ordinary matter is characterized by very small cross sections; hence an extremely low background level is mandatory as well as a large target mass. The XENON1T experiment has been designed to fulfill both this two requirements.

The second part of the present work addresses the study of the **XENON1T sensitivity**, which is a key task in order to assess the expected detector performance and the power in rejecting very small DM cross section values if no valid signals will be observed. Chapter 3 introduces the theoretical framework of statistical hypothesis tests on which the sensitivity calculation is based.

A first application of the precepts described in chapter 3 is presented through the study of a simplified unidimensional model (chapter 4). Our computational implementation is compared, in section 4.4, with the results obtained using the *RooStats* statistical tool distributed in the ROOT software.

The complete XENON1T statistical model, whose ingredients are extensively described in chapter 5, is finally studied in chapter 6. The expected DM interaction rate is computed in section 5.1, while the estimates of the level and the energy spectra of background sources are presented in section 5.2. XENON100 already demonstrated a high discrimination power between electromagnetic (ER) and nuclear (NR) recoils (section 2.1.3). Dark Matter particles are expected to produce only NR, i.e. scatterings off xenon atoms involving the nucleus (while in ER events orbital electrons are interested). Therefore, the ER background can be strongly dropped through such discrimination and this represents one of the key features of the detection technique based on a dual phase TPC.

However, in our statistical analysis the ER events are not removed by applying a hard discrimination cut; on the contrary we evaluate the sensitivity taking advantage of the **Profile Likelihood** (PL) Ratio method, where we can properly treat such events introducing an observable, called *discrimination parameter* (Y), that accounts for the different behavior of ER and NR events. We thus define a bi-dimensional statistical model (section 6.1), whose observables are the *S1 signal*, expressed as number of photoelectrons detected by the PMTs and related to the recoil energy of the events, and the aforementioned Y. The conversion of the recoil energy

into the S1 signal, described in section 5.3, mainly depends on the xenon target performance as scintillator, which is parametrized through the relative scintillation efficiency for NR, called $\mathcal{L}_{eff}$.

The sensitivity of XENON1T is first estimated in section 6.2 using the Likelihood Ratio (LR) method, a simplified version of the Profile Likelihood, where no systematic uncertainties are taken into account. Then, in section 6.3 the full Profile Likelihood analysis is developed, where we introduce a *nuisance parameter* to model $\mathcal{L}_{eff}$, the main systematic uncertainty for the XENON1T experiment. We also argue the impact of systematics on the experimental sensitivity by comparing the LR and PL results.

The results achieved in this work are gathered in the conclusive chapter and discussed in the context of the whole scenario of direct Dark Matter search.

Chapter 1

The Dark Matter quest

First evidences for the Dark Matter (DM) existence came from Zwicky observations of the Coma and Virgo clusters in the early 1930s. He found that the velocity of the galaxies were about one order of magnitude higher than the expected one, as if there were non luminous mass acting on the gravitational field. After Zwicky studies, other evidences sustaining the DM hypothesis were found: anomalies in the rotational curves of spiral galaxies, lensing effects, CMB anisotropies, etc. Triggered by such experimental results, a new campaign of search began with the final goal to "enlighten" this, apparently, new kind of non luminous matter called **Dark Matter**.

Many hypotheses have been formulated about DM properties. Currently it seems that the most viable candidates for this kind of matter rise from extensions of the particle Standard Model (SM). Such candidates are grouped under the common name of **Weakly Interacting Massive Particles** (WIMPs) that already introduces some of their characteristics. Indeed, such matter has to have only gravitational and weak interactions, thus being "Weakly Interacting", and it has to be massive, thus being made of "Massive Particles". The most quoted candidate as WIMP comes from the Supersymmetry: the *neutralino*.

Several experiments have been realized in the last years aiming at the discovery of the Dark Matter. They can be based on two different techniques: *direct* and *indirect* detection, both allowing to search and test different values for the theoretical parameters which define the DM properties.

1.1 Dark Matter evidences

As said, during his studies on the Coma Cluster [1], figure 1.1, Zwicky faced gravitational problems while he was trying to measure its mass.

A cluster is a set of galaxies that move together inside their own gravitational field. The dynamics of such objects is very complex and usually there is not a real center around which the galaxies move. In order to measure the mass of the Coma cluster, Zwicky first determined

Figure 1.1: The Coma Cluster, which provided the first evidence for Dark Matter. This image combines data from the Spitzer Space Telescope with the Sloan Digital Sky Survey to show many of the thousands of galaxies in the Coma cluster.

the galaxy velocities inside of it, by measuring the Doppler effect of their spectra. After that, using the Virial Theorem, he was able to extract the gravitational force acting on each one of them and, finally, to obtain the mass of the system. Then, he measured the total light output of the cluster to determine the light to mass ratio. Comparing this value to the one from the nearby Kapteyn stellar system, he found a value for the Coma cluster that was 100 times lower compared to a single Kapteyn star.

Since Zwicky's results, other experimental observations showed a discrepancy with respect to what expected from a universe without the Dark Matter:

- anomalies in the rotational curves of spiral galaxies;
- observations of the Bullet Cluster;
- gravitational lensing effects;
- anisotropies in the Cosmological Microwave Background (CMB);
- numerical simulations of the structure formation.

1.1.1 Galaxy scale evidences

Spiral galaxies, such as the Milky Way, are excellent probes to test the DM hypothesis. Such systems are said *rotationally sustained* since, for them, it is possible to define a clear rotational motion. To measure the velocity distribution until the edge of a galaxy, different techniques can be used depending on the used probe; for instance, the velocity of the hydrogen clouds is evaluated by measurements of the 21 cm line of the neutral hydrogen (HI), exploiting its low level of absorption in the interstellar medium. Usually, spiral galaxies are considered as made of a central core (disk+bulge), which is supposed to contain almost all the galaxy mass, and of an outer region. Their motion is described as a rigid body, hence, following the Newtonian

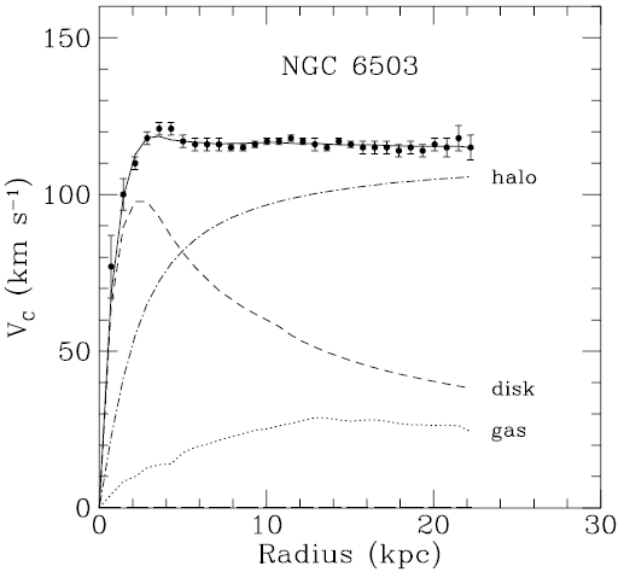

Figure 1.2: Velocity distribution of the dwarf spiral galaxy NGC 6503 [2], located in the region of space called the Local Void. The black dots are the observation results, while the dashed line is the expected shape from the only disk contribution. The contribution from the galaxy gas (dotted line) and halo (dash-dotted line) are also reported.

gravitational law, the velocity distribution is given by

$$v(r) = \sqrt{\frac{GM(r)}{r}}\,, \tag{1.1}$$

where

$$M(r) = 4\pi \int \rho(r) r^2 \mathrm{d}r \tag{1.2}$$

is the mass inside a radius r. If we consider $M(r) = \text{const}$ outside the core of the galaxy, we have

$$v(r) \propto r^{-1/2}\,. \tag{1.3}$$

However, experimental data show that, outside the disk and much beyond, the velocity distribution no longer follows the expected behavior, but it remains constant (see figure 1.2). Such evidence points out the presence of matter (physical entity gravitationally interacting) characterized by a density that scales with the root square of the distance: $\rho \propto r^{1/2}$.

Such result is explained assuming that the spiral galaxies are enclosed in dark halos with a matter distribution that expands much beyond the distribution of the luminous matter and whose effect dominates in the outer region of the galaxies. One of the most popular density profile for the Dark Matter halos is the Navarro-Franck-White (NFW) profile [3]:

$$\rho(r) = \frac{\rho_s}{(r/r_s)(1 + r/r_s)^2}\,, \tag{1.4}$$

where r_s is the halo scale radius and ρ_s is the characteristic density. This formulation reproduces quite well the simulated halos structures in the *Cold Dark Matter* (CDM) models for a quite large range of masses ($3 \cdot 10^{11} \leq M_{vir}/(h^{-1}M_\odot) \leq 3 \cdot 10^{15}$).

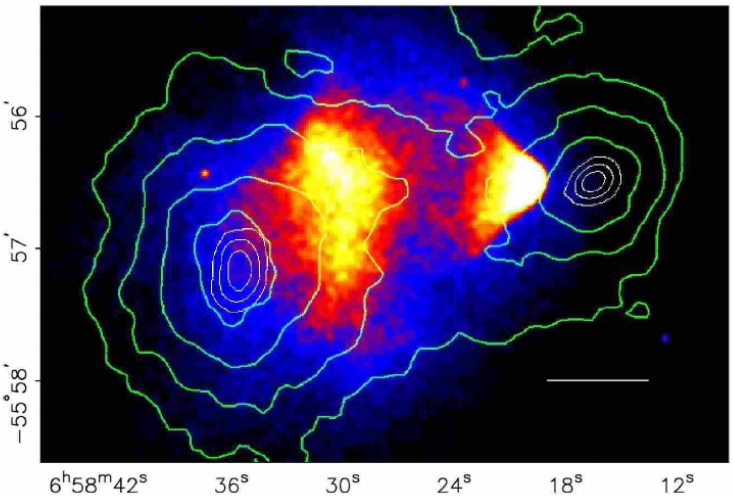

Figure 1.3: X-Ray image of the Bullet Cluster. The mass distribution from weak lensing measurements (green lines) is shown together with the baryonic matter distribution (red points). The putative Dark Matter distribution is drawn as the blue region.

1.1.2 The Bullet Cluster

Other strong evidences for the DM existence come from the study of the Bullet Cluster (1E0657-558) [4], figure 1.3. It is composed by two clusters that are passing through each other. Both of them have a stellar and gaseous component that interact in different ways: the stellar component is slowed down by the gravitational field of the other cluster while the two gaseous components behave as a fluid. The gas interactions result in a X-ray emission that can be measured and used to trace the baryonic matter distribution.

Experimental measurements show up a discrepancy between the baryonic matter distribution, measured from the X-ray emission (red points in figure 1.3), and the gravitational field distribution obtained from lensing measurements (green lines). The blue points in figure 1.3 represent the hypothetical Dark Matter distribution.

The hypothesized Dark Matter distribution, drawn in figure 1.3, is based on its characteristics of weak interaction, which let DM particles to pass through each other without being disturbed along their path. Conversely, this is not the case for the hot gas and stellar component. As the Dark Matter can continue to move on its trajectory, it is placed in the outer region of the Bullet Cluster.

1.1.3 The Microlensing effect

Several studies on the Dark Matter abundance and composition have been based on the *microlensing* effect. Generally speaking, the lensing effect can take place whenever between a distant observed object and the observer there is a source of gravitational field (such as stars, galaxy clusters, etc.) intense enough to bend the light along the path from the source to the observer. The matter distribution which generates the gravitational field represents "the lens". As a result of the lensing effect, the observer can see multiple images or a distorted image of a

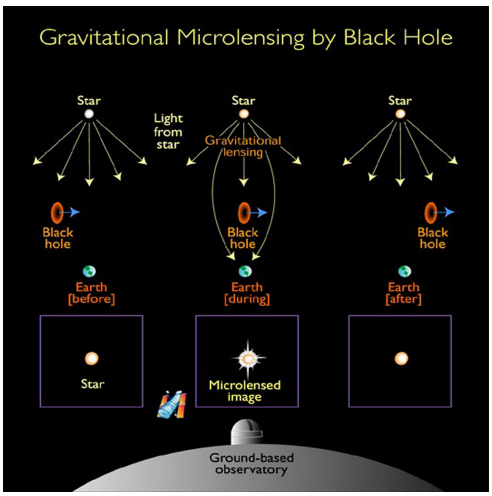

Figure 1.4: Illustration of the *microlensing* effect, i.e. the magnification of a light source due to a astrophysical bodies acting as gravitational lens.

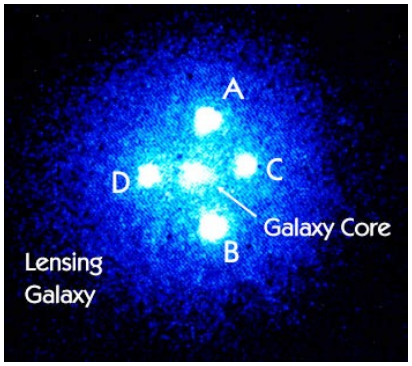

Figure 1.5: Image of the gravitationally lensed quasar called *Einstein Cross* (Q2237+030). Four images of the same distant quasar appears. This is an example of *strong lensing*.

unique source.

The microlensing effect was used to test the hypothesis that the DM was made of the so called MAssive Compact Halo Objects (MACHOs) i.e. astronomical bodies, as brown dwarfs or black holes, intended as the main component of Dark Matter. Such an effect is observed for lenses with small masses ($10^{-6} \leq M/M_{\odot} \leq 10^{6}$) in systems that extent on the kpc scale.

Unlike the *Strong Lensing*, where multiple images of the source are observed (as in figure 1.5), in the microlensing what is observed is a time modulation of the luminosity curve of the source due to the relative motion between it and the lens (an illustration is given in figure 1.4). Hence, the observed luminosity is

$$L = \mu(t)\hat{L}\,, \tag{1.5}$$

where $\hat{L}$ is the intrinsic luminosity of the source and $\mu(t)$ is the magnification due to the lens.

In microlensing studies it is usually defined a quantity called *optical depth* (τ), used to quantify the probability of a background source to be lensed. The optical depth is defined as

$$\tau = \frac{1}{\delta\Omega}\int \mathrm{d}V n(D_L)\pi\theta_E^2\,, \tag{1.6}$$

where $\delta\Omega$ is the observation solid angle, $n(D_L)$ is the micro-lens density as function of the lens distance (D_L) and $\pi\theta_E^2$ is the micro-lens cross section (with $\theta_E = \sqrt{\frac{4GM}{c^2}\frac{D_{LS}}{D_L D_S}}$, being the so-called Einstein radius). Assuming a flat space-time and constant density along the line of sight, we have

$$\tau \approx \frac{2\pi}{3}\frac{G\rho}{c^2}D_S^2\,, \tag{1.7}$$

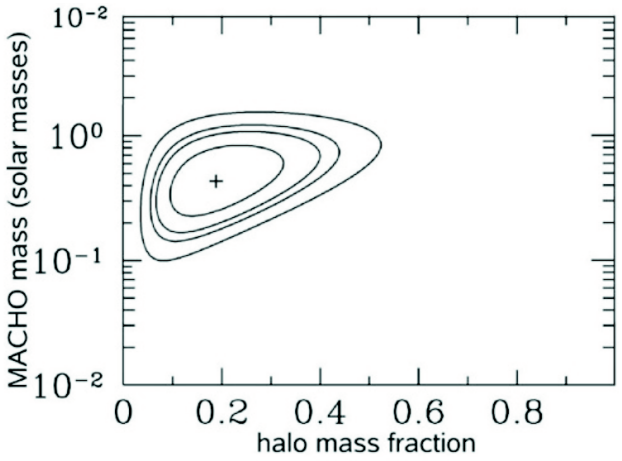

Figure 1.6: Likelihood contours obtained from the MACHO experiment [5]. The abscissa is the fraction of the halo mass contained in MACHOs, the ordinate is the MACHO mass. The contours shown correspond to the 60%, 90%, 95% and 99% confidence level.

where D_S is the source distance. For a galaxy like the Milky Way one finds

$$v^2 \approx \frac{GM_g}{r} \rightarrow M_g = \frac{rv^2}{G} \tag{1.8}$$

and

$$\rho \approx \frac{3M_g}{4\pi r^3} \approx \frac{3}{4\pi G}\left(\frac{v}{r}\right)^2 . \tag{1.9}$$

Thus, the optical depth is given by

$$\tau \approx \frac{1}{2}\left(\frac{v}{r}\right)^2 . \tag{1.10}$$

For the Milky Way $\tau \approx 10^{-6}$. This means that roughly one out of a million stars in the nearby galaxies would be lensed. In this way, counting the micro-lenses in a particular direction it is possible to characterize the lens population. The possibility of detect such events depends on their duration (the Einstein crossing time). This is determined by the transverse velocity $v_\perp$ and by the lens mass. For micro-lenses in the halo of the galaxy ($D_L \sim 10$ kpc) with velocity ~ 200 km/s, one has

$$t_E \approx 6 \cdot 10^6 \ s\left(\frac{M}{M_\odot}\right)^{0.5} \approx 0.2 \text{ yr}\left(\frac{M}{M_\odot}\right)^{0.5} . \tag{1.11}$$

If all events had the same time scale, then the number of expected events, N, in the monitoring time Δt is

$$N = \frac{2}{\pi} n\tau \frac{\Delta t}{t_E} , \tag{1.12}$$

where n is the total number of considered sources.

Several research groups worked on the identification of lenses in the Milky Way's halo looking at sources in the Large and Small Magellanic Clouds (LMC and SMC). After the analysis of

Figure 1.7: Image of the M31 galaxy.

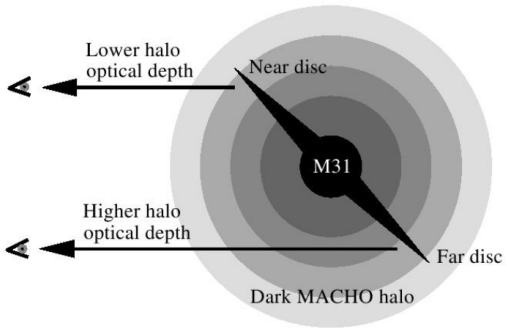

Figure 1.8: representation of the M31 galaxy as seen from the Milky Way.

data collected during several years [5], few microlensing events were observed, leading to the conclusion that MACHOs can account only for less than 20% of the halo mass, figure 1.6.

New observation campaigns are currently on going aiming at the observation of microlensing events in the M31 galaxy (Andromeda galaxy). Due to its larger distance compared to the L/SMC galaxies, it is not possible to distinguish single stars and this drastically changes the observation strategy. In this case, the total luminosity of the galaxy should change and, consequently, only high magnification events gives appreciable signal. There are several advantages in looking at M31: due to its inclination along the line of sight (see figure 1.7), it is possible to accurately measure its rotation curve. Moreover, the lensing effects show an asymmetry that is not possible to explain only with the stars self-lensing.

1.1.4 Cosmological scale evidences

The lensing studies showed that, even if the Dark Matter exists, it is mainly composed by *non-baryonic* matter. Further convincing experimental evidences that sustain such a scenario come from the *Cosmic Microwave Background* (CMB) power spectrum analysis, but also from the Big Bang Nucleosynthesis (BBN).

The Cosmic Microwave Background, discovered by Arno Penzias and Robert Wilson in 1964 [6], provides important hints about the Dark Matter existence, composition and, in particular, about its abundance in the Universe. The CMB consists of relic photons from the early Universe stage at which the temperature dropped to about 3000 K, allowing electrons to recombine with protons. Hence, the Universe became transparent to the photons as they had not enough energy to ionize the hydrogen. The CMB almost perfectly follows an ideal black body spectrum with a temperature of $T = 2.726$ K. However, it shows temperature anisotropies (figure 1.9), at a level lower than 10^{-5}, that can give crucial information on the Universe composition. Such anisotropies stem from quantum fluctuations of the inflation fields that were stretched, at cosmological scale, during the inflation and ultimately became density

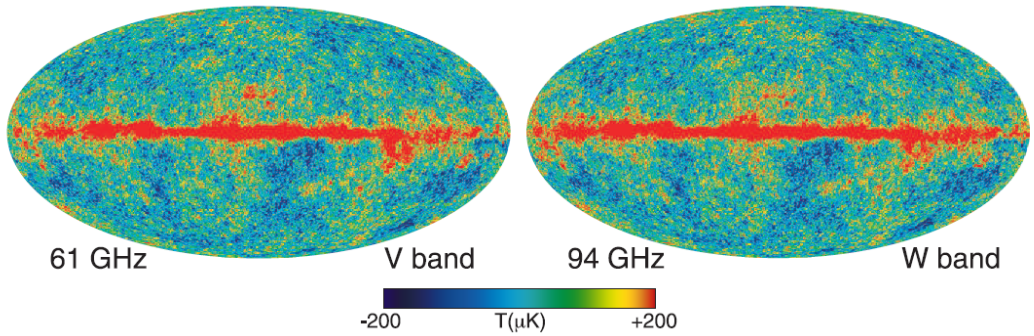

Figure 1.9: Nine-year temperature sky maps obtained by the *Wilkinson Microwave Anisotropy Probe* (WMAP) [7].

Figure 1.10: The 2013 Planck CMB temperature angular power spectrum [9]. The error bars include cosmic variance, whose magnitude is indicated by the green shaded area around the best fit model.

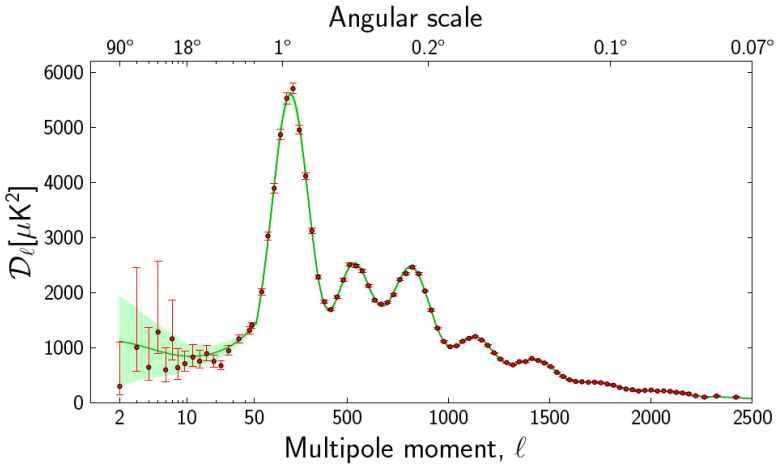

fluctuations. At that time, baryons and photons were well coupled and the latter inherited the density fluctuations as temperature fluctuations. This happened because photons coming from a region with higher density were more redshifted as they lose more energy to overcome the potential well (Sachs-Wolf effect) [8].

The CMB spectrum is characterized by a peak structure, shown in figure 1.10, as a consequence of two opposite effects: the gravitational force attracted the photons into the higher density regions, while the gas pressure pushed them apart. The angular power spectrum is obtained by decomposing the anisotropy map into spherical harmonics and taking into consideration various distortions such as emissions from galaxies. These anisotropies can be described as

$$\frac{\delta T}{T}(\theta,\phi) = \frac{T(\theta,\phi) - \langle T(\theta,\phi)\rangle}{\langle T(\theta,\phi)\rangle} = \sum_{l=2}^{+\infty}\sum_{m=-l}^{+l} a_{lm} Y_{lm}(\theta,\phi)\,, \tag{1.13}$$

where $Y_{lm}(\theta,\phi)$ are the spherical harmonics.

The size and the position of the peaks of the CMB spectrum provide valuable information on cosmological parameters, such as the curvature and the energy-matter composition of the

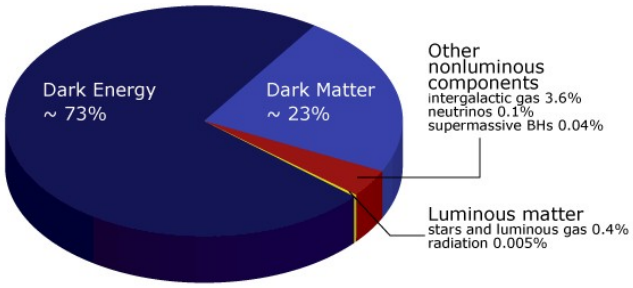

Figure 1.11: Representation of the contributions to the overall Universe content.

universe: Ω_{tot}, Ω_b and Ω_{DM}. From the CMB study [7, 10] it is then possible to extract an estimate of the non-baryonic Dark Matter abundance in the Universe:

$$\begin{aligned} \Omega_\Lambda &= 0.707 \pm 0.010\,; \\ \Omega_m &= 0.293^{\pm 0.056}_{\pm 0.010}\,; \\ \Omega_b h^2 &= 0.02211 \pm 0.00034\,; \\ \Omega_{DM} h^2 &= 0.1162 \pm 0.0020\,. \end{aligned}$$

From the values of cosmological parameters results that the dark energy, Λ, accounts for about 70% of the Universe energy content, while the majority of the matter content is in the form of non-baryonic Dark Matter (see figure 1.11).

1.2 Dark Matter candidates

While the existence of Dark Matter is a well established statement, on the other hand which are the physical constituents of DM is still an open question widely debated. Among the great variety of hypothesized DM candidates, the WIMPs draw the attention of most of the experimental research in this field, including the XENON Collaboration. Nevertheless, it is worth recalling some of the main DM candidates that have been proposed to date.

1.2.1 Baryonic Dark Matter

When talking about baryonic Dark Matter, one refers to ordinary and non-luminous matter, undetectable through direct observation. We already mentioned the MACHOs (massive and slightly luminous objects), which are intended to account for the baryonic component of the Dark Matter. Dark galactic halos are plausible sites for baryonic candidates such as *brown dwarfs* and cold clouds of *molecular hydrogen* H_2. This scenario predicts a diffuse γ-ray emission from the Milky Way's dark halo. A flux, whose properties are in a quite good agreement with the theoretical prediction, has been observed by the EGRET detector [11] mounted onto the CGRO satellite.

Nonetheless, from microlensing studies and cosmological observations, we know that the majority of the Dark Matter is non-baryonic as MACHOs can account for not more than 20% of the total Dark Matter amount.

1.2.2 Non-baryonic Dark Matter

Zeldovich hypothesized a scenario, named **Hot Dark Matter**, where the Dark Matter particles were relativistic. It implied a top-down structure formation history where the big structures came first. However, the evolution of such systems were too slow if compared with the time scale of the primordial galaxy formation. Moreover, the high energy of the DM particles was in contrast with the formation of such big structures since relativistic particles would be dispersed in the space. Nowadays, the most accepted and supported DM scenario is the **Cold Dark Matter** (CDM), in which Dark Matter is not relativistic.

First evidences for the CDM came from the N-body simulations by Jeremiah Ostriker and James Peebles [12], in the 1970s. They simulated the interactions of a distribution of mass points, that represented stars moving in a galaxy, rotating around a central point. To get the correct interactions between the mass points, they used the Newton's law. They found that, in a time less than an orbital period, most of the mass points would have collapsed to a bar-shaped dense concentration, close to the center of the galaxy, with only few mass points at larger radii. This result is clearly in contrast with the elegant spiral or elliptical shape of the galaxies that we observe. But when they added a static and uniform distribution of mass, from 3 to 10 times the size of the total mass of the mass points, they found more recognizable structures. Thus, Ostriker and Peebles had solid numerical evidence that cold Dark Matter was necessary to form the types of galaxies we observe in the universe.

In the following sections we outline the main proposals for CDM candidates arose so far. Candidate particles have hypothesized in different theoretical frameworks, starting from the Standard Model but also in the *Supersimmetry* (SUSY) and in the *Extra dimensions* models context.

1.2.3 Standard Model candidates

The Standard Model of particles offers some viable candidates in the framework of the HDM, while no SM particles seem to be able to account for the larger part of cold Dark Matter.

Relic Neutrinos

One of the first hypothesis about the non-baryonic Dark Matter composition was based on *neutrinos*. They were one of the first suggested candidates due to their "Dark Matter-like" properties: they are stable particles, interact with the ordinary matter very weakly and are massive.

From the cosmology, we have that their relic density is given by

$$\Omega_\nu h^2 = \sum_{i=1}^{3} \frac{m_i}{93 \text{ eV}} , \tag{1.14}$$

where m_i is the mass of the $i-th$ neutrino. The most stringent constraints on their masses come from the combination of PLANCK data with large scale structure information [13]:

$$\sum m_\nu < 0.18 \text{ eV (95\% CL)} . \tag{1.15}$$

Given this upper bound on the neutrino mass, the resulting relic density is not enough to explain the Dark Matter as mainly composed by them. Another reason, that explains why these particles cannot be valid DM candidates, is that being relativistic collisionless particles, neutrinos erase (moving from high to low density regions) fluctuations below a scale of ~ 40 Mpc$(m_\nu/30$ eV), called the *free-streaming* length, implying a top-down formation history of the Universe. As said, this scenario is excluded by the simulations of the structure formation history and also by the observation that our galaxy appears to be older than the Local Group and the discrepancy between the predicted late formation of galaxies, at redshift $z < 1$, and the observations of galaxies around $z > 4$ [14].

Axions Remaining in the SM scenario, the *axion* is another Dark Matter candidate. This particle is a Nambu-Goldstone boson which corresponds to the phase of a complex field, the Peccei-Quinn field, which breaks the $U(1)_{PQ}$ symmetry. The $U(1)_{PQ}$ field is a global $U(1)$ symmetry, which carries QCD anomalies, proposed by Peccei and Quinn as solution to the strong CP problem [15]. This symmetry is broken at the scale of f_a which is the axion decay constant, also called PQ scale. The relic abundance of the axions [16] can be expressed, using the QCD scale $\Lambda_{QCD} \sim 200$ MeV, as

$$\Omega_a h^2 = \theta^2 \left(\frac{f_a}{10^{12}\text{GeV}} \right)^{1.175} . \tag{1.16}$$

With $\theta \sim 0.1$ and $f_a \sim 10^{12}$ GeV axions can represent an important percentage of the CDM which might consist only of axions. They can be detected through the *Primakoff effect* where an axion is converted into a photon under a proper magnetic field. The CERN Axion Solar Telescope (CAST) [17] and the PVLAS [18] are involved in the search of these particles. While the former looks for solar axions, the latter fires polarized light through a long vacuum region with a 5.5 T magnetic field and searches for anomalous rotations of polarization; according to the theory, the vacuum becomes birefringent, thus photons with polarization aligned with the magnetic field are delayed as they are preferentially transformed into axions which travel slower than the speed of light.

The PVLAS collaboration initially claimed the detection of an irregular rotation corresponding to an axion mass of 1-1.5 meV, but retracted their results upon obtaining a null result after upgrades. The current strongest limits, on the axion mass, have been set by the XENON100 experiment [19].

1.2.4 Weakly Interacting Massive Particles (WIMPs)

Concerning SUSY, many interesting features make it attractive, including its role in understanding the fundamental distinction between bosons and fermions and the problems of hierarchy for neutrinos. In this framework, Dark Matter particles are identified with the general definition of: Weakly Interacting Massive Particles (WIMPs). They are stable, cold, non-baryonic and interact only through gravitational and weak forces.

If WIMPs are stable, there is a cosmological relic abundance produced during the Big Bang. Assuming for such particles a mass m_χ, one has that for $T > m_\chi$ they were in thermal equilibrium while at temperatures below m_χ they decoupled and their abundance started to lower. Finally, when the expansion rate of the Universe became larger than the annihilation rate ($\Gamma < H$, where H is the Hubble constant), the WIMP abundance "freezed out", resulting in the current relic abundance.

The evolution of the WIMP density is described by the Boltzmann equation

$$\frac{dn_\chi}{dt} + 3Hn_\chi = -\langle\sigma_a v\rangle[(n_\chi)^2 - (n_\chi^{eq})^2] \,, \tag{1.17}$$

where n_χ^{eq} is the number density at the thermal equilibrium and $\langle\sigma_a v\rangle$ is the thermally averaged total annihilation cross section. For massive particles (non-relativistic limit) and in the Maxwell-Boltzmann approximation, n_χ^{eq} is given by

$$n^{eq} = g\left(\frac{m_\chi T}{2\pi}\right)^{3/2} e^{-m_\chi/T} \,, \tag{1.18}$$

where g is the number of degree of freedom, m_χ the particle mass and T the temperature. As said, the "freeze-out" is verified for $\Gamma = H$ that results in a temperature $T = m_\chi/20$. Introducing the entropy density $s = 2\pi 2 g_* T^3/45$, where g_* counts the number of relativistic degrees of freedom, and using the conservation of entropy per co-moving volume, one finds

$$(n_\chi/s)_0 = (n_c hi/s)_f = \frac{H(T_f)}{\langle\sigma_a v\rangle s(T_f)} \equiv 100\frac{1}{g_*^{1/2} m_\chi m_{Pl}\langle\sigma_a v\rangle} \,, \tag{1.19}$$

where m_{Pl} is the Planck mass and the subscripts 0 and f denote the present and the freeze-out epoch, respectively. Thus, the relic density can be expressed as function of the annihilation rate:

$$\Omega_\chi h^2 = \frac{m_\chi n_\chi}{\rho_c} \equiv 3\cdot 10^{-27}\frac{\mathrm{cm}^3\mathrm{s}^{-1}}{\langle\sigma_a v\rangle} \,, \tag{1.20}$$

which is independent from m_χ.

The annihilation cross section of a new particle interacting at the weak scale can be estimated as: $\langle \sigma_a v \rangle \sim 10^{-25}$ cm^3 s^{-2}. Such value is close to the one derived from cosmological arguments. This strongly suggests that if a stable particle associated with the electro-weak scale interactions exists, then it is likely to be the dark matter particle. This coincidence has provided strong motivation for finding WIMPs.

There are several WIMP candidates; the most promising is the Lightest Supersymmetric Particle (LSP), which is the *neutralino*.

The neutralino

The Minimal Supersymmetric Standard Model (MSSM) contains the smallest possible field content necessary to give rise to all the Standard Model (SM) fields. All of the SM particles have R-parity equal to 1 and all sparticles, their superpartners, have $R = -1$. Thus, from R-parity conservation (first introduced to suppress the rate of proton decay), sparticles can only decay into an odd number of sparticles (plus Standard Model particles). The Lightest Supersymmetric Particle is, therefore, stable and can only be destroyed via pair annihilation, making it an excellent Dark Matter candidate. Among few alternatives, the most promising LSP is the lightest *neutralino*, which is uncharged under electromagnetic and strong interactions.

In the MSSM, binos ($\tilde{B}$), winos ($\tilde{W}_3$) and higgsinos ($\tilde{H}_1^0$ and $\tilde{H}_2^0$) states mix into four Majorana fermionic mass eigenstates, called neutralinos. The four neutralinos are labeled as: $\tilde{\chi}_1^0$, $\tilde{\chi}_2^0$, $\tilde{\chi}_3^0$ and $\tilde{\chi}_4^0$. The first of them is the lightest one and it is referred as the **neutralino**, $\chi = \tilde{\chi}_1^0$.

The most relevant neutralino interactions for Dark Matter searches are self *annihilation* and *elastic scattering* with nucleons. At low velocities, the leading channels for neutralino annihilations are into fermion-antifermion, gauge bosons pairs and final states containing Higgs bosons.

All the possible annihilation processes are of interest for indirect Dark Matter searches (section 1.3.2), while direct detection techniques (section 1.3.1) are based on the elastic scattering processes. The WIMP interaction with the matter can be divided into two types: spin-independent (SI) and spin-dependent (SD). A scalar interaction, i.e. SI, with quarks can be expressed as

$$\mathcal{L}_{scalar} = a_q \overline{\chi}\chi\overline{q}q \,, \tag{1.21}$$

where a_q is the WIMP-quark coupling. The scattering cross section is given by

$$\sigma_{scalar} = \frac{4m_r^2}{\pi} f_{p,n}^2 \,, \tag{1.22}$$

where m_r is the reduced mass of the nucleon and $f_{p,n}$ is the coupling to protons and neutrons. The total scalar cross section for interactions with a nucleus, in the case of zero transfer

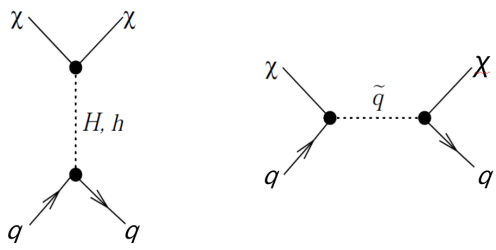

Figure 1.12: Feynman diagrams for neutralino-quark scalar (**spin-independent**) elastic scattering interactions [20].

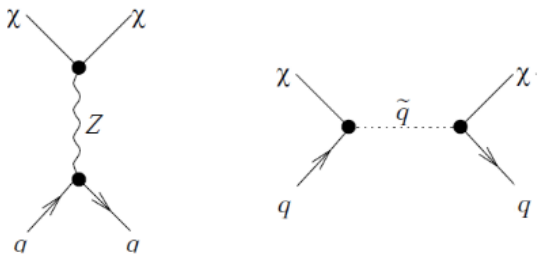

Figure 1.13: Feynman diagrams for neutralino (**spin-dependent**) axial-vector interactions [20].

momentum, is given by the sum over all the nucleons:

$$\sigma = \frac{4m_r^2}{\pi}\Big(Zf_p + (A-Z)f_n\Big)^2 . \tag{1.23}$$

A spin-dependent interaction, i.e. axial-vector interaction, between WIMPs and quarks can be expressed as

$$\mathcal{L}_{AV} = d_q \overline{\chi}\gamma^\mu\gamma_5\chi\overline{q}\gamma^\mu\gamma_5 q \,, \tag{1.24}$$

where d_q is the generic coupling. The Feynman diagrams for both SI and SD neutralino interactions are shown in figures 1.12 and 1.13.

The cross section for SD interactions is given by [21]

$$\frac{d\sigma}{d|\vec{v}|^2} = \frac{1}{2\pi v^2}\overline{|T(v^2)|^2} \,, \tag{1.25}$$

where v is the WIMP velocity relative to the target and $T(v^2)$ is the scattering matrix element. At zero transfer momentum, one has

$$\begin{aligned}\overline{|T(0)|^2} = \frac{4(J+1)}{J}|(d_u\Delta_u^p + d_d\Delta_d^p + d_s\Delta_s^p)\langle S_p\rangle + \\ + (d_u\Delta_u^n + d_d\Delta_d^n + d_s\Delta_s^n+)\langle S_n\rangle|^2 \,,\end{aligned} \tag{1.26}$$

where J is the total nuclear spin of the target nucleus, $\Delta_{u,d,s}^{n,p}$ are the fractions of the nucleon spin carried by a given quark and $\langle S_{p,n}\rangle$ are the expectation values of the total spin of protons and neutrons, respectively. For target nuclei with even numbers of protons and neutrons, the total spin is equal to 0. Thus, for such nuclei, the spin-dependent cross section vanishes.

Another kind of interaction to be considered is the WIMP-quark vector interaction:

$$\mathcal{L}_V = b_q\overline{\chi}\gamma_\mu\chi\overline{q}\gamma_\mu q \tag{1.27}$$

where b_q is the WIMP-quark vector coupling. The zero transfer momentum cross section can be expressed as [22],

$$\sigma = \frac{m_\chi^2 m_N^2[2Zb_p + (A-Z)b_n]^2}{64\pi(m_\chi + m_N)^2} \,, \tag{1.28}$$

with $b_q = G_F(T_q^3 - 2e_q \sin^2\theta_W)/\sqrt{2}$, where G_F is the Fermi constant, T_q^3 and e_q are the weak isospin and electric change of the quark q, respectively, and θ_W is the Weinberg angle.

Sneutrino and Gravitino

In the SUSY context the *sneutrino* and *gravitino*, the superpartners of the SM neutrino and graviton, have been considered as DM candidate.

The **sneutrino** is a viable candidate if its mass were in the range [550, 2300] GeV/c^2. Despite this possibility, it has been rejected since its cross section would be higher than the current found limits.

The **gravitino** interacts only through the gravitational force and this makes it very hard to detect. The most important coupling for the gravitino is given by

$$\mathcal{L} = -\frac{1}{\sqrt{2}m_P}\mathcal{D}_\nu\phi^{i*}\overline{\tilde{\phi}}_\mu\gamma^\nu\gamma_\mu\psi^i - \frac{1}{\sqrt{2}m_P}\mathcal{D}_\nu\phi^i\overline{\psi}^i\gamma^\mu\gamma^\nu\overline{\psi}_\mu - \\ - \frac{i}{8m_P}\overline{\tilde{\psi}}_\mu[\gamma^\nu,\gamma^\rho]\gamma^\mu\tilde{\lambda}^a F^a_{\nu\rho}\,, \tag{1.29}$$

where $\tilde{\psi}_\mu$ is the gravitino field, ϕ^i and ψ^i are the complex scalar fields and the corresponding chiral fermion fields, $\tilde{\lambda}^a$ are the gaugino fields, m_P is the reduced Planck scale ($\simeq 2.44 \cdot 10^{18}$ GeV) and D_ν is the covariant derivate. Gravitinos can be produced in $2 \to 2$ processes such as scalar-fermion-gravitino or gaugino-gauge boson-gravitino vertices [23]. The relic gravitino abundance can be written as [24]

$$\Omega_{\tilde{G}}h^2 \approx 0.2\left(\frac{T_r}{10^{10}\text{ GeV}}\right)\left(\frac{100\text{ GeV}}{m_{\tilde{G}}}\right)\left(\frac{m_{\tilde{g}}(\mu)}{1\text{ TeV}}\right) \tag{1.30}$$

where $m_{\tilde{g}}$ is the gluino mass.

Axino

The *Axino*, $\tilde{a}$, is the superpartner of the axion and it is a Majorana chiral fermion. Its mass is strongly model-dependent ([1 eV, M_{SUSY}]), meaning that it could be the lightest particle, thus stable, in SUSY models. The most important couplings for $\tilde{a}$ can expressed as

$$\mathcal{L} = i\frac{3\alpha_Y C_{aYY}}{8\pi f_a}\overline{\tilde{a}}\gamma_5[\gamma^\mu,\gamma^\nu]\tilde{B}B_{\mu\nu} + i\frac{3\alpha_S}{8\pi f_a}\overline{\tilde{a}}\gamma_5[\gamma^\mu,\gamma^\nu]\tilde{g}^b F^b_{\mu\nu}\,, \tag{1.31}$$

where B and $\tilde{B}$ are the gauge and gaugino fields corresponding to $U(1)_Y$, F^b and $\tilde{g}^b$ are the gluon and gluino fields, α_Y and α_S are the $U(1)_Y$ and strong fine-structure constant and C_{aYY} is model-dependent coefficient of order of unity. A production channel for $\tilde{a}$ is the decay of non-thermal particles. An example of this process is the decay of the lightest stau mass eigenstate $\tilde{\tau}_2$.

Wimpzillas

The **Super heavy Dark Matter**, also named *wimpzillas*, has been proposed as a non-thermal Dark Matter candidate. The masses of this kind of particles range from 10^{12} up to 10^{16} GeV/c^2.

In the early Universe there were different available channels to produce such particles as the gravitational production at the end of inflation, resulting from the expansion of the background space-time. The interaction cross section of such particles with ordinary matter, covers a wide range of hypotheses, from very weak to strong coupling (in the latter case super-massive particles are sometimes called *simpzillas*).

The wimpzillas have been proposed as a first explanation for the observed ultra high energy cosmic rays, above the GZK cut-off ($\sim 5 \cdot 10^{19}$ eV). Above this energy the Universe, on cosmological scale ($\geq$ 50 Mpc), is opaque to protons. Since sources for such energetic protons have not been observed yet, a possible explanation for their existence is that they are produced in the decay or annihilation of super heavy Dark Matter particles (top-down cosmic-ray models [25]).

Kaluza-Klein particle

In the **Extra dimensions model**, the space is considered to have four dimensions needed to include electromagnetism into a "geometric" theory of gravitation. Also in this scenario, the lightest particle, called *Kaluza-Klein* (KK) particle [26], is a viable candidate for the Dark Matter.

If Standard Model particles propagate in such Extra dimensions and the KK parity is conserved, the lightest KK particle is stable, becoming an excellent candidate for DM. The mass of the first stable KK particle ranges from several hundreds of GeV up to few TeV, and can be detected via elastic scattering in the Dark Matter direct search experiments, or indirectly via annihilation products, such as positrons from the galactic halo, gamma rays from the galactic center, high energy neutrinos from the core of the Sun or the Earth, and antiproton. Due to their characteristics, a tonne-scale detector is required to detect their interactions thus, it is necessary to wait for experiments as XENON1T.

1.3 Experiments searching for WIMPs

Currently, there are several experiments aiming at detecting Dark Matter interactions with an ordinary matter target. Different choices of the detection technique and target material allow to scan different ranges of the parameter space of DM models.

The DM experiments can be divided in two main classes: *direct detection*, based on DM scatterings off target nuclei, and *indirect detection*, searching for DM particles annihilation products inside and outside the galaxy.

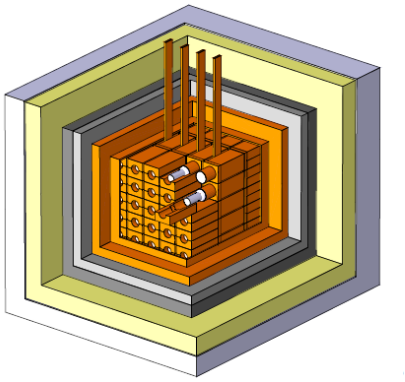

Figure 1.14: DAMA/LIBRA detector: schematic view of the 25 highly radio-pure NaI(Tl) scintillator crystals within the passive shield.

To date, the best results for WIMP masses above 8 GeV/c^2 have been obtained in 2012 by XENON100 [27], reaching the best SI limit of 2×10^{-45} cm^2 at 55 GeV/c^2 mass, and LUX [28], in 2013 with 7.6×10^{-46} cm^2 for 33 GeV/c^2 WIMPs. At lower masses, other experiments, as CoGeNT and CDMS, are more sensitive.

In the next sections we browse through the main Dark Matter experiments based on both direct and indirect detection techniques.

1.3.1 Direct detection experiments

Dark Matter interactions with ordinary nuclei are characterized by very small cross sections. The direct detection of WIMP-nucleon scatterings requires very large target masses and an extremely low level of radioactivity. Hence, an ultrapure detector is mandatory as well as its placement into underground laboratories in order to properly drop the background rate.

DAMA/LIBRA

The DAMA/LIBRA detector, placed in the LNGS underground laboratory, is the upgrade of the previous DAMA/NaI detector. Its sensitive part is made of 25 highly radio-pure NaI(Tl) crystals, each one of 9.70 kg, arranged in a 5×5 matrix.

For the Dark Matter search, the modularity of DAMA/LIBRA is very useful since WIMPs are expected to give only one interaction in the entire stuck of detectors. Moreover, the characteristics of the scintillators allow to reject noise events. With the exception of the noise rejection, in DAMA/LIBRA it is not possible to distinguish between nuclear and electromagnetic recoils. Thus, the detector can be only sensitive to the modulation of the WIMP signal, due to the Earth motion around the Sun, that is searched in the [2, 20] keV energy region.

With a total exposure of 1.04 tonne $\cdot$ years, DAMA/LIBRA has observed a signal modulation (see figure 1.15) that could be explained as due to the modulation of the Dark Matter flux [29].

The modulation of the signal, observed for 14 annual cycles (7 from DAMA/NaI and 7 from DAMA/LIBRA) has now a significance of 9.3σ. It shows a period of about 1 year and a phase

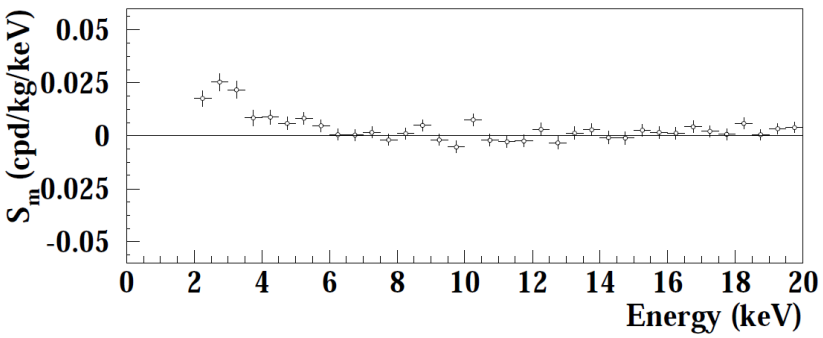

Figure 1.15: Energy distribution of the modulation amplitude S_m for the total cumulative (DAMA/LIBRA plus DAMA/NaI) exposure of 1.33 t-y obtained with maximum likelihood analysis [29].

of 144 ± 7 days. As one can see from figure 1.15, the modulate signal appears only in the low energy region, where it is expected after spin-independent scatters from light WIMP in a thermal halo model.

Several explanations for the modulation signal have been proposed to investigate a possible background as source of this signal. For example, since DAMA/LIBRA does not have a muon veto, it was hypothesized that it was the modulation of the muon flux to generate the signal [30]. However, recently it was shown that the muon flux is too low to explain the observed signal [31].

CoGeNT

The CoGeNT detector, made of one p-type point contact (PPC) Ge crystal of 440 g, is focused on the search for WIMP interactions in the [0.4, 3] keV energy region. Due to its very low energy threshold, this detector is particularly suitable for the low mass WIMP search (m_χ below $\sim$ 10 GeV/c^2). It is placed in the Soudan Underground Laboratory (SUL), at a depth of 2090 meters water equivalent (m.w.e.), to guarantee a shield against cosmic rays and their associated backgrounds. To reduce even more the background, a passive shield has been realized, figure 1.16. In order to be operative it requires a cryogenic system and for this reason, the crystal is housed in a copper cryostat.

In 2010 CoGeNT observed an excess of events [32], at low energies, in the bulk of the Ge crystal. Several analyses have been performed to explain this excess as due to Dark Matter interactions. Assuming a Maxwellian velocity distribution with $v_0 = 230$ km/sec, and $v_{esc} = 500$ km/sec for a spin-independent model, with equal coupling to protons and neutrons and without any unknown background, the WIMP hypothesis gives a nice agreement, especially in the very low energy region, with the observed data.

The best results were obtained for $m_\chi = 9.4$ GeV and $\sigma = 0.84 \times 10^{-40}$ cm^2. However, such results are excluded by other experiments such as CDMS-Si.

In the CoGeNT results from a 1129 live days run [33], a modulated signal has been observed. The period of this modulation is compatible, within the errors, with a period of one year and the t_{max} is compatible with the DAMA/LIBRA one. However, a discrepancy of a factor $\sim$4-7

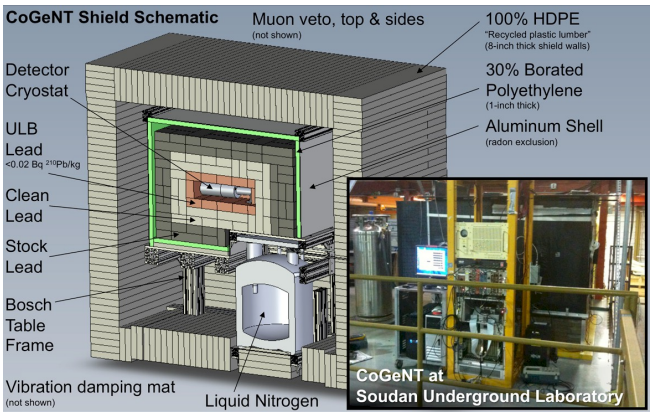

Figure 1.16: Schematic view of the CoGeNT structure with its passive shield.

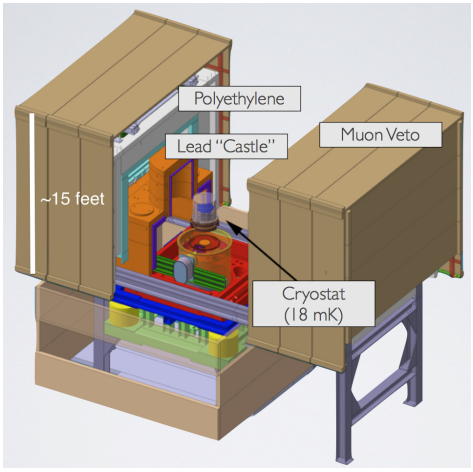

Figure 1.17: Schematic view of the EDELWEISS-II experiment.

is found for the amplitude if the signal would be given by a low mass WIMP in a standard halo model.

EDELWEISS-II

The EDELWEISS-II detector (figure 1.17), at the Laboratoire Souterrain de Modane (LSM) under 4800 m.w.e., is enclosed in a passive shield, covered by a muon veto system for thorough-going muons. The core of the detector is based on ten bolometers of hyper-pure Ge crystals of cylindrical shapes with a diameter of 70 mm and a height of 20 mm, all inside a cryostat.

For each event, two signals are recorded: one from the temperature increase, measured using neutron transmutation doped (NTD)-Ge thermometric sensors glued on each detector, and one from the charges produced in the interaction that are recorded by proper electrode wires on both side of the Ge bolometers.

In 2012, the collaboration carried out an analysis on low-energy (E<20 keV) WIMP-induced nuclear recoils [34]. For a WIMP mass of 30 GeV/c^2, three events have been found as possible candidates.The data indicated no evidence for an exponential distribution of low-energy nuclear recoils that could be attributed to WIMP elastic scattering after an exposure of 113 kg $\cdot$ days. For WIMPs of mass 10 GeV/c^2, the observation of one event in the WIMP search region results in a 90% CL limit of 1.0×10^{41} cm^2 [34] on the spin-independent WIMP-nucleon scattering cross section.

superCDMS

The superCDMS detector is a bolometer sited at the Soudan Underground Laboratory. To operate, a cryogenic system based on He-3/He-4 dilution refrigerator has been realized. The

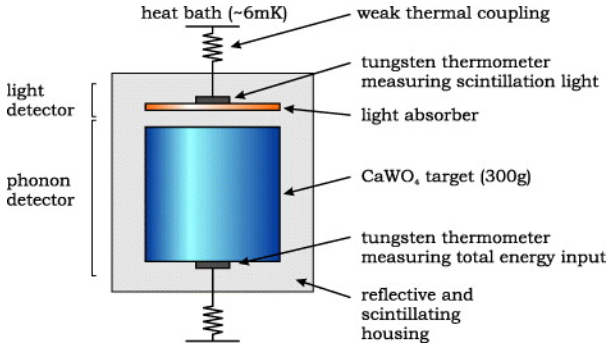

Figure 1.18: Scheme of the CRESST-II module.

core of the detector is made of fifteen 600 g Ge crystals from which it is possible to extract the phonon and the charge signals. The crystals have cylindrical shape with a diameter of 76 mm and height of 25 mm. The phonon sensor is a superconducting ^{174}W film held in the transition state from the superconducting to the normal state (therefore called Transition Edge Sensor or TES). A small change in the temperature leads to a large variation in the measured resistance. The charge sensors are made of electrodes biased at a certain voltage. For events near the surface, the charge carriers distribute between the electrode and the phonon sensors (acting as ground reference) on the same side of the detector. From the different ratio of the charges on both sides it is possible to reject events closed to the surface (usually due to background).

In 2014, the collaboration carried out the analysis of a run characterized by an exposure of 577 kg $\cdot$ days [35]. They focused on WIMP masses below 30 GeV/c^2 considering the energy search region [1.6, 10] keV. With these results, superCDMS set an upper limit on the spin-independent WIMP-nucleon cross section of 1.2×10^{-42} cm^2 for $m_\chi = 8$ GeV/c^2 [35].

CRESST-II

CRESST-II is the upgrade, placed at LNGS, of the CRESST detector that includes a new neutron shield and a muon veto. It uses simultaneously two independent detectors for revealing heat/phonon and light. The core of the detector is made of modules that consist of a $CaWO_4$ 300 g crystal, the target, and a silicon-on-sapphire (SOS) wafer used for measuring the scintillation light. In their interaction inside the crystals, WIMPs lose energy producing phonons and a small amount of scintillation light. The reading of signals from crystals and SOS is obtained by a Transition Edge Sensor (TES) attached to them. All these elements are enclosed in a reflective and scintillating case (see figure 1.18).

The use of two detectors allows for precise measurements of the deposited energy and background discrimination. For example, the electromagnetic background rejection can be achieved using the scintillation to phonon signals ratio.

In 2014, the CRESST-II collaboration has published its results from the analysis of a 29.35 kg $\cdot$ days focused on the [0.6, 40] keV energy region [36].

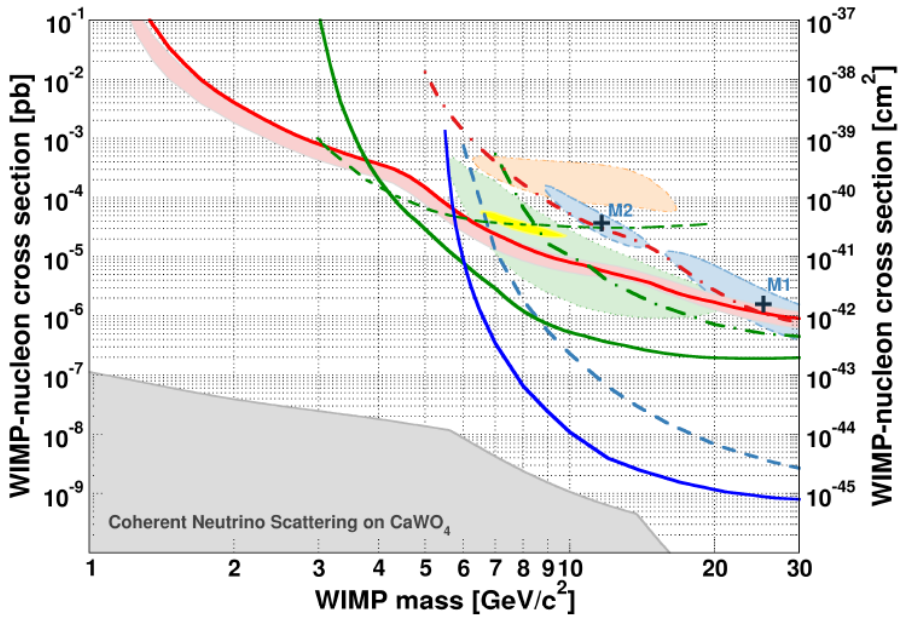

Figure 1.19: WIMP parameter space for spin-independent WIMP-nucleon scattering. The 90% C.L. upper limit (solid red) is depicted together with the expected sensitivity (1σ C.L.) from the background-only model (light red band). The CRESST 2σ contour [37] is reported in light blue. The dash-dotted red line refers to the reanalyzed data from the CRESST commissioning run [38]. In green there are the limits (90% C.L.) from Ge-based experiments: SuperCDMS [35] (solid), CDMSlite [39] (dashed) and EDELWEISS [34] (dash dotted) . The parameter space favored by CDMS-Si [40] is shown in light green (90% CL), the one favored by CoGeNT (99% CL) [41] and DAMA/Libra (3σ CL) [42] in yellow and orange. The exclusion curves from liquid xenon experiments (90% CL) are drawn in blue, solid for LUX [28], dashed for XENON100 [27]. Marked in gray is the limit for a background-free $CaWO_4$ experiment arising from coherent neutrino scattering (dominantly from solar neutrinos) [43].

In figure 1.19 a summary of the exclusion limits from several DM experiments in the low WIMP mass region are is shown.

LUX

The Large Underground Experiment (LUX) is based on a double phase Time Projection Chamber (TPC) which contains Xe in liquid and gaseous phases. The TPC, which contains an active volume of LXe of about 300 kg, is hosted in a double vessel structure that guarantees thermal isolation, figure 1.20. The detector is placed at the Stanford Underground Research Facility (SURF) at a depth of 4850 feet and it is surrounded by a water tank that acts as muon veto. The TPC has a diameter of 47 cm and a height of 48 cm. The prompt scintillation signal, S1, and the electroluminescence one, S2, are read by two PMTs arrays.

After the selection of a 118.3 kg fiducial volume for the analysis, 160 events have been observed in the WIMP search region ([2, 30] pe). From the likelihood analysis, all the events

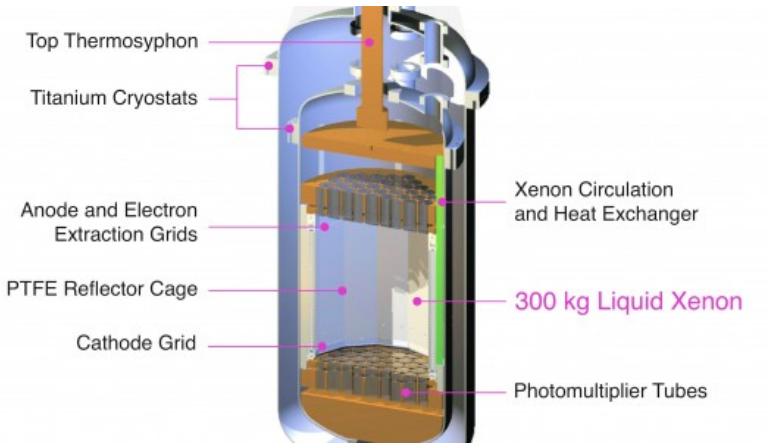

Figure 1.20: LUX cryostats and TPC structures.

have been found to be compatible with the background-only hypothesis resulting in new upper limits for the DM spin-independent cross section, whose minimum has been found at 7.6×10^{-46} cm^2 for a WIMP mass of 33 GeV/c^2.

The current WIMP exclusion limits for masses extending up to 1 TeV/c^2 is drawn in figure 1.21.

XENON

The XENON Collaboration faces the direct search for WIMPs through a scalable LXe detector arranged in a double-phase TPC. The first stage was the XENON10 experiment, successively upgraded to XENON100. The further extension is represented by the XENON1T experiment, which is currently in an advanced phase of installation at LNGS.

We describe in detail such experiment in the next chapter, with particular attention to XENON1T.

1.3.2 Indirect detection experiments

Unlike the direct Dark Matter searches, where the focus is on the observation of WIMP interactions in the detectors, indirect techniques aim to detect DM decay or annihilation products. Indeed, it is usually assumed that WIMPs can annihilate in SM particles. Viable signatures for such kind of processes are thus the production of neutrinos, γ-ray, positrons, anti-protons and anti-deuterons.

General AntiParticle Spectrometer (GAPS)

The GAPS experiment will search for antideuterons as signature for the Dark Matter annihilations.

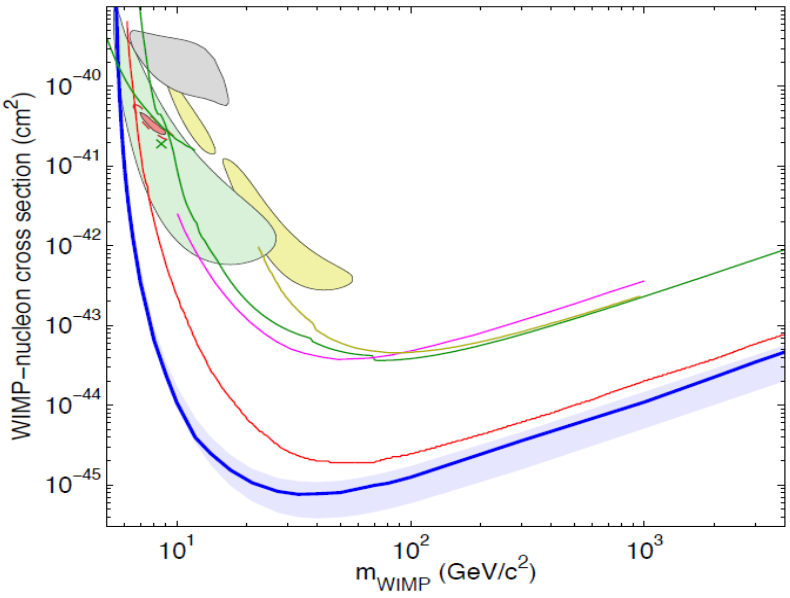

Figure 1.21: LUX 90% confidence limits on the SI elastic WIMP-nucleon cross section (blue) [28], together with the $\pm$ 1σ variation (light blue area) and XENON100 results from 225 live days run (red curve) [27]. Also shown are limits from: Edelweiss II [44] (dark yellow line), CDMS II [45] (green line), ZEPLIN-III [46] (magenta line), CDMSlite [39] (dark green line), XENON10 S2-only [47] (brown line), SIMPLE cite48lux (light blue line) and XENON100 100 live-day [48] (orange line). The colored regions come from measurements from annual modulation in CoGeNT [41] (light red, shaded), along with exclusion limits from low threshold re-analysis of CDMS II data [49] (upper green line), 95% allowed region from CDMS II silicon detectors [35] (green shaded) and centroid (green x), 90% allowed region from CRESST II [37] (yellow shaded) and DAMA/LIBRA allowed region [50] interpreted by [42] (gray shaded). Results sourced from DMTools [51].

Secondary antideuterons can be produced in collisions of cosmic rays (CR) with the interstellar medium (IM). Due to the mass of such nuclei, low energy productions are quite disadvantaged leading to a reduced background in the search for low energy nuclei.

Due to the background characteristics, the GAPS detector will be optimized for low energy antideuterons in particular in the range [100, 500] MeV. The first data acquisition is planned for the 2017. The detector will consist of a inner part made of 10 layers of Lithium-drifted Silicon (Si(Li)) modules for an overall cubic shape of 2 m edge. The inner tracker will be enclosed in a time-of-flight system (TOF) made of plastic scintillators with photomultipliers tubes (PMTs) for the readout. Also the TOF system will have a cubic shape with 4 m edge. GAPS will detect the X-ray emission after de-excitation of an exotic atom made of a target atom where an external electron is replaced by an antideuteron. After the de-excitation, the antideuteron annihilates with the nucleus, thus producing pions and protons.

The detector will be able to measure the velocity and the charge of the incoming particle in the TOF as well as the stopping depth of the particle in the tracker and the development of the energy loss per layer throughout the slowing process. The main source of background for the

Figure 1.22: View of the VERITAS telescope array.

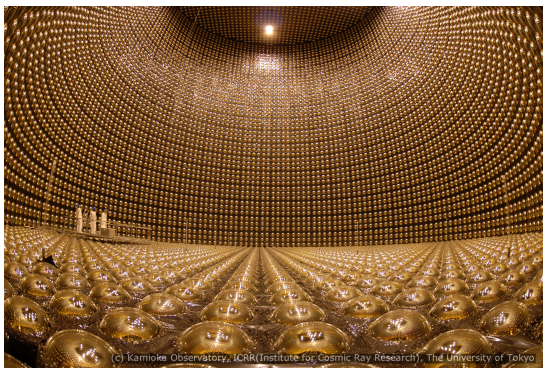

Figure 1.23: Internal view of the Super-Kamiokande detector.

antideuteron signal comes from antiprotons. Therefore, a good X-ray energy resolution along with a reliable tracking and counting systems for pions/protons are essential for the background reduction.

VERITAS

The VERITAS telescope consists of four 12 m diameter Davies-Cotton optical reflectors (see figure 1.22). They focus the light from γ-ray air showers, in the energy range from 100 GeV up to 50 TeV, onto four 499 pixel PMT cameras. Its observations are mainly directed to dSph galaxies and galaxy clusters. The dSph galaxies are gravitational-bound objects and are believed to contain up to $\mathcal{O}(10^3)$ times more mass as Dark Matter than as visible matter, making them widely discussed as potential targets for indirect Dark Matter observations. One of the most important results from VERITAS comes from the observation of the gamma-ray flux, from Segue 1 [52], perhaps originated by annihilation or decay of Dark Matter. Since no signal above the background has been observed, only upper limits on the gamma-ray flux have been set considering different annihilation channels.

Super-Kamiokande

The Super-Kamiokande (SK) detector, figure 1.23, is a kton water Cherenkov detector of cylindrical shape with height of 36.2 m and radius of 16.9 m. It is located in the Kamioka-Mozumi mine in Japan under about 1000 m rock. It consists of a inner detector with 11.146 inward-facing 50 cm PMTs and an outer detector equipped with 1885 outward-facing 20 cm PMTs, serving as a cosmic ray veto counter. This detector is able to search for Dark Matter through the detection of an excess of upward-going muons (upmu). These muons are generated by the muon neutrinos (generated in DM annihilations in the Sun) which interacts with rocks that surround the detector.

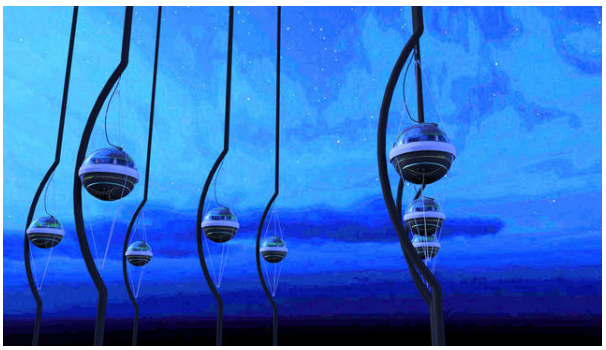

Figure 1.24: Representations of IceCube's DOMs.

For their last results, the collaboration used data acquired from April 1996 to August 2008 (3109.6 days) [53]. Muon events in the detector have been divided into three categories: "stopping", i.e. muons with the lowest energy that stop in the detector ($E_\nu << 10$ GeV); "showering", i.e. muons that produce showers in the detector and "non-showering", which don't produce any shower.

Using DARKSUSY calculations [54], the 90% CL limit on SD cross section has been evaluated as function of the WIMP mass. The minimum for the cross section is reached at a WIMP mass of 100 GeV/c^2 and it is equal to 4.5×10^{-39} cm^{-2} and 2.7×10^{-40} cm^{-2} in the soft, $\bar{b}b$, and hard, W^+W^-, annihilation channels, respectively.

Fermi-Large Area Telescope

The Fermi-Large Area Telescope (Fermi-LAT) is a gamma-ray telescope, placed on board the Fermi Observatory, sensitive to energies from 20 MeV up to over 300 GeV. One of the goals of this telescope is to find a DM signature in the diffuse gamma-ray emission. At galactic level, it is believed that the signal comes from annihilation of WIMPs in a smooth halo around the galaxy while the extra-galactic signal arises from DM annihilation processes throughout the universe. For the galactic halo study, the Fermi-LAT collaboration explored the energy range [1, 400] GeV. Limits were set both for annihilation and decay of DM particles.

IceCube

IceCube is a neutrino telescope placed at the south pole that aims at the detection of the Cherenkov light emitted by muons, created by neutrinos interacting with the Antarctica ice. The neutrinos of interest are generated by Dark Matter annihilations in the Earth and in the Sun. The telescope consists of 86 vertical strings equipped with Digital Optical Modules (DOMs), figure 1.24, that contain a digitizer board and a PMT. Part of these strings (78) carry 60 DOMs, placed at intervals of 17 m from a depth of 1450 m up to 2450 m below the ice surface. The other 8 strings are infill-specialized for a sub-array dubbed DeepCore, placed in the central region of the telescope.

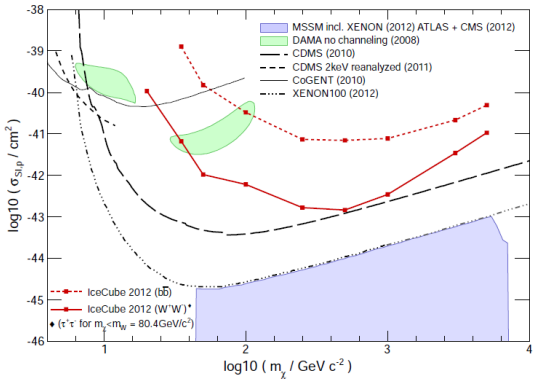

Figure 1.25: 90% CL upper limits on the **spin-independent** cross section $\sigma_{SI,p}$ for hard and soft annihilation channels over a range of WIMP masses. The shaded region represents an allowed MSSM parameter space. Systematic uncertainties are included.

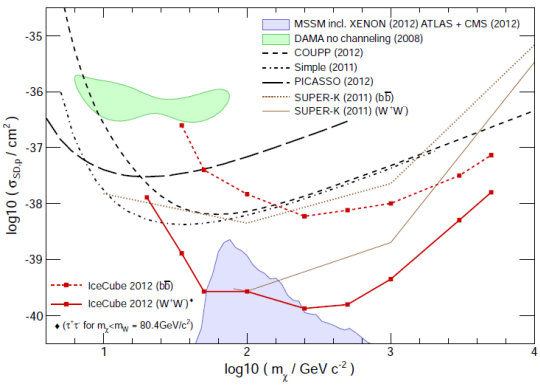

Figure 1.26: 90% CL upper limits on the **spin-dependent** cross section $\sigma_{SD,p}$ for hard and soft annihilation channels over a range of WIMP masses.

IceCube is sensitive to neutrinos in the energy range from 100 GeV up to 1 TeV, while DeepCore can reach sensitivity down to 10 GeV neutrinos. This means that the entire telescope is sensitive to neutralinos down to masses of about 50 GeV [55]. The last results of the IceCube collaboration come from the analysis of 317 live-days of data taken between June 2010 and May 2011 [49]. The main background of the telescope is due to muons and neutrinos produced by cosmic rays interacting in the atmosphere.

The background from solar atmospheric neutrinos, originating from cosmic rays interactions in the Sun's atmosphere, has also been calculated and it has been found to be of the order of 1 event [49, 56]. To take into account all the possible background variations, the dataset was divided into three parts: summer season, focused on low energy neutrinos, and winter season which is, in turn, divided into a low and high energy sample. After all the cuts and track selection criteria, the observed distributions of the event directions have been compared with the expected background distributions from atmospheric muons and neutrinos [49] finding compatibility with the only-background hypothesis. The obtained upper limits on the expected number of signal events, μ_s^{90}, can be translated into upper limits for the annihilation rate, Γ_a, of WIMPs in the Sun that, in turn, can be converted into limits on the spin-dependent, $\sigma_{SD,p}$, and spin-independent, $\sigma_{SI,p}$, WIMP-proton scattering cross-sections. Considering a local Dark Matter density of 0.3 GeV/c^3 and a Maxwellian WIMP velocity distribution with a RMS velocity of 270 km/s, limits on the spin-dependent WIMP-proton cross section for WIMPs annihilating into W^+W^- or $\tau^+\tau^-$, with masses above 35 GeV/c^2, were set [49], figure 1.25 and figure 1.26.

The IceCube data have been also used to infer information and set limits on the super heavy Dark Matter, i.e. for $m_\chi > 100$ TeV/c^2 [57]. These values of masses imply a much lower density

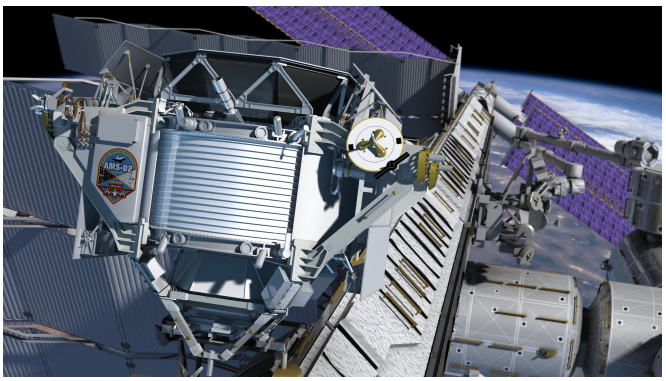

Figure 1.27: AMS-02 experiment on the International Space Station.

of Dark Matter which results in a reduced sensitivity for direct detection experiments. Due to the low density, this kind of search is based on the detection of the decay products such as high energy neutrinos. Considering Dark Matter with $m_\chi \sim 100$ TeV that decays into two neutrinos, IceCube already set limits on the lifetime giving the strongest limit: $\tau > 10^{27}$ y [58].

AMS-02

The Alpha Magnetic Spectrometer (AMS), currently in its second phase AMS-02, is an antimatter search experiment placed on the International Space Station (ISS), figure 1.27. In its latest results [59] the AMS collaboration has found an excess in the positron fraction, at energies > 8 GeV, above the expected background due to secondary positrons originate in the spallation of cosmic rays on the interstellar medium. The positron fraction stops to increase at ~ 275 GeV and this excess seems to be isotropic within 3%, suggesting that the energetic positrons may not be coming from a preferred direction in space.

Considering also the antiproton results from PAMELA [60], where the antiproton flux is compatible with the expected background, a scenario that consider a leptophilic Dark Matter, as possible source of positrons, is viable [61].

This kind of candidates annihilates predominately into leptons producing a large amount of energetic positrons while the antiproton flux remains suppressed. Using this kind of WIMP and considering masses above 500 GeV/c^2, the AMS-02 collaboration has evaluated the annihilation cross section for leptophilic channels that can explain the observed positron fraction [61]; the value for the annihilation cross section is of the order $10^{-23} \div 10^{-22}$ cm^{3}s^{-1} that is about 10^3 times larger than the thermal cross section.

Chapter 2

The XENON project

Among the various experimental strategies to directly detect Dark Matter particles, detectors using liquid xenon have demonstrated highest sensitivities over the past years. This is the case of the DM experiments realized by the *XENON Collaboration*. The first detector of the XENON project was XENON10 [62] (see section 2.2.1). The main goal of this experiment was to test the possibility to realize a dual phase, LXe/GXe, detector on the kg scale to detect Dark Matter interactions. The good results, obtained in 2007, pushed towards the realization of a new and larger detector, XENON100 [63] (see section 2.2.2), based on the same detection and work principles. Both detectors, have been placed in the interferometer tunnel at the Laboratori Nazionali del Gran Sasso (LNGS), Italy, at an average depth of 3600 m water equivalent.

The XENON100 experiment published the world's best upper limits on the spin-independent [27] and spin-dependent [64] coupling of WIMPs to nucleons in 2012 and 2013. Recently, the LUX experiment which also employs liquid xenon (LXe) as detection medium, has confirmed and improved upon these results [28]. To significantly improve upon current experimental sensitivities, the XENON collaboration is focusing on the XENON1T experiment [65]. With a 30 times larger target mass, and a background goal which is 100 times lower than the one of XENON100, the maximal sensitivity to spin-independent WIMP-nucleon cross sections is expected to improve by two orders of magnitude with respect to the XENON100 limits.

2.1 Detection principle of a dual phase TPC

The detectors of the XENON project are based on a *dual phase Time Projection Chamber* (TPC), containing xenon in the liquid phase (LXe) and, above it, a small gap of gaseous xenon (GXe). Xenon is maintained in the liquid phase by means of a cryogenic system working at temperatures around 160 K.

In this section we review the main properties of a xenon-based target and the characteristics of detection signals achieved with the dual phase TPC.

2.1.1 Liquid xenon as target

The choice of LXe as active target for the direct detection of Dark Matter implies several advantages. An important property of a xenon target is represented by its self-shielding power against external background sources, thanks to its high density, equal to 2.96 g/cm^3, and a relatively large triple point (165 K), which is not extremely demanding from the cyogenic point of view. Moreover, since the WIMP-nucleus cross section scales with A^2, the large xenon atomic number ($A = 131$), relatively to other noble gases, increases the expected WIMP interaction rate.

Xenon has about ten stable isotopes, while instable ones are very short-lived. Hence, it is a rather pure material, which is a mandatory requirement for a search of very rare events like WIMP scatterings. Specifically, there are two isotopes with nonzero spin: ^{129}Xe (spin 1/2) and ^{131}Xe (spin 3/2). This allows to study also the dependence of the WIMP-nucleus cross section on the spin, thus providing more information about the Dark Matter nature.

After an electronic transition from an exited to the fundamental state, xenon emits scintillation light of 177.6 nm wavelength, i.e. VUV photons. Xenon is an excellent scintillator, since emits about $5 \cdot 10^7$ photons per keV deposited, but has also a good ionization yield, of about $6 \cdot 10^7$ electron-ion pairs per keV. Therefore, an interaction produces both a relatively large amount of charges and photons.

The xenon scintillation is ruled by de-excitation of excimers, i.e. excited xenon dimeric molecules (Xe_2^*), which are formed after recoil events through direct excitation or recombination of ionization products. In the direct excitation process an excited state Xe^* is promptly formed, leading to scintillation through the following decay chain:

$$\begin{aligned} Xe^* + Xe + Xe &\rightarrow Xe_2^* + Xe \\ Xe_2^* &\rightarrow 2Xe + h\nu \, . \end{aligned} \tag{2.1}$$

After ionization in the xenon target, the Xe^+ ions can form a molecular state and a freed electron can recombine, producing scintillation at the end of the chain:

$$\begin{aligned} Xe^+ + Xe &\rightarrow Xe_2^+ \\ Xe_2^+ + e^- &\rightarrow Xe^{**} + Xe \\ Xe^{**} &\rightarrow Xe^* + \text{heat} \\ Xe^* + Xe + Xe &\rightarrow Xe_2^* + Xe \\ Xe_2^* &\rightarrow 2Xe + h\nu \, . \end{aligned} \tag{2.2}$$

Due to the different configuration of the energy levels of dimers and atoms, the photons emitted by dimers are not re-absorbed by the atoms making LXe transparent to its own scintillation light. The scintillation light in LXe has two decay components characterized by two different decay times: the singlet (S) and triplet (T) states of the excited dimers Xe_2^*. The

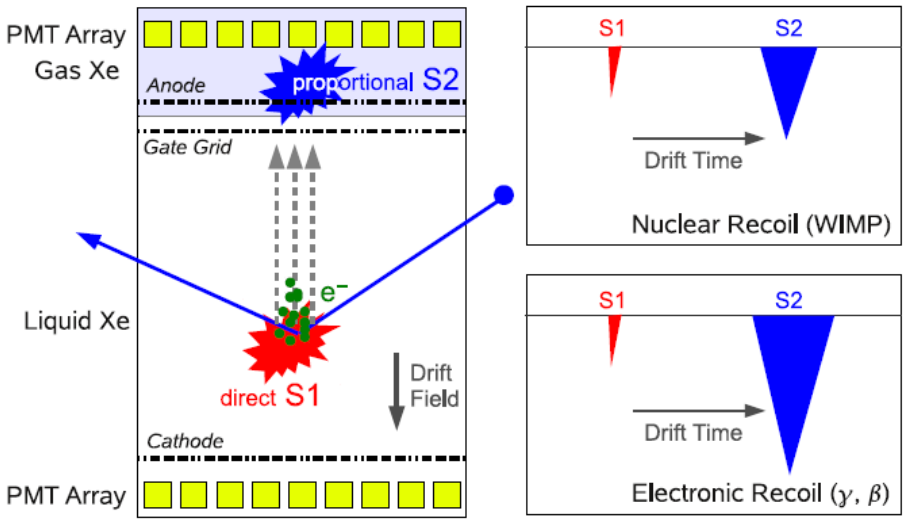

Figure 2.1: (Left) Schematic view of the XENON TPC along with its working principle. (Right) Illustration of characteristic wave forms due to different kinds of events, NR and ER.

fast scintillation component is due to the S state and its decay time can vary under intense electric fields. For instance, with a 4 kV/cm electric field, the decay times after the interaction of relativistic electrons with xenon atoms are: (2.2 ± 0.3) ns from the singlet states decays and (27 ± 1) ns from triplet states [66].

2.1.2 Signals produced in the TPC

As already said, a particle interacting in LXe produces a prompt scintillation signal, called **S1**, through excitation, and ionization electrons. The electrons can recombine, participating to the S1 signal, or can be drifted by an appropriate electric field towards the liquid-gas interface where they are extracted by a strong extraction field $\mathcal{O}(10$ kV/cm), and a light signal, named **S2**, is generated by proportional scintillation in the gas. The S2 signal is delayed by the time occurring in the drift from the interaction site to the liquid/gas interface.

On the bottom, the TPC is closed by the Cathode (at negative voltage) while on its top it is closed by the Gate mesh (grounded). This structure encloses the LXe active region, called *sensitive volume*, that represents the volume used to detect the interactions and which is available for the electrons drift. Along the vertical axis equally spaced thin copper rings are properly distributed, together with the Cathode and the Gate mesh, to generate a uniform electric field.

Above the Gate mesh there is the Anode and the LXe/GXe interface is set between them. Gate mesh and Anode produce the extraction field which has a strength of $\mathcal{O}(10)$ kV/cm, that guarantees an extraction level close to 100%.

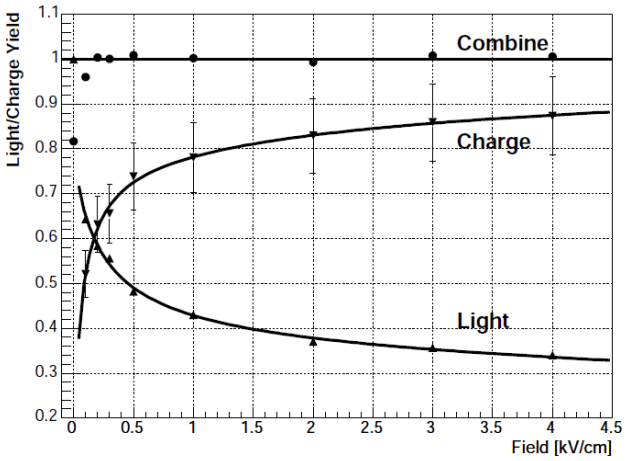

Figure 2.2: Light and charge yield as a function of drift field for 662 keV$_{ee}$ γ-rays from ^{137}Cs [67].

Two PMT arrays, one on top of the TPC inside the GXe and one at its bottom below the cathode, in LXe, are used to detect the scintillation light. From the pattern of the hit PMTs in the S2 signal, the (x, y) position of the events is determined, while from the time difference between S1 and S2 signals it is possible to infer the z coordinate. Combining all these informations, a 3D vertex reconstruction can be achieved. The knowledge of the interaction point allows the selection of those events located in the inner part of the LXe, usually called *fiducial volume* (FV) since the majority of background events are expected to be found outside, using the outermost volume as shield, thus remarkably reducing the background from external sources.

The S1 and S2 signals are also used to lower the background, thanks to their different distribution in case of either electromagnetic (ER) or nuclear recoils (NR). From the measured S1 and S2 it is possible to achieve a satisfying discrimination power between ER and NR events. Moreover, single scatter interaction (expected from WIMPs) can be distinguished from multiple scatters thanks to the presence of more than one S2 signal in the latter case.

Since the scintillation efficiency, i.e. the light output per unit energy deposited, for ER and NR is significantly different; therefore it is usual to define two energy scales: keV_{ee} (or keV_e) for ER events and keV_{nr} (or keV_r) for NR events. They are defined so as to avoid misinterpretation of the event energy in the case it is an ER or NR (see section 5.3.3).

A schematic view of the TPC structure and of the S1 and S2 signals pattern from NR and ER is shown in figure 2.1.

2.1.3 Discrimination of ER and NR

The ability to discriminate among different particles is essential for a Dark Matter experiment. WIMPs are expected to produce NR while most of the background radiation produces ER. Particles with different Linear Energy Transfer (LET), dE/dx, have different S2/S1 ratio and

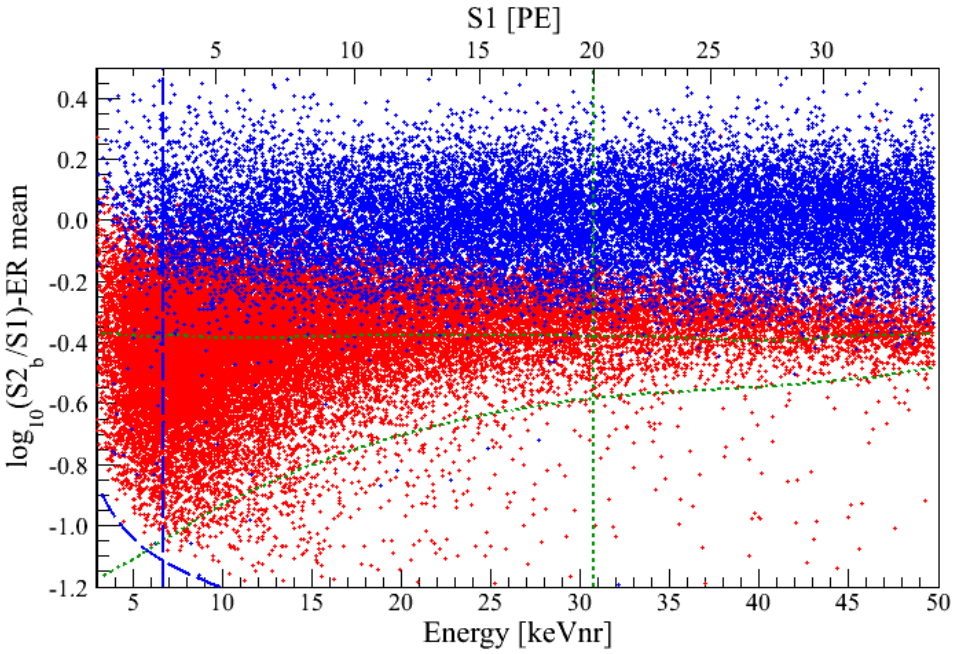

Figure 2.3: Distribution of the flattened discrimination parameter, $\log_{10}$(S2/S1), as function of the recoil energy achieved with the XENON100 experiment [27]. The ER band (red points), obtained from ^{60}C and ^{232}Th calibration data, is showed together with the NR band (blue points), from the ^{241}AmBe calibration.

this allows to discriminate among them. Indeed, a NR has a higher recombination rate, due to its higher LET, than an ER. A higher recombination gives a lower S2 and a higher S1 and ultimately a lower S2/S1 ratio. This characteristic of the signals implies the anti-correlation between ionization and scintillation signals, which is experimentally observed, figure 2.2.

Hence, using the ratio of the signals S1 and S2 as discrimination parameter, it is possible to distinguish between the two types of recoil. Having such a separation between the ER and NR bands, in the S2/S1 parameter, it is possible to set a discrimination level for the ER which allows to reach, or at least to lower, the desired background level.

The detector response to ER and NR events is studied through calibration runs where sources of photons (for ER) or neutrons (for NR) are used to produce a high statistics of recoil events of each type. The XENON100 performance is shown in figure 2.3 [27], where the ER band (blue) is clearly distinguished from the NR band (red). Indeed, the distribution of figure 2.3 is the "flattened" version of the S1/S2 distribution. The flattening is simply achieved considering $\log_{10}(\mathrm{S2/S1}) - ER(median)$, where $ER(median)$ is the median of the ER band. By this way, one gets a flat ER band centered in zero and removes the energy-dependence of this discrimination parameter.

With the separation achieved by XENON100, it is found that a 99.5% ER discrimination corresponds to a 50% acceptance of NR events, while 99.75% ER discrimination gives 40%

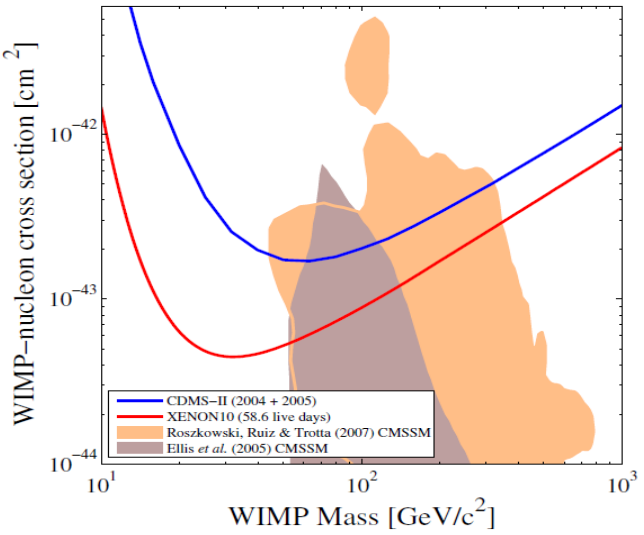

Figure 2.4: Cross section limit, 90% CL, on spin-independent WIMP interactions (red line), from the XENON10 58.6 live-days dataset [68]. The blue line is the best limit from CDMS experiment [69]. The shaded areas represent the allowed parameter region in the constrained minimal supersymmetric models.

NR acceptance [27]. This information will be crucial in determining the sensitivity of the experiment, as it will be extensively discussed in chapter 6.

2.2 The XENON experiments

The XENON Collaboration started with the XENON10 experiment, with a target mass of the order of 10 kg. We have seen the main features of the double phase (LXe/GXe) TPC. This kind of detector represents a scalable technology which allows successive upgrades toward larger target masses.

The XENON10 experiment has been followed by XENON100, whose xenon mass is in the order of 100 kg. The mass of the XENON1T experiment will be increased of a further factor 10. Finally, an upgrade to a xenon mass of about 7 tonnes, named XENONnT is already foreseen by the Collaboration.

In the following, we briefly review the main results of XENON10 and XENON100, while a more detailed discussion is dedicated to XENON1T, the experiment studied in this thesis.

2.2.1 XENON10

The XENON10 experiment [62], installed in 2005, has been in operation until October 2007. The TPC was made of a PTFE cylinder with an inner diameter of 20 cm and a height of 15 cm. The amount of LXe contained inside the TPC was 15 kg, with 5.4 kg used as fiducial volume.

In 2008, the Collaboration published the results of the 58.6 days run, establishing upper limits on both SI and SD WIMP-nucleon cross section. XENON10 reached a sensitivity at 90% confidence level to SI cross sections of 8.8×10^{-44} cm^2 for a 100 GeV/c^2 WIMP mass and 4.5×10^{-44} cm^2 for $m_\chi = 30$ GeV/c^2 [68] (see figure 2.4). Concerning the SD case, a limit of

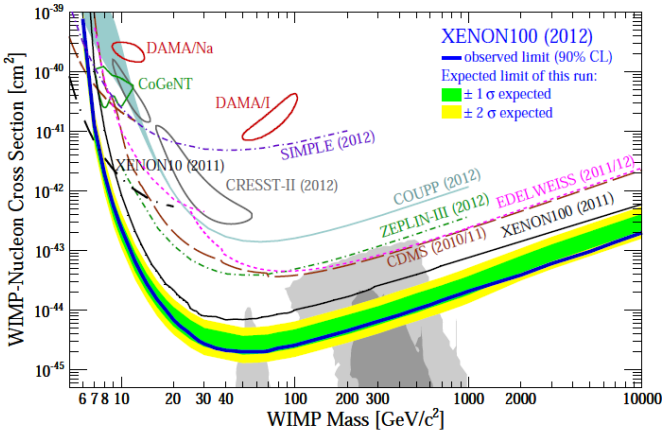

Figure 2.5: Result on SI WIMP-nucleon scattering from XENON100 [27]. The sensitivity is shown by the green/yellow band ($1\sigma/2\sigma$) and the resulting exclusion limit (90% CL) in blue. For comparison, other experimental limits (90% CL) and detection claims (2σ) are also shown together with the regions ($1\sigma/2\sigma$) preferred by supersymmetric (CMSSM) models [71].

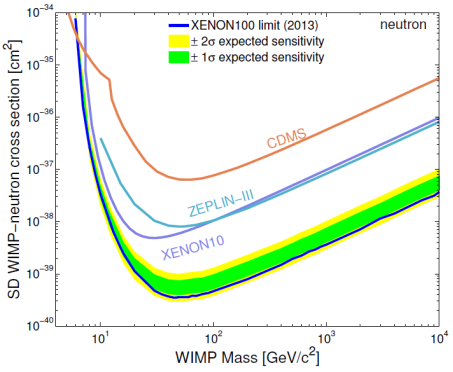

Figure 2.6: XENON100 90% CL upper limits on the WIMP SD cross section for interaction with neutrons [64]. The 1σ (2σ) uncertainty on the expected sensitivity is shown as a green (yellow) band. Also shown are results from XENON10 [70], CDMS [72], ZEPLIN-III [46].

5×10^{-39} cm^2 was set for 30 GeV/c^2 WIMP mass [70]. The XENON10 sensitivity plot for SD WIMP interactions is shown together with the result of XENON100 in figure 2.6.

2.2.2 XENON100

The XENON100 experiment [63] started in 2008 and it is still in data acquisition at LNGS. The LXe amount was increased to 161 kg, with 62 kg used as active volume in the TPC and the remaining as an outer active veto; the fiducial volume was chosen as 34 kg or 48 kg, depending on the background conditions in the various runs. The XENON100 TPC has a radius of 15.3 cm and a height of about 30.5 cm.

The goal of this experiment was to lower the sensitivity by two orders of magnitude with respect to XENON10. Such result has been achieved thanks to a larger target, but also thanks to a factor 100 of background reduction through an accurate screening and selection program for all detector construction materials.

No Dark Matter evidences have been found after 225 live-days of data taking. Two events have been found in the energy region of interest for the WIMP search, but this number is compatible with the expected background (1.0 ± 0.2 events). Hence, upper limits on the WIMP cross section have been set (at 90% confidence level): for the SI interaction the minimum is 2.0×10^{-45} cm^2 for $m_\chi = 55$ GeV/c^2 [27], while for SD interactions the best sensitivity corresponds to 3.5×10^{-40} cm^2 for $m_\chi = 45$ GeV/c^2 [64]. The exclusion limits as function of

Figure 2.7: Schematic overview of the XENON1T building placed at LNGS: on the left, the Muon Veto water tank containing the TPC; on the right the Service Building which host the cryogenic system, the DAQ equipment and the emergency recovery system.

the WIMP mass are shown in figures 2.5 and 2.6.

2.2.3 XENON1T

The XENON1T experiment [65] (figure 2.7) is currently under construction in the Hall B, shown in figure 2.8, of the Gran Sasso Underground Laboratory (LNGS). Mounting operations started in the fall of 2013 and will continue until the fall of 2015. Detector commissioning and a first science run are expected by the end of 2015, while the nominal Dark Matter sensitivity will be reached by 2017, after two years of operation.

The total amount of about 3 ton of LXe is contained in a double vessel vacuum insulated cryostat made of low activity stainless steel (SS), 5 mm thick. The dimensions of the inner cryostat are chosen to host the XENON1T TPC (figure 2.9), while the outer one is increased in order to host also the future enlarged version of the experiment, XENONnT. Both vessels are composed by a cylindrical part and two domes; the top dome is connected to the central part through a flange whose thickness is 50 mm. The upper domes have a central port from which the cryostat is connected to the XENON1T cryogenics system, via a long double-wall vacuum insulated tube.

The target consists of about 2 ton of LXe, defined laterally by an almost cylindrical structure of 24 polytetrafluoroethylene (PTFE) interlocking panels: the radius of the TPC is 479 mm. The target volume is viewed by two arrays of PMTs: one made of 121 PMTs in a compact hexagonal structure directly immersed in LXe in the bottom, and one made of 127 PMTs

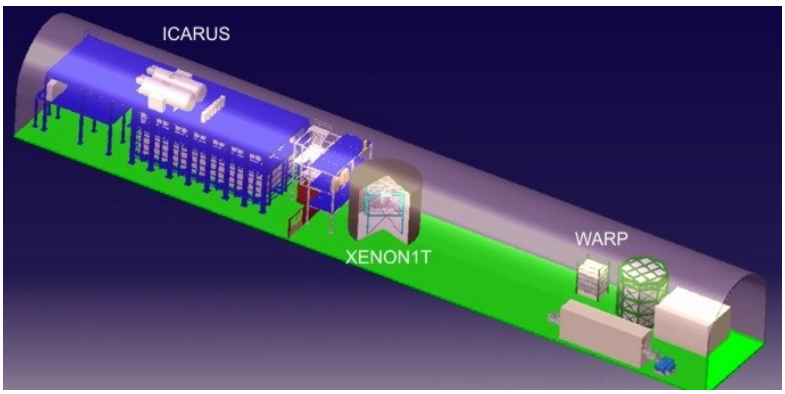

Figure 2.8: The Hall B of the Gran Sasso Underground Laboratory hosting the XENON1T detector.

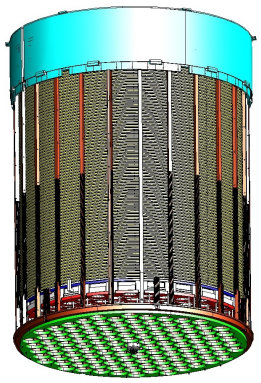

Figure 2.9: External view of the XENON1T TPC. Image from CAD drawings.

placed in concentric rings in the gas phase above the target volume. The radius of the bottom array is the same as the TPC, while the top one is slightly larger to guarantee a good position reconstruction even at the edge of the TPC. The space among the PMTs is covered with PTFE to reflect the UV light and ensure a good light collection efficiency. The structure of the TPC is reinforced on the outside region through PTFE pillars and copper rings. Additional PTFE and copper disks support the two PMT arrays.

The PMTs are the 3" Hamamatsu R11410-21, chosen for their low radioactivity and high quantum efficiency (36% on average). Their main components are a Kovar-free body, a quartz window and a ceramic stem, with also some smaller components made of SS and Aluminum. The voltage divider circuit is mounted on a base made of *Cirlex*.

The electric fields in the TPC are generated through electrodes made of SS meshes welded onto SS rings. There are two electrodes on the bottom of the TPC: the cathode and a second one to screen the bottom PMT array. At the liquid gas interface there is a stack of two electrodes, ground and anode, separated by 5 mm; another mesh is used to protect the top PMTs. The distance between the cathode and the ground meshes, which defines the "active" region where both the light and charge signals can be generated, is 967 mm, calculated taking into account the 1.5% shrinkage of PTFE panels at the LXe temperature. A stack of 74 field shaping rings, made of copper and placed just outside the PTFE lateral panels, assures the uniformity of the electric field along the TPC.

The liquid level in the proportional amplification region is adjusted between the gate and the anode electrode, and kept constant, by using the concept of a diving bell with an adjustable overflow tube coupled to a linear motion feedthrough. The bell closing the gas phase region is made of SS, 5 mm thick on the top and 3 mm in the lateral part. This solution has the additional advantage that the LXe outside the bell can rise above the top PMT array. In this way we have a layer of LXe, about 5 cm thick, above the Bell and all around the TPC (outside

of the field cage, between the rings and the cryostat wall); a 3 cm LXe layer is kept below the bottom PMT array. In the initial operation phase of the experiment this LXe layer will act as a passive shield to reduce the background from outside; in a second phase it can be instrumented with 1" PMTs and PTFE panels to be operated as an active veto.

The bottom part of the region inside the inner cryostat is completed with an empty filler, made of SS 5 mm thick along the cryostat wall and a 10 mm flat cap on top. It allows to reduce the total amount of xenon, and also to be used as a reservoir.

The Muon Veto system

At the depth of the LNGS, the flux of cosmic muons is $(3.31 \pm 0.03) \cdot 10^{-8} \mu$ cm^{-2}s^{-1} [73], with a mean energy of ~ 270 GeV [74]. Such particles, together with their cascades, generated in the rock and concrete of the laboratory, can give both ER and NR backgrounds. The latter is more problematic since neutrons, produced in spallation processes on nuclei or in electromagnetic and hadronic showers, have an energy up to tens of GeV and so they can penetrate even through large shields and mimic a WIMP signal. Therefore, several efforts have been put in designing a muon veto system that can tag and reject those events as background.

The Muon Veto for the XENON1T detector is made of a water tank with a cylindrical shape body, 4.8 m of radius and 9 m height, plus a truncated cone shape roof, for a total height of 10.5 m, that will be filled with water (figure 2.10).

The Muon Veto system is based on the detection of the Cherenkov light emitted by particles travelling through the water. The light is seen by 84 PMTs (8" in diameter), model Hamamatsu R5912ASSY, whose quantum efficiency in the range [300, 600] nm is about 30%. The PMTs are arranged in two rings, one on top at 9 m from ground and one on the bottom of the water tank, each made of 24 photomultipliers, and 4 equally spaced rings of 12 PMTs each, along the vertical wall of the tank.

The detector will be placed at the center of the structure (figure 2.11), thus resulting surrounded by an equal thickness water layer in all directions. The inner surface of the water tank will be covered by a reflective foil, DF2000MA, which has a reflective efficiency close to 100% between 400 and 600 nm wavelengths. It acts also as a wavelength-shifter to better overlap the Cherenkov light spectrum with the high quantum efficiency region of the PMTs.

In order to trigger a veto event two requirements have to be satisfied: the level of the signal has to overcome a defined threshold and the signal must stay above the threshold for a specific amount of time.

The evaluation of the trigger rate due to muon events requires to consider the PMT dark counting rate and the flux of particles from radioactive decay of rock and concrete that surround the experiment. It is possible to reduce these contributions using a N-fold PMT coincidence, in a certain time window, with a certain threshold. After several MC simulations [75] it was

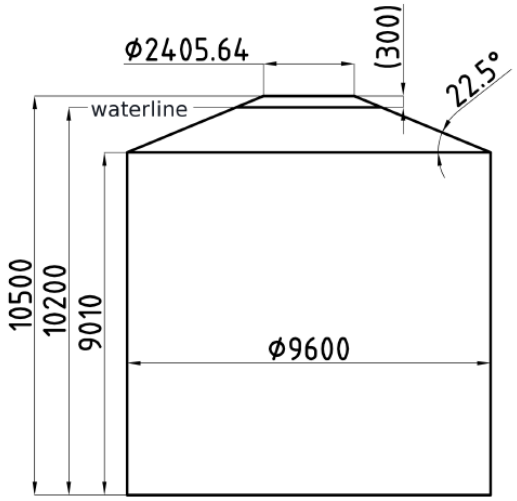

Figure 2.10: Schematic view of the XENON1T Muon Veto water tank.

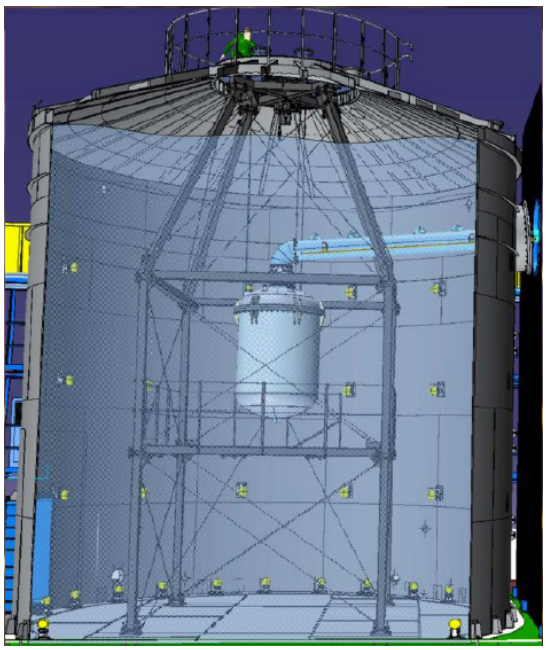

Figure 2.11: Design of the Muon Veto with the detector and its support structure at the center of the water tank [75].

established that using a 5-fold coincidence in 300 ns, a rate lower than 1 Hz can be reached, still having high efficiency in detecting single photoelectrons.

Monte Carlo simulations determined that the efficiency of the Muon Veto, with respect to the muon-induced events, is 99.78% for events directly from muons and 72.2% for shower-induced events. The residual muon-induced neutron background, in XENON1T, is < 0.01 ev/y in 1 tonne FV, i.e. practically negligible.

Chapter 3

Statistical hypothesis tests

In order to search for new physics phenomena or particles, one must distinguish between background (already known physics) and signal (new physics) events, and then study through statistical concepts the possible hypotheses at stake, basically the null or background-only hypothesis H_0 (which describes only known processes) and an alternative hypothesis H_1 (which includes both background and new physics signals).

Searches of rare events, like Dark Matter interactions with nucleons, often lead to the observation of no signal-type events and what an experiment is able to set is an upper limit for the quantity related to the appearance of new physics events. In our case such a quantity is the WIMP-nucleon cross section, as function of the possible WIMP masses. In mid-2012, XENON100 published the upper limits with a 90% confidence level for the spin-independent elastic WIMP-nucleon scattering cross section over a WIMP mass range from 8 GeV/c^2 to 10 TeV/c^2 [27]. The minimum value was set at 2×10^{-45} cm^2 in correspondence to 55 GeV/c^2. The current lowest limit has been carried out by LUX in 2013, excluding cross section values down to 7.6×10^{-46} cm^2 for a WIMP mass of 33 GeV/c^2 with a 90% confidence level [28]. As obvious, the search for WIMP particles evidences must proceed with experiments more and more sensitive to very low cross section values, below the aforementioned limits. Therefore, characterizing the experimental sensitivity becomes an aspect of primary importance in designing and realizing an experiment like XENON1T.

In the context of frequentist statistical tests, one obtains an upper limit from the observed data sets by investigating the significance with which non zero values of the cross section are excluded (i.e. the alternative hypotheses are rejected). Conversely, the sensitivity is based on the *expected* significance of the rejection of hypothesized cross section values.

Hypotheses tests are performed by defining a test statistic, that is a function of the observables, which allows to reduce the amount of data without losing the ability to discriminate between hypotheses. The test statistic should be chosen so as to get well distinct distributions when it is calculated under contrasting hypotheses. In principle, many different functions can

be used, but it has been demonstrated, through the Neyman-Pearson lemma, that the most powerful test statistic, in terms of signal purity given a significance level, is the likelihood ratio [76–78]

$$\frac{f(\mathbf{x}|H_0)}{f(\mathbf{x}|H_1)}\,, \tag{3.1}$$

where $\mathbf{x}$ is a vector of data and $f(\mathbf{x}|H_i)$ is the probability density function (p.d.f.) of the data under the hypothesis H_i.

3.1 Likelihood-based statistical tests

To accept or reject a certain hypothesis H, one needs to quantify how much a given data set is in agreement with that, by computing the statistical significance with which a statement of acceptance or rejection is made. The probability p of finding data equally or less compatible with the hypothesis H is called *p-value*. An equivalent significance Z is usually associated to the p-value. It is defined as the number of standard deviations above the mean of a gaussian distribution corresponding to an upper-tail probability[1] equal to p (figure 3.1):

$$Z = \Phi^{-1}(1-p)\,, \tag{3.2}$$

where Φ is the cumulative distribution (c.d.f.) of the standard Gaussian distribution. Therefore, Φ^{-1} gives the quantile relative to the $1-p$ percentile. A $Z = 5$ significance, which correspond to a p-value of 2.87×10^{-7}, is usually considered the appropriate value requested to announce a discovery. Conversely, when one wants to exclude a hypothesis, a threshold p-value is usually taken at 0.1 or 0.05, for which $Z = 1.29$ or 1.64. One often equivalently talks about p-value or *confidence level* (CL), which is expressed as the percentage corresponding to $1-p$. Thus, for instance, $p = 0.1$ is equivalent to the 90% confidence level.

The vast majority of particle physics searches summarize their results through frequentist significance tests and the p-value, or Z, are usually calculated by means of the likelihood ratio test statistic (3.1). One usually studies a model including a hypothesized *signal* of new physics in addition to a well known *background*, with the aim of claiming a discovery or setting exclusion upper limits in the parameter space of interest. Counting experiments represent the simplest case with which the Likelihood Ratio method can be illustrated.

We call s and b the expected mean number of signal and background events expected within an assumed model. It is often convenient to express the expected number of signal events as $\mu \cdot s$, where μ, named *signal strength*, can vary from 0 (background-only hypothesis) to 1 (nominal signal hypothesis). We consider first uni-dimensional models, i.e. we assume that a

[1] The relation between Z and p can be also defined considering two-sided gaussian fluctuations, i.e. the sum of lower and upper tails is set equal to p. However, the one-sided definition has the advantage that for $p = 0.5$, the significance Z is 0.

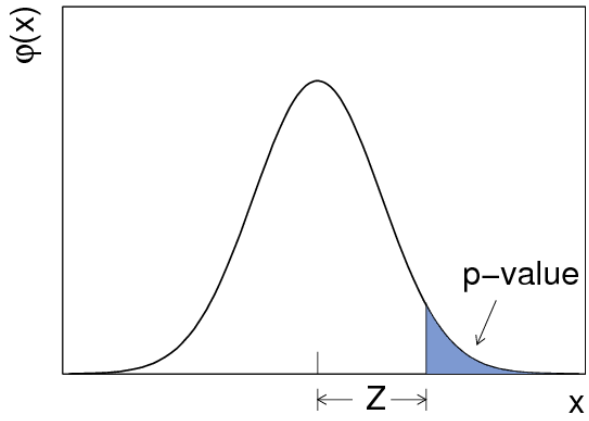

Figure 3.1: Relation between the p-value and the significance Z relative to a corresponding one-sided fluctuation of a Gaussian distributed variable.

kinematic variable x is measured for each observed event. Thus, the model consists not only in the prediction of the total number of events, but also in the spectra which determine how signal and background events are distributed with respect to x. In this case, the parameter μ is simply a scaling factor of the total number of expected signal events. Given the signal spectrum in the observable x, one can test all possible hypotheses H_μ by analyzing the whole range [0, 1] of μ values. This is desirable, for instance, when all possible cross section values of a rare particle interaction must be tested in order to set exclusion upper limits.

If we consider a binned analysis (the unbinned version is a straightforward extension of that), we can write the expectation value of the content n_i of each bin in the histogram of the variable x as

$$E[n_i] = \mu s_i + b_i \,, \tag{3.3}$$

with the mean number of entries in a specific bin from signal and background given by

$$\mu \cdot s_i = \mu \cdot s \int_{\text{bin}\, i} f_s(x|H_\mu)\, \mathrm{d}x \,, \tag{3.4}$$

$$b_i = b \int_{\text{bin}\, i} f_b(x|H_\mu)\, \mathrm{d}x \,. \tag{3.5}$$

The functions $f_s(x|H_\mu)$ and $f_b(x|H_\mu)$ are the signal and background p.d.f.s, whose shapes depend on the hypothesis under test by means of some parameters $\boldsymbol{\theta}$, named *nuisance parameters*. Note that the number of expected signal events μs is not a nuisance parameter as it is fixed by the nominal signal model.

The **likelihood function** is defined as the product of the probabilities to have an outcome n_i in the bin i, over all the bins, say N, of the x histogram. Since n_i are poissonian random variables, the likelihood function results

$$L(\mu, \boldsymbol{\theta}) = \prod_{i=1}^{N} \frac{(\mu s_i + b_i)^{n_i}}{n_i}\, e^{-(\mu s_i + b_i)} \,. \tag{3.6}$$

As we already mentioned, the agreement between a data set and a hypothesis H_μ can be evaluated using likelihood ratio test statistic, which in this case is taken as

$$\rho(\mu) = \frac{L(\mu)}{L(\hat{\mu})}\,, \tag{3.7}$$

where $L(\mu)$ represents the likelihood for a hypothesized value of μ, while $L(\hat{\mu})$ is its maximum value, found in correspondence to the maximum likelihood estimator (MLE) $\hat{\mu}$ of the signal strength μ. Indeed, given a set of data $\mathbf{n} = (n_1, ..., n_N)$, the MLE of μ is defined as the value which maximizes the likelihood function (3.6). So $\rho(\mu)$ ranges from 0 to 1, with higher values meaning better agreement between data and the hypothesis H_μ.

In the definition (3.6) the nuisance parameters $\boldsymbol{\theta}$ are assumed to be fixed with no uncertainty from the tested hypothesis. Instead, if we are to some extent uncertain about their value, the **profile likelihood ratio**

$$\lambda(\mu) = \frac{L(\mu, \hat{\hat{\boldsymbol{\theta}}})}{L(\hat{\mu}, \hat{\boldsymbol{\theta}})} \tag{3.8}$$

should be used rather than $\rho(\mu)$. Here, $\hat{\hat{\boldsymbol{\theta}}}$ stands for the conditional MLE of $\boldsymbol{\theta}$ under the hypothesis H_μ, i.e. that value which maximizes $L(\mu, \boldsymbol{\theta})$, with μ kept fixed at the value under test. The denominator of (3.8) is the maximum value of the likelihood function, selected by the maximum likelihood estimators of μ and $\boldsymbol{\theta}$ ($\hat{\mu}$ and $\hat{\boldsymbol{\theta}}$). The introduction of uncertainties on the nuisance parameters makes the profile likelihood broader as a function of μ with respect to the case of $\boldsymbol{\theta}$ fixed. This is not surprising since systematic uncertainties are added into the model through the nuisance parameters. However, exactly as with $\rho(\mu)$, once again $\lambda(\mu) = 1$ indicates the maximum agreement with the data, while lower values means larger discrepancy.

The most frequently used test statistic is not simply $\lambda(\mu)$, or $\rho(\mu)$, but the form

$$t_\mu = -2\,\ln \lambda(\mu)\,, \tag{3.9}$$

which is more convenient from a computational point of view, basically because it converts exponential terms into linear ones and products into sums. Contrary to the quantity (3.8), t_μ can vary from zero to infinite, with $t_\mu = 0$ for the best agreement, while more incompatibility causes increasing values of t_μ.

To quantify the level of disagreement between a data set and a hypothesis H_μ, firstly one should know how the test statistic is distributed under H_μ. Found the p.d.f. $f(t_\mu|\mu)$, the value of t_μ calculated from the observed data, called t_μ^{obs}, can be exploited to evaluate the corresponding p-value

$$p_\mu = \int_{t_\mu^{obs}}^{\infty} f(t_\mu|\mu)\,\mathrm{d}t_\mu\,, \tag{3.10}$$

i.e. the probability to observe a data sample as much as or less compatible with the hypothesis H_μ than the considered data are. By this way, if a threshold p_μ is fixed (e.g. $\alpha = 10\%$), those

values of μ producing p-values under the threshold can be rejected by means of the statistical hypothesis test based on the observed data. As a consequence, a confidence interval $[\mu_{low}, \mu_{up}]$ at $(1-\alpha)\%$ confidence level can be obtained from the scan of the whole range of possible values of μ.

3.1.1 Exclusion and discovery test statistic

The most general definition of the **profile likelihood test statistic** is the one given in (3.9). If one wants to evaluate the expected power of an experiment in rejecting the signal (exclusion) or the background-only hypothesis (discovery potential), simulations of data under a given hypothesis are required. In the exclusion case, one studies the power in rejecting signal hypotheses H_μ, while the discovery potential assess the experimental ability in rejecting the background hypothesis H_0, which necessarily implies a discovery. In these cases, one must use different definitions of the test statistic in accordance with the purpose of setting exclusion upper limits or claiming a discovery. Indeed, the a priori decision on computing exclusion or discovery intervals is also adopted in the analysis of real data [79].

Test statistic for exclusion upper limits

If the aim of the data analysis is to exclude signal hypotheses under test, the proper profile likelihood test statistic to be used is

$$q_\mu = \begin{cases} -2\ln\lambda(\mu) & \hat{\mu} \leq \mu \\ 0 & \hat{\mu} > \mu\,. \end{cases} \tag{3.11}$$

It differs from the generic definition (3.9) when the MLE $\hat{\mu}$ is found larger than the tested μ. In such case the test statistic is set to zero, which corresponds to the highest level of agreement with the hypothesis H_μ. The reason for this condition is that one do not want to regard upward fluctuation of data as an evidence of lack of compatibility with the signal hypothesis, since the declared purpose is to reject it. Hence, by this way one constrains the rejection region only to data samples with less events than expected under a given signal strength.

The level of agreement of a data set with a given signal strength μ to test, is evaluated from the canonical p-value calculation

$$p_\mu = \int_{q_\mu^{obs}}^{\infty} f(q_\mu|\mu)\,\mathrm{d}q_\mu\,. \tag{3.12}$$

An alternative test statistic to q_μ has been proposed for statistical models for which negative values of the parameter μ are physical meaningless. It is the case, for instance, in which μ represents a cross section value or a number of expected events. To take this into account, when $\hat{\mu}$ is found negative, one could modify the test statistic value by resetting the MLE to

zero, which is the nearest value in the physical domain of the parameter μ. Consequently, the alternative test statistic, named $\tilde{q}_\mu$, should be defined as

$$\tilde{q}_\mu = \begin{cases} -2\ln\frac{L(\mu,\hat{\hat{\boldsymbol{\theta}}}(\mu))}{L(0,\hat{\boldsymbol{\theta}}(0))} & \hat{\mu} < 0 \\ -2\ln\frac{L(\mu,\hat{\hat{\boldsymbol{\theta}}}(\mu))}{L(\hat{\mu},\hat{\boldsymbol{\theta}})} & 0 \leq \hat{\mu} \leq \mu \\ 0 & \hat{\mu} > \mu\,. \end{cases} \tag{3.13}$$

Following this approach, downward fluctuations of data which produce $\hat{\mu} < 0$ are interpreted as lack of background events, while in terms of signal such an an evidence is considered equivalent to the observation of the expected background with no signal events. However, statistical tests based on q_μ or $\tilde{q}_\mu$ usually provide very similar results [80]. From here on, we will refer to the standard q_μ test statistic if not explicitly declared.

Test statistic for discovery

Analogously, an other test statistic definition is used to study the statistical exclusion of the background-only model. This time, the hypothesis to test is only H_0, or equivalently the specific parameter value $\mu = 0$. In this context, higher values of $\hat{\mu}$ above zero point towards larger incompatibility with H_0, but data with $\hat{\mu} < 0$ are not interpreted against H_0, since they can not be a hint for the presence of signal. The test statistic used to find an exclusion interval of the background-only hypothesis is

$$q_0 = \begin{cases} 0 & \hat{\mu} < 0 \\ -2\ln\frac{L(0,\hat{\hat{\boldsymbol{\theta}}}(0))}{L(\hat{\mu},\hat{\boldsymbol{\theta}})} & \hat{\mu} \geq 0\,, \end{cases} \tag{3.14}$$

for which one has lack of agreement with H_0, i.e. $q_0 > 0$, only if $\hat{\mu} > 0$, while data with $\hat{\mu} < 0$ correspond to the maximum compatibility with the background-only hypothesis ($q_0 = 0$).

By means of this test statistic it is possible to evaluate the *discovery potential* of an experiments. Knowing the probability distribution of q_0 under the background hypothesis H_0 and simulating data samples under signal hypotheses H_μ, one can estimate the p-value of H_0, namely

$$p_0 = \int_{q_0^{obs}}^{\infty} f(q_0|0)\,\mathrm{d}q_0\,, \tag{3.15}$$

in order to find the minimum signal strength μ required to reject the background-only hypothesis at a given confidence level. The significance threshold to claim discovery of new physics phenomena is usually set at 5σ, corresponding to a p-value of 2.9×10^{-7}.

The present work is focused on the study of the experimental sensitivity of the XENON1T experiment, therefore in the following we describe in more detail the evaluation of exclusion upper limits using the proper test statistic q_μ.

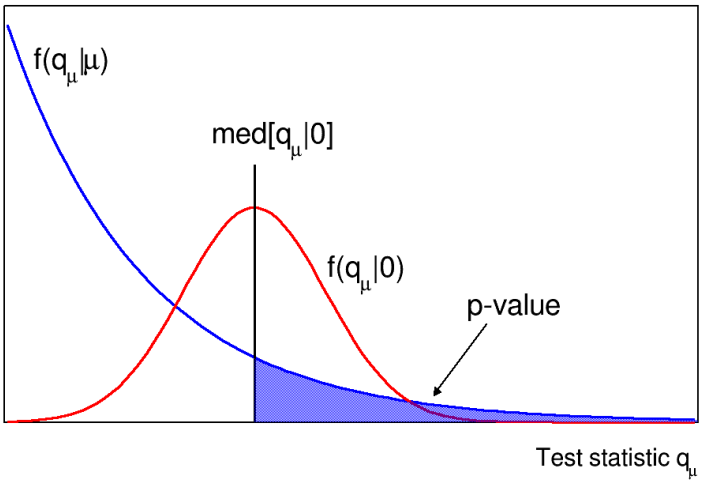

Figure 3.2: Toy illustration of expected p-value (blue filled area), for the hypothesis H_μ, under which the test statistic q_μ has the distribution $f(q_\mu|\mu)$ (blue curve). It is calculated using the median of the test statistic distribution $f(q_\mu|0)$ (red curve) obtained by simulating numerous toy experiments based on the background-only model H_0.

3.2 Experimental sensitivity

The sensitivity gives the expected power of the experiment in rejecting signal hypotheses in the case the background would be the only source of events. In the framework of the XENON1T experiment, the sensitivity is represented by the curve of the minimum values of the WIMP-nucleon cross section, σ, as function of different WIMP masses which can be excluded. More precisely, for each mass, one studies the *expected* significance of a test on various signal hypotheses H_μ (i.e. varying the signal strength) with the aim of rejecting them, if it is assumed that the data come from the background-only hypothesis H_0.

Let us specify the operational meaning of the *expected* significance of hypothesis tests. To estimate what to expect if WIMPs did not exist, one must simulate fictitious data samples, also called *toy experiments*, generated from the background-only model. For each sample, the test statistic q_μ can be calculated in correspondence to different values of μ. Collecting several toy experiments, an estimate of the distribution of q_μ^{obs}, which one would obtain from data stemming from H_0, is evaluated. They are the p.d.f.s $f(q_\mu|\mu = 0)$ for each hypothesized μ. The expected significance is related to the median value of $f(q_\mu|0)$, since such value, med$[q_\mu|0]$, is taken as the lower edge of integration in the calculation of the p-value [80]:

$$expected\ p_\mu = \int_{\text{med}[q_\mu|0]}^{\infty} f(q_\mu|\mu)\, \mathrm{d}q_\mu\ . \tag{3.16}$$

Therefore, having fixed a hypothesized μ, and having established the two test statistic p.d.f.s $f(q_\mu|\mu)$[2], i.e. the distribution in the signal model H_μ, and $f(q_\mu|0)$, the distribution under the background-only hypothesis, one is able to assess the expected rejection significance of μ by means of the equation (3.16). At this point, a threshold α must be chosen for the p-value, in

[2]The determination of $f(q_\mu|\mu)$ is achieved as in the case of $f(q_\mu|\mu)$, but simulating data under the proper hypothesis H_μ.

order to exclude μ or not. Thus, by performing a complete scan of the possible values of μ, one finds the interval to be rejected with a $(1-\alpha)\%$ confidence level, made up of those μ with

$$\textit{expected } p_\mu < \alpha \,. \tag{3.17}$$

The upper limit on μ, named $\mu^{\rm up}$, is the lowest among the excluded ones. In other words, we can state that, if the background-only hypothesis is true, the experiment is expected to be able to reject with a, say, 90% CL signal hypotheses H_μ larger than $\mu^{\rm up}$. One says the experiment is sensitive, at most, to signals as weak as those produced by $\mu^{\rm up}$. In our study, the upper limits on μ are finally converted into cross section values, namely $\sigma^{\rm up}$. The full sensitivity curve of XENON1T is then carried out by simply repeating the estimation of $\sigma^{\rm up}$ for different WIMP masses.

As obvious, each simulated toy experiments will generate a different data set and thus different values of $\hat{\mu}$, the MLE of μ. Consequently, the test statistic q_μ^{obs} will assume different values each time, following the aforementioned probability distribution $f(q_\mu|0)$. Statistical fluctuations in the data must be, therefore, taken into account when the upper limits are computed. The impact of such fluctuations on the upper limit determination stems from the width of the expected test statistic distribution $f(q_\mu|0)$. Thus, in addition to the *median* limit $\mu^{\rm up}$, it is recommendable to report also how much it would vary for given fluctuations in the data. The **error bands** on $\mu^{\rm up}$ are constructed by carrying out the same procedure, taking not the median of $f(q_\mu|0)$, but values corresponding to a fluctuation of N standard deviation from that. For example, the $\pm1\sigma$ error band is obtained considering the 15.87% ($\text{med}[q_\mu|0]-1\sigma$) and the 84.13% ($\text{med}[q_\mu|0]+1\sigma$) quantiles of $f(q_\mu|0)$. They will lead to upward and downward shifted upper limits with respect the "median" value. Over all the WIMP masses, what one constructs is an error band around the expected limit $\mu^{\rm up}$ delimited by the values computed as just said. Usually, the $\pm1\sigma$ and $\pm2\sigma$ bands are reported when the experimental sensitivity is shown.

3.2.1 The CL$_s$ method

In experiments searching for new signal processes often arise the problem of the exclusion of parameter values to which the experiment is very poorly sensitive. This happens, e.g., if one tests very small signal strengths μ, which predict data almost indistinguishable from the background-only model. Downward fluctuations of the background or incorrect estimate of the background rate would lead to the anomalous exclusion of low μ values.

A way to mitigate the issue of excluding signal hypotheses H_μ, to which the experiment is not sensitive, is provided by the CL_s method [81,82]. In order to protect against such an effect, the p-value considered to assess the significance is modified to

$$p'_s = \frac{p_\mu}{1-p_b} \,, \tag{3.18}$$

where $1 - p_b$ express the significance of the background-only hypothesis given the same test statistic value q_μ^{obs} used to evaluate p_μ, that is

$$1 - p_b = \int_{q_\mu^{obs}}^{\infty} f(q_\mu|0)\,\mathrm{d}q_\mu \,. \tag{3.19}$$

Hence, p_μ is penalized by an amount increasing with decreasing significance of H_0. If one finds data with significantly less events than predicted by a signal hypothesis with very low μ tested, it is often the case of also incompatibility with the background-only hypothesis (meaning low values of both p_μ and $1-p_b$). In such cases p_μ is strongly increased by the CL_s method, avoiding the exclusion of too low μ values.

However, one must keep in mind that the coverage properties of statistical inference executed applying the CL_s method are not clearly established for the theoretical point of view, since it represents a modification *ad hoc* of the frequentist inference.

The CL_s is a conservative method as it produces weaker exclusion limits, i.e. larger upper limits, and has an over-coverage nature. Moreover, its overall effect on the limit distribution obtained from the procedure to evaluate the experimental sensitivity is to squeeze the lower tail of the distribution toward higher values, consequently avoiding too optimistic exclusion limits.

Chapter 4

Simplified statistical model

We present here the implementation of a simple signal plus background model for which we carry out the sensitivity evaluation following the precepts described in the previous section. Then, we will compare our results with those obtained using the *RooStats* tool [83] (section 4.4). The aim of this chapter is to validate our analysis through the RooStats tool for a rather standard and simple model.

The sensitivity study for the full XENON1T statistical model will be presented in chapter 6.

4.1 Definition of the model

We consider a uni-dimensional statistical model, i.e. background and signal are characterized by a unique observable, namely x. The background and signal p.d.f.s, called G_b and G_s respectively, are analytical distributions defined as

- background: gaussian with mean 0 and unit variance, G_b;
- signal: gaussian with mean -2.58 and standard deviation 0.92, G_s.

This choice reflects the modeling of ER and NR distributions in the discrimination parameter Y used in the XENON1T bi-dimensional model (see section 6.1.2). However, we remark that this model is introduced just as a dummy simplified example.

We indicate the background and signal expectation values of the number of observed events as μ_b and μ_s. The background level is fixed at $\mu_b = 120$, while we will vary μ_s in order to calculate the expected sensitivity in rejecting the signal hypotheses tested. An example of a data set, with enhanced signal to $\mu_s = 50$, is shown in figure 4.1.

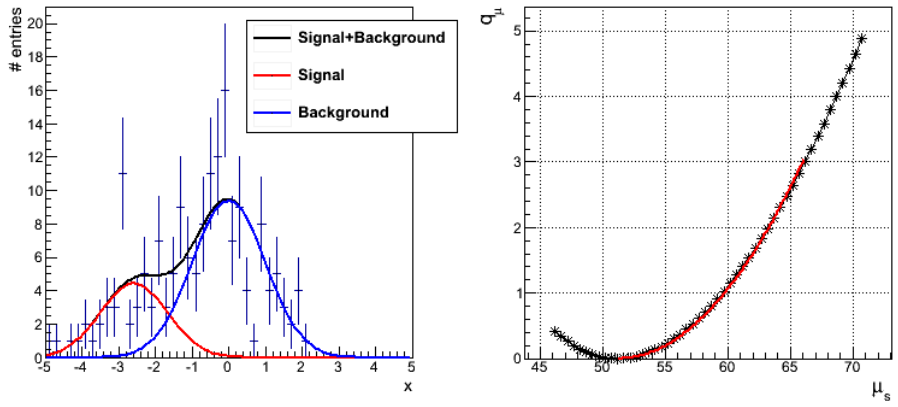

Figure 4.1: (Left) Example of a data set generated assuming $\mu_s = 50$ and $\mu_b = 120$ as signal and background expectation values; (Right) distribution of the test statistic q_μ as function of μ_s for the data sample shown to the left. The MLE $\hat{\mu}_s$ is found equal to 51.2.

4.2 Likelihood function and test statistic

The analysis of simulated data set is based on the *unbinned* version of the **likelihood function** (3.6). It means that the data are sampled from the analytical functions G and, thus, each event is identified by a value of the unbinned observable x. The total number of events N_{obs} in a data set is also a random variable (poissonian), whose expectation value corresponds to $\mu_{tot} = \mu_s + \mu_b$.

In the expression of the likelihood function, one then must add the poissonian probability to observe N_{obs} events in addition to the product of the probability of each event x_i. In this case the likelihood is said *extended* and it is written as [84]

$$L(\mu_s) = \frac{\mu_{tot}^{N_{obs}}}{N_{obs}!}\, e^{-\mu_{tot}} \prod_{i=1}^{N_{obs}} P(x_i) = \frac{e^{-\mu_{tot}}}{N_{obs}!} \prod_{i=1}^{N_{obs}} \mu_{tot}\, P(x_i)\,, \tag{4.1}$$

where x_i is the value of the observable for the i-th event and $P(x_i)$ express the corresponding probability, which can be written, in terms of its components, as

$$P(x_i) = \frac{1}{\mu_{tot}} \left[\mu_s\, G_s(x_i) + \mu_b\, G_b(x_i)\right]. \tag{4.2}$$

If we consider the log-likelihood function, we get

$$-2 \ln L(\mu_s) = 2\,(\mu_s + \mu_b) - 2 \sum_{i=1}^{N_{obs}} \left[\mu_s\, G_s(x_i) + \mu_b\, G_b(x_i)\right]. \tag{4.3}$$

The *parameter of interest* for the analysis is the expected number of signal events μ_s.

Having defined the likelihood function, the **test statistic** exploited to evaluate exclusion limits is the proper likelihood ratio q_μ (3.11):

$$q_\mu = \begin{cases} -2 \ln \frac{L(\mu_s)}{L(\hat{\mu}_s)} & \text{if } \hat{\mu}_s \leq \mu_s \\ 0 & \text{if } \hat{\mu}_s > \mu_s\,, \end{cases} \tag{4.4}$$

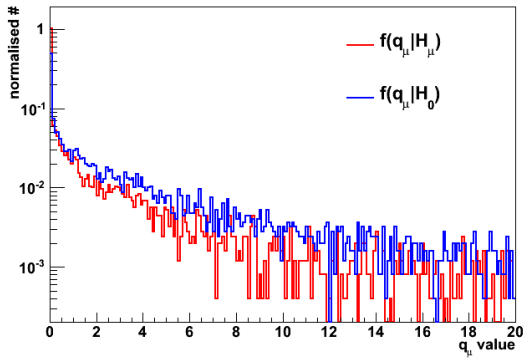

(a) Test statistic distributions $f(q_\mu|H_\mu)$ and $f(q_\mu|H_0)$ for the signal hypothesis $\mu_s = 1$.

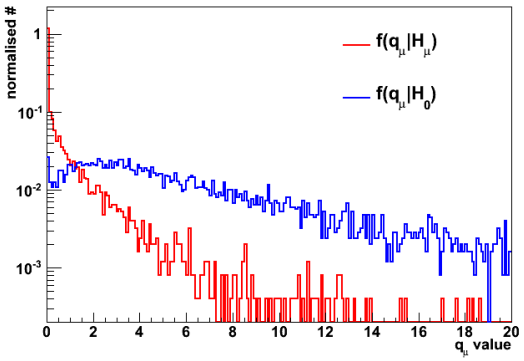

(b) Test statistic distributions $f(q_\mu|H_\mu)$ and $f(q_\mu|H_0)$ for the signal hypothesis $\mu_s = 5$.

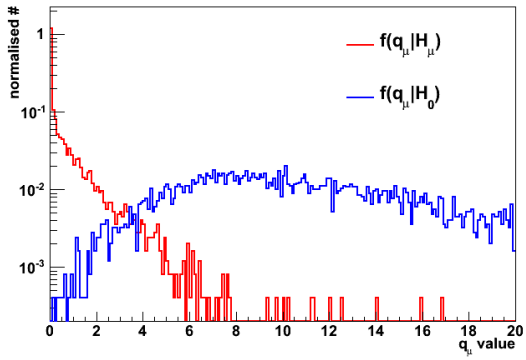

(c) Test statistic distributions $f(q_\mu|H_\mu)$ and $f(q_\mu|H_0)$ for the signal hypothesis $\mu_s = 10$.

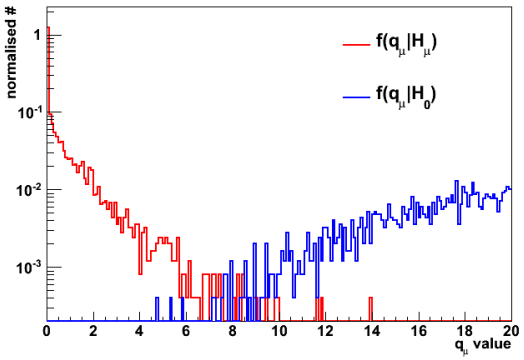

(d) Test statistic distributions $f(q_\mu|H_\mu)$ and $f(q_\mu|H_0)$ for the signal hypothesis $\mu_s = 20$.

Figure 4.2: Probability distributions of the test statistic q_μ under signal and background-only hypothesis for different μ_s tested.

where μ_s specifies the signal hypothesis under test, while $\hat{\mu}_s$ is its MLE, i.e. the value which maximizes the likelihood (4.1). The MLE $\hat{\mu}_s$ is operationally found by minimizing the log-likelihood function (4.3). The test statistic q_μ represents the distance of the log-likelihood computed for a given μ_s with respect to its minimum, found at $\hat{\mu}_s$. The typical trend of q_μ as function of μ_s is shown in figure 4.1.

4.3 Evaluation of the sensitivity

In order to perform tests of several signal hypotheses, one must know the distribution $f(q_\mu|H_\mu)$ of the chosen test statistic under each hypothesis H_μ. Moreover, in the sensitivity study one must also produce the corresponding p.d.f.s of q_μ obtained from background-only toy experiments, i.e. the $f(q_\mu|H_0)$ distributions.

To this purpose, we generate a large number of data samples under all signal assumptions of

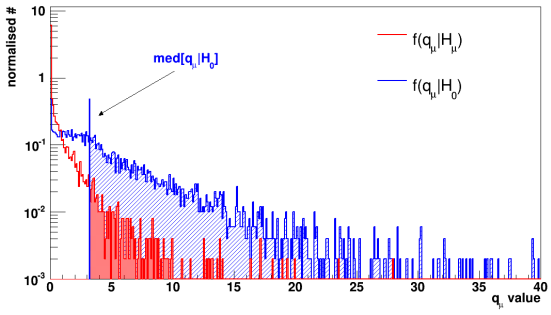

Figure 4.3: Distributions $f(q_\mu|H_\mu)$ (red) and $f(q_\mu|H_0)$ (blue) for tested $\mu_s = 5$.

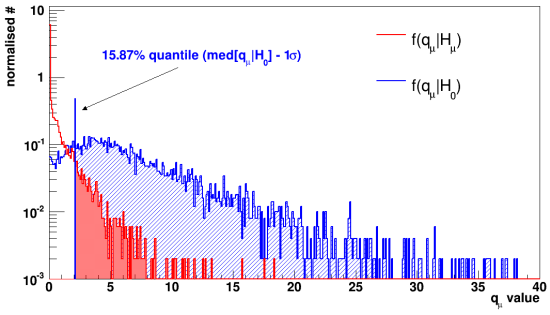

Figure 4.4: Distributions $f(q_\mu|H_\mu)$ (red) and $f(q_\mu|H_0)$ (blue) for tested $\mu_s = 8$.

interest. A distribution $f(q_\mu|H_\mu)$, for a given μ_s, is obtained by collecting an appropriately large statistics of data samples generated under a specific signal expectation value and by calculating each time the associated test statistic value q_μ^{obs}. Such procedure is repeated for every signal hypothesis μ_s.

A toy experiment is generated via poissonian extraction of the number of signal and background events with mean values μ_s (depending on the assumed hypothesis) and μ_b (fixed by the model). Then, the x value of each event is sampled from the respective spectra according to the nature of the event (signal or background).

A few examples of test statistic distributions, for different μ_s, are reported in figure 4.2. One can easily see that for very weak signal hypothesis the p.d.f. $f(q_\mu|H_0)$ approaches $f(q_\mu|H_\mu)$, indicating quite good compatibility between signal and background-only hypotheses. On the contrary, moving toward higher μ_s, $f(q_\mu|H_0)$ becomes a broader distribution containing increasingly large values of the test statistic, representing higher incompatibility with the signal hypothesis H_μ. As one would expect, the separation between $f(q_\mu|H_0)$ and $f(q_\mu|H_\mu)$ is remarkable when testing strong signal hypotheses, but it reduces when μ_s is small, making difficult the rejection of H_μ and ultimately limiting the experimental sensitivity.

We produced the test statistic p.d.f.s $f(q_\mu|H_\mu)$ and $f(q_\mu|H_0)$ for μ_s ranging from 0 to 20 by generating 5000 independent toy experiments under such hypotheses H_μ and H_0. The procedure followed to evaluate the experimental sensitivity consists in performing hypothesis tests with the aim to find the lowest μ_s we are able to exclude with the given confidence level.

The sensitivity study is carried out fixing a confidence level of 90% and using the CL_s method (see section 3.2.1). Thus, we will reject a signal hypotheses if its modified p-value, p'_s, is lower than 10%. The upper limit μ^{up}, above which WIMPs are excluded, is then identified by the condition: $p'_s = 0.1$. From the computational point of view, we can analyze only discrete values of μ_s. The number of signal events corresponding to the threshold p-value is found through interpolation between those μ_s actually studied.

The reference sensitivity limit is calculated using as q_μ^{obs} the median of the distribution

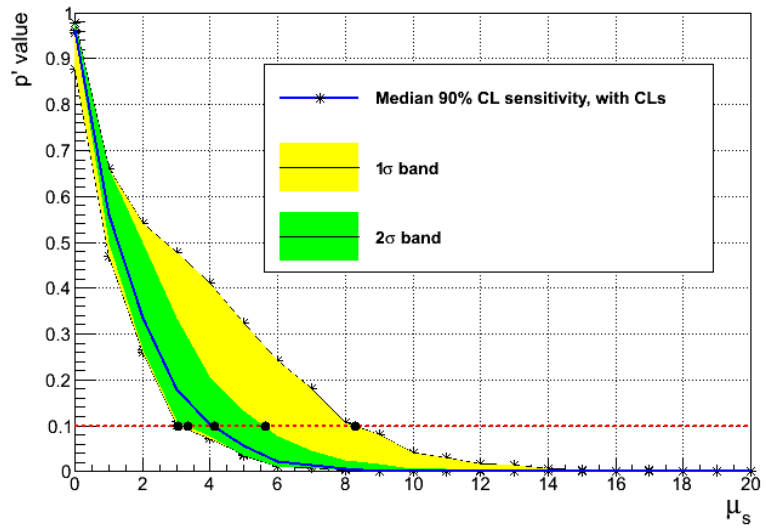

Figure 4.5: Values of p'_s as function of signal hypotheses μ_s. The blue curve indicates the p'_s calculated with the median of $f(q_\mu|H_0)$, while the green and yellow bands comes from the calculation of p'_s with the $\pm1\sigma$ and $\pm2\sigma$ quantiles of $f(q_\mu|H_0)$. The horizontal dashed line marks out the threshold corresponding to 90% CL.

of q_μ obtained from the background-only toy experiments. The error bands comes from the analogous tests, but performed using the $\pm1\sigma$ and $\pm2\sigma$ quantiles of $f(q_\mu|H_0)$, which are 15.87% and 84.13% for 1σ and 2.28% and 97.72% for 2σ. It should be noted that when the lower 1σ and 2σ quantiles of $f(q_\mu|H_0)$ are considered, the limit found correspond to upward 1σ and 2σ fluctuations of μ^{up} and vice versa.

A graphical overview of the p'_s calculation is given in figures 4.3 and 4.4. Having selected the desired quantile of $f(q_\mu|H_0)$ (blue p.d.f.), p'_s is given by the ratio of the integral over $f(q_\mu|H_\mu)$ (red shaded area) and the corresponding percentile of $f(q_\mu|H_0)$ (blue area).

The result of the sensitivity study for this simple model is outlined in figure 4.5, where p'_s (median, 1σ and 2σ bands) is plotted as function of the μ_s tested. The exclusion limit corresponding to the 90% confidence level is found equal to 4.1.

4.4 Comparison with results from RooStats

The same statistical model has been implemented within the RooStats tool [83], whose classes are built on top of the RooFit package [85] of the ROOT software [86].

An example of a simulated data sample is reported in figure 4.6. The calculation of the sensitivity has been performed taking advantage of the standard tutorial macro *StandardHypoTestInvDemo.C* [87] provided by RooStats. By setting the correct test statistic (q_μ) and type of analysis ("frequentist"), we carried out the same scan of signal hypothesis presented in the previous section by generating, again, 5000 toy experiments. Some of the test statistic distributions $f(q_\mu|H_\mu)$ and $f(q_\mu|H_0)$ produced by RooStats are shown in figure 4.7.

The confidence level has been set at 90% and the hypothesis tests have been performed using the CL_s correction. Figure 4.8 shows the final result produced by RooStats. The quite

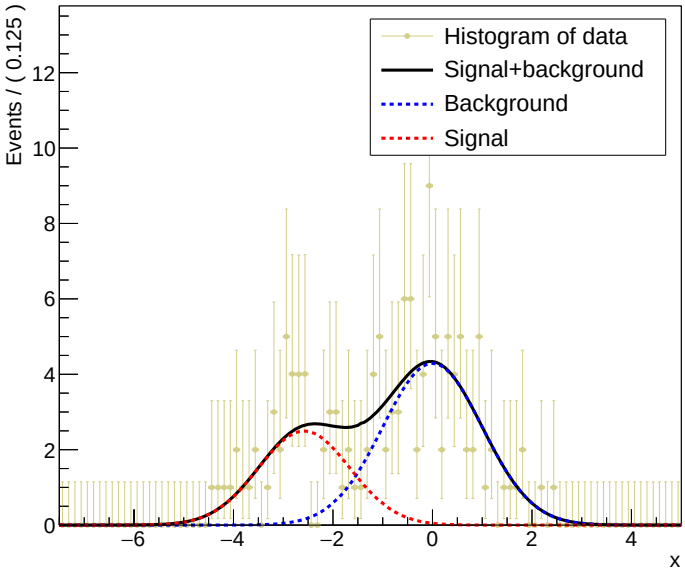

Figure 4.6: RooStats implementation: example of a data set generated assuming $\mu_s = 50$ and $\mu_b = 120$ as signal and background expectation values.

different behavior of the p-value bands above about 0.5 is related to the binning of the test statistic distributions used to compute p'_s. Their integration is particularly sensitive to different computational algorithms for very small q_μ. Nonetheless, the limit calculation is not affected by this aspect since it is related to the region of small p-values, near 0.1 in our case.

The exclusion limit found at 90% CL is 4.0, hence in good agreement with the value obtained from our implementation. In table 4.1 we show the direct comparison of p'_s for each μ_s tested from the two calculations. These values are very close, therefore we can consider our implementation to be pretty robust.

In the following chapters, we will extend this simplified case to the statistical model for the the XENON1T experiment and, finally, we will evaluate its expected sensitivity.

Expected exclusion limits at 90% CL		
	Our code	RooStats
-2σ	3.0	2.6
-1σ	3.3	3.3
median	4.1	4.0
-1σ	5.6	5.6
-2σ	8.3	8.4

Table 4.1: Comparison of the expected exclusion limit, median and error boundaries, calculated with our implementation and with the RooStats tool.

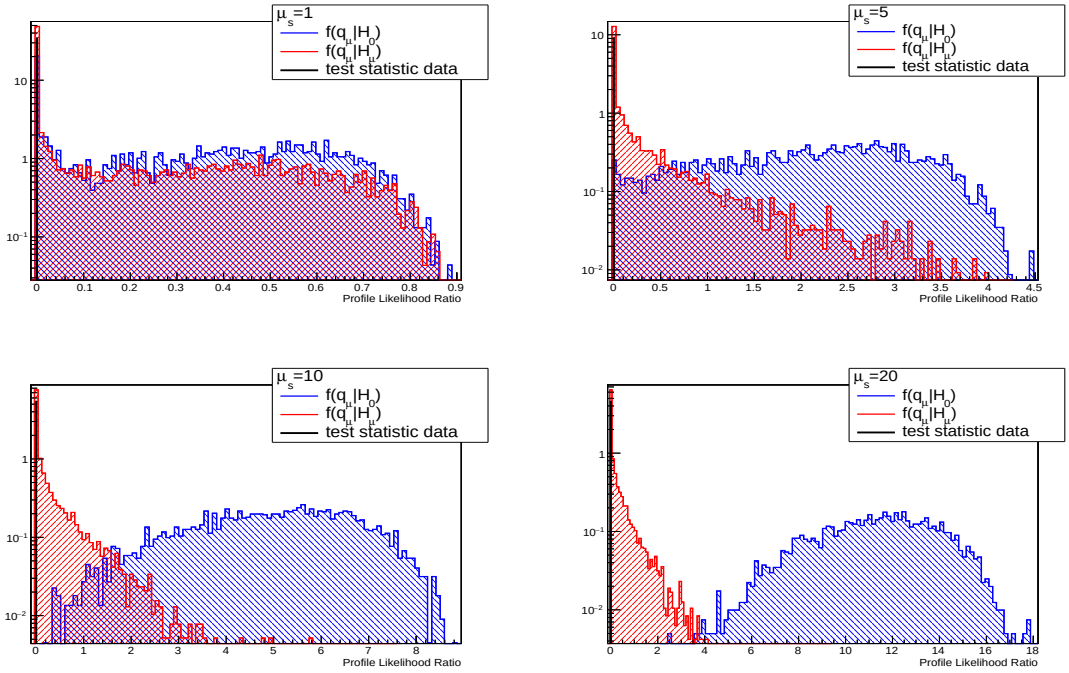

Figure 4.7: RooStats implementation: probability distributions of the test statistic q_μ under signal (red) and background-only (blue) hypothesis for different μ_s tested: 1, 5, 10, 20. The black vertical line is the q_μ^{obs} relative to a single simulated data set.

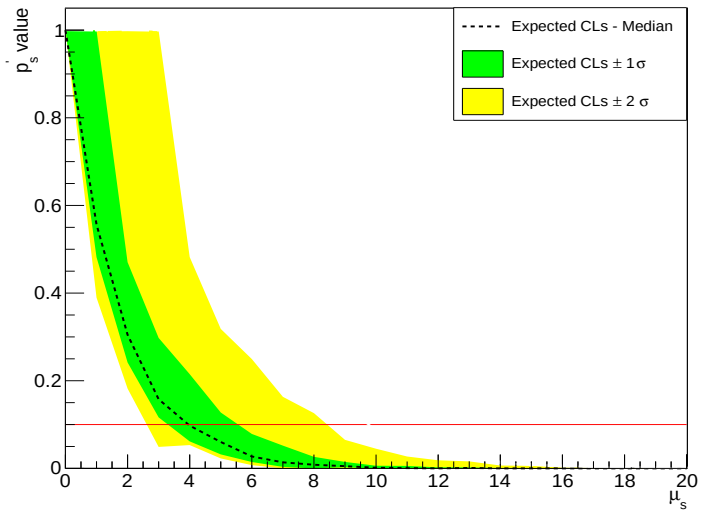

Figure 4.8: RooStats result: values of p'_s as function of signal hypotheses μ_s. The blue curve indicates the p'_s calculated with the median of $f(q_\mu|H_0)$, while the green and yellow bands comes from the calculation of p'_s with the $\pm 1\sigma$ and $\pm 2\sigma$ quantiles of $f(q_\mu|H_0)$. The horizontal red line marks out the threshold corresponding to 90% CL.

Chapter 5

XENON1T: expected signal and background

In this chapter we describe how the expected recoil energy spectra of WIMPs are estimated for a wide range of hypothesized WIMP masses (section 5.1). We also present the background estimates for XENON1T in section 5.2 and discuss the conversion of recoil energy into the S1 and S2 signals, which allows to obtain the S1 spectra used in the model. The definition of the complete statistical model is then presented in section 6.1 through the definition of the two observables S1 and Y.

5.1 WIMP-nucleon interaction rate

The computation of the expected interaction rate of WIMPs is clearly a key feature when approaching the Dark Matter direct detection issue. Moreover, the spectral information about the recoil energy of WIMP-nucleon scatterings is also mandatory in the statistical analysis of both simulated and real data. In order to estimate such spectra, one needs to fix the astrophysical model which supplies all necessary parameters about WIMPs characteristics. A standard assumption [88] is to consider WIMPs to be trapped into a Dark Matter galactic halo, whose velocities are distributed according to the Maxwell-Boltzmann distribution[1]. The range of hypothesized WIMP mass (m_χ) spans from the scale of GeV/c^2 up to the order of 1 TeV/c^2.

The local Dark Matter density is usually taken equal to $\rho_0 = 300$ MeV/cm^3 [89], while the most probable WIMP velocity we will use is $v_0 = 220$ km/s [90]. In principle, the Maxwell-Boltzmann distribution provides WIMP velocities up to pretty high values. However, Dark Matter is thought to be gravitationally confined in the galactic halo, thus WIMPs cannot move faster than the escape velocity, which we fix at $v_{escape} = 544$ km/s [90].

[1] Cosmological simulations of galaxy formation show up minor departures from the simplest case of a Dark Matter gas in thermal equilibrium.

Table 5.1: Parameters used in the estimation of total and differential WIMP-nucleon interaction rate

Parameters of WIMP interaction model		
WIMP density	ρ_0	300 MeV/cm^3
Most probable WIMP velocity	v_0	220 km/s
WIMP escape velocity	v_{escape}	544 km/s
Solar system velocity	v_{Sun}	250 km/s
Mass number of target atoms	A	131.293
WIMP-nucleon cross section	σ	2×10^{-45} cm^2

In this work we study the spin-independent (SI) interactions of WIMPs and we will indicate the SI cross section for elastic WIMP-nucleon scatterings simply as σ. The cross section for a WIMP scattering off a nucleus, σ_N, with mass number A, can be expressed in terms of σ through [91]

$$\sigma_N \simeq A^4 \sigma \,, \tag{5.1}$$

which is an acceptable approximation for our purpose, since we assume that WIMPs do not distinguish protons from neutrons, i.e. they both have the same coupling constant.

In the following, the interaction rate of WIMPs on xenon atoms along with the recoil energy spectrum are estimated starting from the simple case of detector at rest in the galaxy and then introducing more accurate details (section 5.1.2). We initially study the interaction of a WIMP of 100 GeV/c^2. We also compare recoil energy spectra coming from different computational methods for the cases of m_χ=10, 100, 1000 GeV/c^2 (section 5.1.3). Finally, we show the WIMP spectra obtained for several masses and a reference estimate of the expected number of signal events in the XENON1T experiment for a given exposure (section 5.1.4). In this section we take a hypothesized value of the WIMP-nucleon cross section equal to $\sigma = 2 \times 10^{-45}$ cm^2, just to set the calculation. However, the cross section acts only as a scaling factor on the recoil energy spectra. The values of parameters used in the calculations are summarized in table 5.1.

5.1.1 Simplified estimation

Having set up the main input parameters, the first ingredient we need in order to implement the calculation of nuclear recoil energy spectrum is the distribution of galactic WIMP velocities. We said that the WIMP halo is assumed to be a gas in thermal equilibrium, hence each component v_i of WIMP velocity is distributed according to a gaussian p.d.f. with mean value equal to zero. The Maxwell-Boltzmann shape for $|\overrightarrow{v}| = \sqrt{v_x^2 + v_y^2 + v_z^2}$ simply comes from the product of the three gaussian distributions of v_x, v_y and v_z. Figure 5.1 shows the WIMP velocity distribution along with one of its component.

The interaction rate of WIMPs with the target is given by

$$R = N \cdot \phi \cdot \sigma_N \,, \tag{5.2}$$

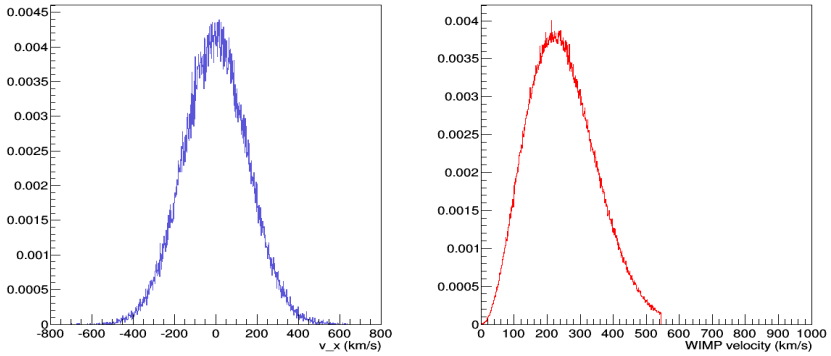

Figure 5.1: (Left) Normalized gaussian distribution of v_x with $\langle v_x \rangle = 0$ and $\sigma = v_0/\sqrt{2}$; (Right) Maxwell-Boltzmann distribution of v, cut off at $v_{escape} = 544$ km/s.

where

- $N = \frac{M_{target}}{m_{Xe}}$ is the number of target atoms, with M_{target} total target mass and m_{Xe} mass of a xenon atom;
- $\phi = \frac{\rho_0}{m_\chi}\langle v \rangle$ is the WIMP flux.

It has been demonstrated that the *differential rate*, i.e. the spectrum for any recoil energy of scattered nuclei, can be expressed as [92, 93]:

$$\frac{dR}{dE_R} = \frac{\rho_0 \, \sigma \, A^2}{2\mu_p^2 \, m_\chi} \int_{v_{min}}^{v_{escape}} \frac{f(v)}{v} \, \mathrm{d}v \, . \tag{5.3}$$

Here, μ_p is the reduced mass between a proton and a WIMP, that is $\mu_p = \frac{m_p \, m_\chi}{m_p + m_\chi}$, while the integral involves the WIMP velocity p.d.f., $f(v)$, over all values of v which can produce a certain recoil energy E_R. A xenon atom scattered by a WIMP of velocity v, gains a recoil energy equal to

$$E_R = \frac{\mu_N^2 v^2 (1 - \cos\theta)}{m_N} \, , \tag{5.4}$$

where μ_N is the WIMP-Xenon reduced mass and θ the scattering angle. Therefore v_{min}, the minimum WIMP velocity able to cause a recoil energy of E_R, is found considering the case of head-on collision ($\theta = 180°$):

$$v_{min} = \sqrt{\frac{m_N E_R}{2\mu_N^2}} \, . \tag{5.5}$$

On the other hand, the maximum velocity simply corresponds to v_{escape}.

The *total interaction rate* can be easily obtained by integrating over all possible recoil energies:

$$R = \int_{E_R^{min}}^{E_R^{max}} \left(\frac{dR}{dE_R} \right) dE_R \, . \tag{5.6}$$

Note that equations (5.3) and (5.6) refer to a rate per unit target mass. For a given extensive xenon target of total mass M_{target}, these rates must be multiplied by M_{target}. In the contest of

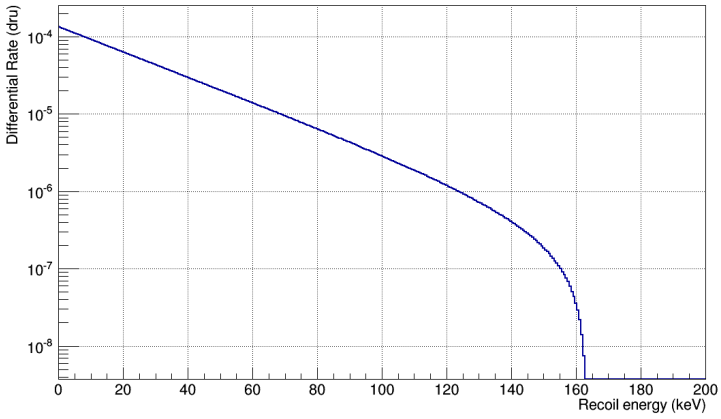

Figure 5.2: Differential rate of a 100 GeV/c^2 WIMP obtained from the simplified estimation.

Dark Matter research, the differential rate is usually expressed in *dru* units, defined as number of events/kg/keV/day.

At this point, the recoil energy spectrum for a WIMP mass of 100 GeV has been produced (figure 5.2) evaluating the differential rate for different E_R between zero and the maximum recoil energy allowed (coming from a head-on collision of a WIMP with $v = v_{escape}$), which in this case is approximately 163 keV.

Computing the integral of this differential rate, $R = 3.53 \cdot 10^{-3}$ events/kg/day is obtained as total expected interaction rate if we assume, e.g. a cross section σ equal to 2×10^{-45} cm^2.

5.1.2 Full calculation

The previous estimation has been achieved leaving out two important features of the problem we are dealing with. The first is related to the motion of our detector, since the Earth rotates in the galaxy along with the solar system, the second regards the cross section σ, which must be corrected for diffractive effects due to the finite size of the target nucleus, especially for fast WIMPs.

Detector motion

We are interested in the calculation of interaction rate within our reference frame (say *LAB frame*). Such a frame has a rotational motion within the galaxy: we consider here only the main motion of the solar system as a whole around the galactic center, neglecting the Earth's revolution and rotation. Thus, in the LAB frame the WIMP velocity has always an additional term along one direction. This direction obviously changes continuously, but for our aim we can simply add the velocity of LAB frame, called v_{Sun}, to one of the WIMP velocity components. We are, indeed, interested only in the magnitude of v.

The introduction of this new element causes the increase of maximum WIMP velocity, as the Maxwell-Boltzmann distribution is stretched toward higher values, from v_{escape} to $v_{max} =$

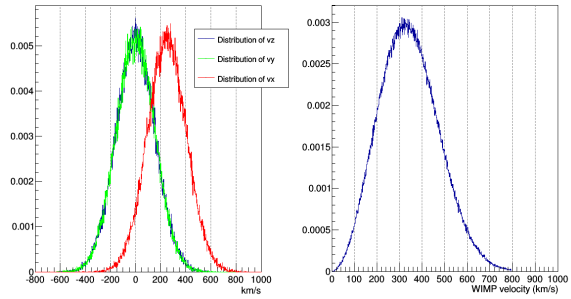

Figure 5.3: (Left) Distribution of v_x (red), v_y (green), v_z (blue) with $\sigma = v_0/\sqrt{2}$ and $\langle v \rangle = 0$ for v_y and v_z, while $\langle v_x \rangle = v_{Sun}$ for v_x; (Right) Distribution of $|\overrightarrow{v}| = \sqrt{v_x^2 + v_y^2 + v_z^2}$

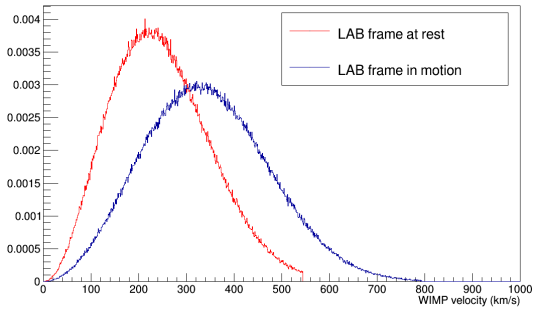

Figure 5.4: Distributions of $|\overrightarrow{v}|$ with the LAB reference frame at rest (red) in the galaxy and in motion with velocity v_{Sun} (blue).

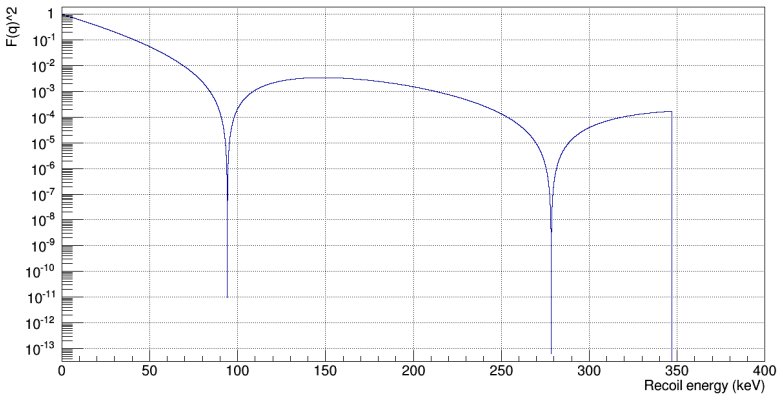

Figure 5.5: Square of the nuclear form factor for xenon target nuclei.

$v_{escape}+v_{Sun} = 794$ km/s. Here we use the standard average value of 250 km/s for the parameter v_{Sun} [94]. From figure 5.4, we can see how the p.d.f. of the WIMP velocity in the detector reference (LAB) frame vary with respect to the velocity seen in the galactic reference frame (i.e. co-moving with the galaxy).

Nuclear form factor correction

The cross section σ_N, given in (5.1), needs to be corrected for quantum effects which reduce the value obtained from a classical approach. The ratio between the proper and the classical cross section is the square of the so-called *nuclear form factor*, $F(q)$, which depends on the transferred momentum in the collision $q = \sqrt{2m_N E_R}$. The Helm parametrization of the spin-independent form factor [95, 96] can be written as

$$F(q) = 3\frac{\sin(qr) - qr \cdot \cos(qr)}{(qr)^3} e^{-\frac{1}{2}(qs)^2} , \tag{5.7}$$

where r is a constant with dimensions of a length. It is given by $r = \sqrt{\left(c^2 + \frac{7}{3}\pi^2 a^2 - 5s^2\right)}$, with $c = \left(1.23 \cdot A^{1/3} - 0.6\right)$ fm, $a = 0.52$ fm and $s = 0.9$ fm.

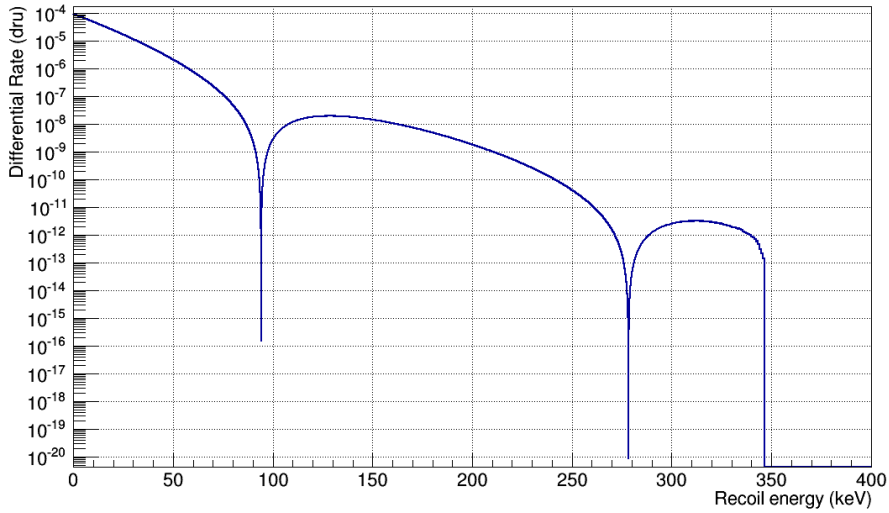

Figure 5.6: Differential rate of the interaction of 100 GeV/c^2 WIMP mass with a xenon target, after the LAB frame and form factor corrections.

For very low energetic WIMPs, we have $F(q) \simeq 1$, but when their velocity is high enough to reduce the De Broglie wavelength to values comparable with the nuclear radius, then WIMPs become able to see the internal structure of the nucleus. Therefore the scattering can no longer be outlined as a collision on a rigid sphere and diffraction-like effects begin to arise causing a suppression of the cross section. The form factor has been calculated for the range of E_R of interest and it is shown in figure 5.5.

Considering the two corrections mentioned above, the proper recoil energy spectrum can be easily computed introducing few adjustments in the equation (5.3). The square of nuclear form factor appears as a multiplicative factor, the integral over WIMP velocities runs up to $v_{max} = v_{escape} + v_{Sun}$ and the modified p.d.f. $f(|\overrightarrow{v} + \overrightarrow{v_{Sun}}|)$ must be taken:

$$\frac{dR}{E_R} = \frac{\rho_0 \, \sigma \, A^2}{2\mu_p^2 \, m_\chi} \, F^2(q) \int_{v_{min}}^{v_{max}} \frac{f(|\overrightarrow{v} + \overrightarrow{v_{Sun}}|)}{v} \, \mathrm{d}v \, . \tag{5.8}$$

The resulting recoil energy spectrum for a WIMP of mass 100 GeV/c^2 is shown in figure 5.6. The end point increased from 163 keV to 347.2 keV as a consequence of the LAB frame correction. The total rate obtained from this distribution amounts to $R = 1.35 \cdot 10^{-3}$ events/kg/day.

5.1.3 Cross checks for different WIMP masses

We carry out analogous calculations of the differential rate also for hypothesized WIMP masses of 10 GeV/c^2 and 1 TeV/c^2. Moreover, we check the recoil energy spectra following a different procedure: after having sampled a WIMP velocity v according to its p.d.f., a nuclear recoil energy E_R (below the maximum corresponding to that specific velocity) is sampled according

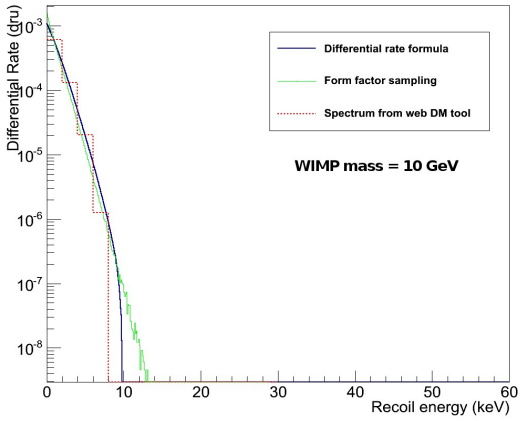

(a) WIMP mass $m_\chi = 10$ GeV/c^2

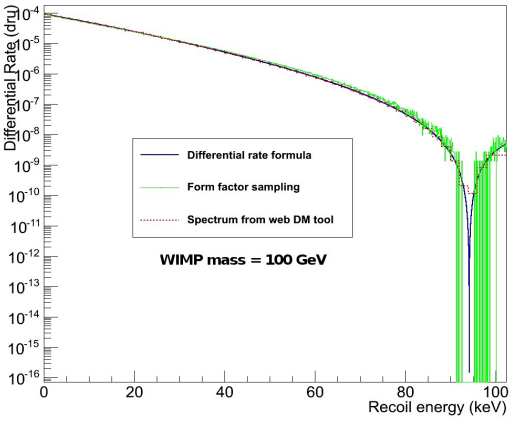

(b) WIMP mass $m_\chi = 100$ GeV/c^2

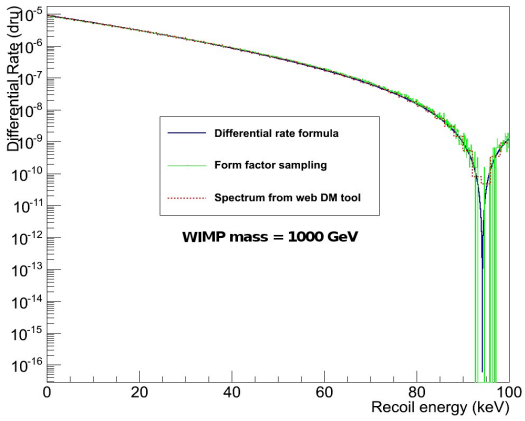

(c) WIMP mass $m_\chi = 1000$ GeV/c^2

Figure 5.7: Differential rates of WIMP-nucleon interaction computed with three different methods: from the differential rate formula (blue), via the "form factor sampling" procedure (green) and from the Dark Matter tool (dashed red line).

to the form factor distribution and then a histogram is filled with a large number of such recoil energy entries.

The resulting distributions are then compared to the spectra supplied by DMMC [97] (a general purpose Dark Matter tool publicly available on web) in which we set the same input parameters used in our study. Figure 5.7 show the energy recoil spectra for m_χ=10, 100 and 1000 GeV/c^2 obtained with the three procedures: computing the differential rate (as in section 5.1.2), with the method just described in this section (via E_R sampling through the form factor distribution, that we can call "form factor sampling") and using the Dark Matter web tool.

The three methods produce compatible recoil spectra in the wide range of WIMP masses

Table 5.2: Total interaction rates for different WIMP masses and for a WIMP-nucleon cross section equal to 2×10^{-45} cm^2.

WIMP mass m_χ (GeV/c^2)	**Total rate** R (events/kg/day)
10	$1.53 \cdot 10^{-3}$
100	$1.35 \cdot 10^{-3}$
1000	$0.16 \cdot 10^{-3}$

investigated. An exception is observed in the plot for $m_\chi = 10$ GeV/c^2, where the "form factor sampling" curve lies above the two others near the maximum recoil energy. It should be noted that the web DM tool supplies only few points in this case, causing the red line to be rather fragmented. However, values from the DM tool are very close to those obtained using the differential rate formula (5.8).

5.1.4 Conclusive results

We computed the WIMP interaction rate expected in a direct detection experiment using xenon as target, under the astrophysical assumptions summarized in table 5.1 and for a 100 GeV/c^2 WIMP. We carried out the calculation in a simplified approach, then we introduced the motion of our detector through the galaxy and the nuclear form factor which supplies the correct WIMP-nucleon cross section. The total interaction rates obtained for $m_\chi = 100$ GeV/c^2 and $\sigma = 2 \times 10^{-45}$ cm^2 are

- $R = 3.53 \cdot 10^{-3}$ events/kg/day (simplified calculation),
- $R = 1.35 \cdot 10^{-3}$ events/kg/day (full calculation).

While the motion of LAB frame increases the relative velocity in WIMP-xenon collisions, thus enhancing the maximum recoil energy and consequently the total rate, the form factor correction significantly suppresses the cross section, causing an overall reduction of 62% for the total interaction rate.

In table 5.2, the total interaction rates computed for three different hypothesized WIMP masses are reported. As expected, the overall number of interactions per unit exposure (kg·day) decreases with the WIMP mass; since one assumes a fixed WIMP density, the number of WIMPs in the galactic halo is larger for lower m_χ. Hence, the WIMP flux ϕ increases with the considered mass m_χ and this leads to a larger total rate, as can be easily understood from the definition of R (5.6).

A collection of several WIMP differential rates for masses in the range [5, 1000] GeV/c^2 is shown in figure 5.8. Such spectra are obtained assuming a cross section $\sigma = 2 \times 10^{-45}$ cm^2. It is possible to use them in order to estimate the expected number of signal events (WIMP-nucleon scatterings) in a given exposure. Table 5.3 shows these numbers for an exposure of 2 tonne·years

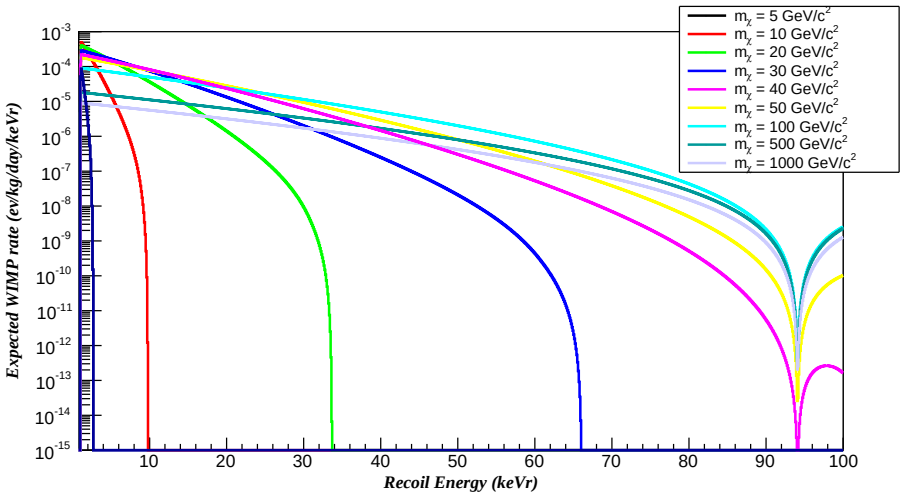

Figure 5.8: Differential WIMP-nucleon interaction rate for a sample of masses m_χ between 5 and 1000 GeV/c^2 with cross section $\sigma = 2 \times 10^{-45}$ cm^2.

and in the recoil energy window [5, 50] keV, which is approximately the energy range where XENON1T looks for DM events.

WIMP mass (GeV/c^2)	**expected signal events**
5	0
10	9.6
20	382.1
30	730.9
40	875.3
50	903.3
100	684.9
500	168.8
1000	85.9

Table 5.3: Number of expected WIMP-nucleon interaction events inside the recoil energy window [5, 50] keV for an exposure of 2 tonne·years and assuming a cross section $\sigma = 2 \times 10^{-45}$ cm^2.

The lack of events from very light WIMPs is explained by the lower bound of the energy range selected, meaning, e.g., that 5 GeV/c^2 WIMPs can not produce recoils larger than 5 keV.

5.2 Background estimation

To define the XENON1T statistical model we must distinguish between *signal* events, due to WIMP-nucleon interactions, and *background* events originated by other physics channels. In the previous section, we estimated the pattern of energy spectra produced by WIMPs under the assumption of a standard galactic Dark Matter halo model. Of course, it is equally important

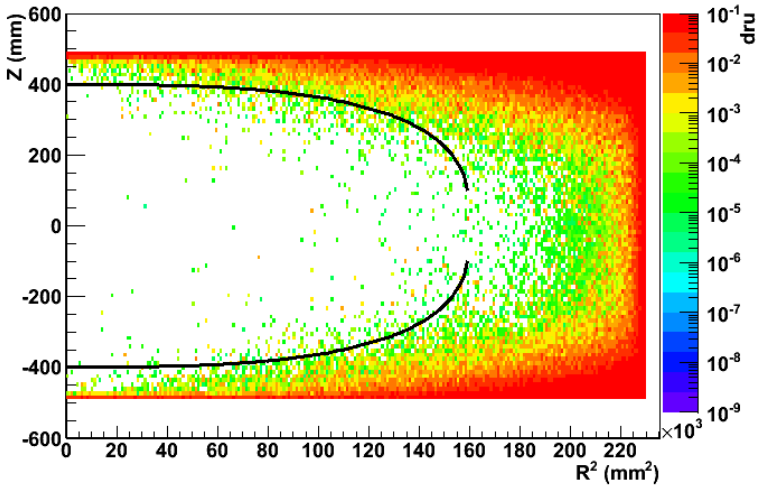

Figure 5.9: Electromagnetic background events distribution inside the XENON1T TPC, considering the [2, 12] keV$_{ee}$ energy region. The black line represents the 1 tonne fiducial volume.

to estimate the background behavior too. All sources of background have been studied via a detailed MC simulation of the detector geometry and the particle interactions in the materials using the GEANT4 software toolkit [98]. They have been extensively discussed in [99]; here we simply recall the main features.

Basically, background events mimic, to some extent, the features of signals produced by WIMPs. Therefore, the estimation of the background for the XENON1T experiment has been carried out by selecting, among events generated by standard particles, those satisfying the same requirements applied in the WIMP search, namely:

- a single scattering interaction;
- vertex of interaction inside the fiducial volume (FV);
- deposited energy in the WIMP search region.

The first condition is justified by the guess that WIMPs would produce not more than one interaction inside the detector, since they are highly "weakly interacting particles". In the present study we fix a **1 tonne FV** defined as an ellipsoid centered in the middle of the TPC active volume. It is chosen such that the distance from the TPC inner walls is at least 4 cm. The fiducial volume guarantees a substantial reduction of internal background thanks to the self-shielding properties of LXe. Moreover, the region of interest (ROI) in the S1 parameter is defined as the **[3, 70] pe** window. The lower constrain derives from the analysis of XENON100 detector performances, which points out the presence of disturbing instrumental noise below 3 photoelectrons. The upper end comes from considerations about the end point of the WIMP recoil energy: below 70 pe, corresponding to about 50 keV, we found that 95% of the spectrum of a 100 GeV/c^2 WIMP is contained. In terms of the ER and NR energy scales, the [3, 70] pe interval corresponds to about [2, 12] keV$_{ee}$ (for ER) and to [5, 50] keV$_{nr}$ (for NR).

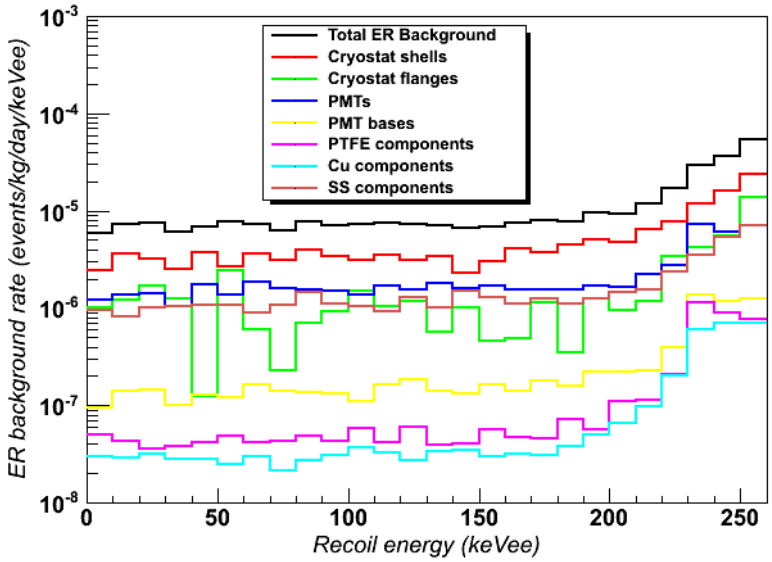

Figure 5.10: Recoil energy spectra of the ER background in 1 tonne fiducial volume for several detector materials. Each curve is obtained summing over all the active isotopes.

Background events can be divided in two main categories: electronic (*ER*) and nuclear recoils (*NR*) depending on whether the interaction with a xenon atom involves an orbital electron or the nucleus.

5.2.1 ER background

From the detector materials

A source of ER background comes from the radioactivity present in the detector materials, in particular those closest to the LXe target. The most dangerous background is from the gamma emitted in the ^{238}U and 232Th radioactive chains, and the decay of ^{60}Co, ^{40}K and ^{137}Cs . The material contaminations have been accurately measured using a variety of complementary techniques and dedicated measurements. The decays from each isotope and each detector component have been generated via MC [99] and the results scaled accordingly to the contamination and the mass of that component.

Since the gammas come from outside the active volume of the TPC, it is possible to reduce this background by applying position cuts, thus selecting an inner fiducial volume, see figure 5.9. The residual dangerous events are those which reach the internal volume of the active region, produce a low energy Compton scatter and leave the detector without other interactions.

The expected recoil energy spectra of ER background from the materials are collected in figure 5.10.

Background diffused in the LXe target

Other important sources of ER background are also originated inside the LXe target, due to residual radioactive impurities. Such ER background is uniformly distributed in the whole active volume, thus the selection of a FV is not effective in reducing it. The dangerous isotopes found in natural xenon are ^{85}Kr, ^{222}Ra and ^{136}Xe (which undergo double beta decay). To lower their contribution it is necessary to reduce their concentration using proper purification (for ^{85}Kr and ^{222}Ra) and depletion (for ^{136}Xe) techniques.

Another source of ER background uniformly distributed inside the LXe active volume is given by the elastic scattering of solar neutrinos (in particular those from the pp chain) off electrons.

The energy spectrum of ER background for the XENON1T experiment from all sources is shown in figure 5.11. Table 5.4 summarizes the results in terms of number of expected ER background events before any discrimination cut.

Ultimately, the ER background can be strongly reduced through the discrimination of NR from ER events thanks to their different response in terms of S1 and S2 signals. In XENON100 it was achieved a 99.75% ER discrimination, while keeping a 40% NR acceptance [27].

Source	**background (ev/kg/day/keV)**	**background (ev/y)**	**% contribution**
materials	$(7.27 \pm 0.34) \cdot 10^{-6}$	26.5 ± 1.3	20.5
^{222}**Rn**	$(8.88 \pm 1.78) \cdot 10^{-6}$	32.4 ± 6.5	25.1
^{85}**Kr**	$(7.64 \pm 1.53) \cdot 10^{-6}$	27.9 ± 5.6	21.6
solar neutrinos	$(8.89 \pm 1.78) \cdot 10^{-6}$	32.4 ± 6.5	25.2
$2\nu2\beta$ **decay**	$(2.70 \pm 0.54) \cdot 10^{-6}$	9.9 ± 2.0	7.6
Total	$\mathbf{(3.54 \pm 0.30) \cdot 10^{-5}}$	$\mathbf{129 \pm 11}$	**100**

Table 5.4: Summary of the expected ER background for the XENON1T experiment before discrimination cuts. The ev/y background is evaluated for a 1 tonne fiducial volume and in the [2, 12] keV energy window. The errors on the intrinsic sources are 20% due to the uncertainties on the low energy part of the recoil energy spectra.

5.2.2 NR background

Elastic scatterings of neutrons off xenon nuclei generate a signal which is, on an event-by-event basis, indistinguishable from that of WIMPs. In case of single scatter inside the FV and low energy recoil, this kind of interaction defines the NR background for XENON1T. Fast neutrons are more penetrating than γ-rays in LXe, since their mean free path is of the order of tens of cm. Consequently, it is more difficult to shield them and their probability to have a single scatter in the LXe active volume is higher than γ. The presence of ^{238}U, ^{235}U and ^{232}Th in the detector materials generates *radiogenic neutrons* in the MeV energy range through spontaneous fission (SF), mainly from ^{238}U and (α, n) reactions induced by the α emitted along the chains.

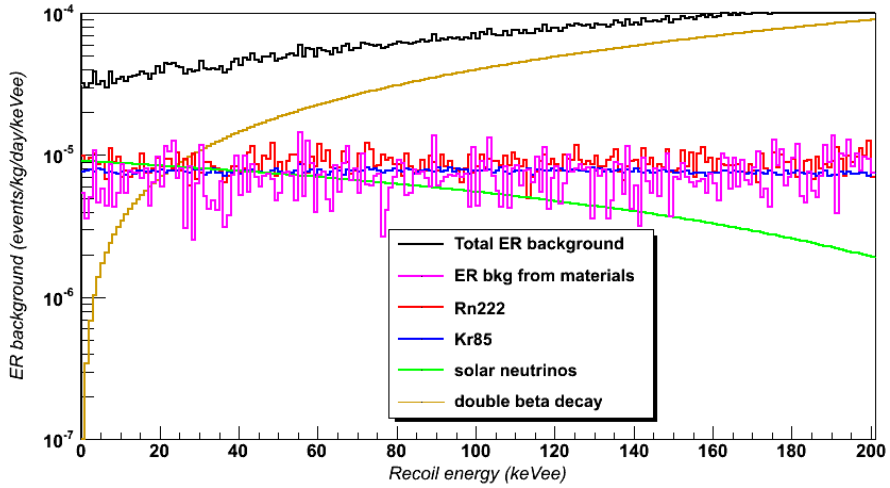

Figure 5.11: Energy spectra of ER background sources. The black curve represents the distribution of the total ER background. Different contributions are also specified: from materials (pink), from solar neutrinos (green) and from intrinsic LXe contaminations, i.e. ^{222}Rn (red), ^{85}Kr (blue), $2\nu2\beta$ decay (orange).

Additionally, *cosmogenic neutrons*, with energies extending to tens of GeV, are produced by muons along their path through the rock into the underground laboratory and through the materials that surround the detector. However, muon-induced neutrons can be tagged with high efficiency thanks to the Muon Veto system [100].

Radiogenic neutron yield and spectra have been estimated through the dedicated SOURCES-4A code [101, 102]; they are propagated through the experiment via GEANT4 MC simulation; then their interactions inside the active volume have been analysed with the usual selection cuts. The results, again scaled for the contamination of the materials, are shown in figure 5.12.

Astrophysical neutrinos, in particular those produced via the ^{8}B chain in the Sun, also contribute to the NR background since they can undergo to *Coherent Neutrino-Nucleon Scattering* (CNNS), a process predicted by the Standard Model which has not yet been observed, mainly because of the lack of detectors with enough target mass and low background. This is an irreducible background which imply a ultimate limit to the WIMP sensitivity of direct experiments [103].

The differential interaction rate of CNNS due to solar and atmospheric neutrinos in a xenon target is reported in figures 5.13 and 5.12 (superimposed on the neutron spectrum).

The total number of events in the [5, 50] keV energy range from neutrons is (0.5 ± 0.1) events per year in 1 tonne fiducial volume. The amount of interaction from CNNS in the same energy range is negligible; however, given the Poisson fluctuations in the number of emitted and detected photons (which will be discussed in the next section) it may happen that low energy NR can be detected in the chosen region of interest in S1. Given the large number of expected NR from CNNS, about 170 event per tonne·year with recoil energy >1 keV, and their steep spectrum, the effect is even more relevant and will be quantified in chapter 6.

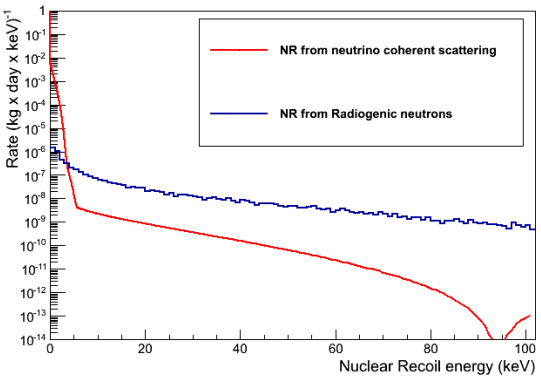

Figure 5.12: Energy spectra of NR background originated from radiogenic neutrons emitted by the detector materials (blue line) and from neutrinos undergoing CNNS (red line).

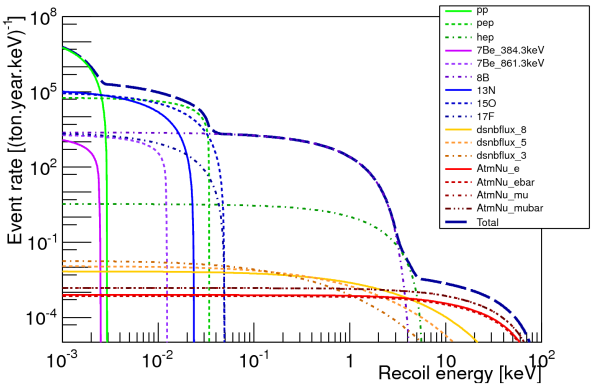

Figure 5.13: Recoil energy spectrum of Coherent Neutrino-Nucleon Scattering events. The contributions of each type of solar, diffused supernovae and atmospheric neutrinos are also shown.

5.3 Conversion from energy to S1 and S2 signals

As already said, we characterize the XENON1T statistical model through two observables: the S1 signal and the discrimination parameter Y. Hence, having established the assumptions under which signal and backgrounds will be treated in our model, we need to know their expected distributions in the observables S1 and Y. To this purpose, we need to associate the recoil energy to the amplitude of the produced S1 and S2 signals[2].

Electromagnetic and nuclear recoils lead to different scintillation and ionization. The output in terms of light (S1) and charges (S2) collected after an event of given energy is not the same in case of electronic or nuclear recoils. Hence, the proper conversion of the deposited energy during a collision into the measured S1 and S2 signals is mandatory.

5.3.1 Light and charge yield

Scatterings off xenon atoms can cause, in general, both excitation and ionization , with consequent emission of scintillation light and free charges. Hence, the basic output of a recoil event can be treated in terms of the number of photons and electrons produced, which is characterized by the quantities called *light yield* (L_Y) and *charge yield* (Q_Y), respectively. The photon and electron yields are estimated following two different procedures in case of electromagnetic or nuclear recoils.

[2]The observable Y we use in the statistical model is an idealization of the discrimination parameter $\log_{10}$(S1/S2). In this section we deal with the conversion into both S1 and S2. However, only the S1 conversion is actually used to define the spectra of the model, while the Y spectra are chosen as standard gaussian p.d.f.s, even if with mean and variance chosen to reproduce a good approximation of the real discrimination parameter distributions.

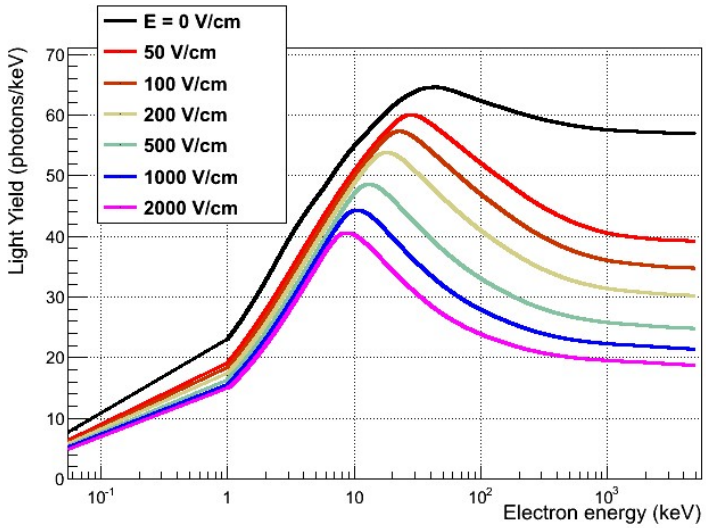

Figure 5.14: Photon yield of ER interactions as function of the deposited energy for different magnitudes of the electric field applied.

Electromagnetic recoils

For an ER event with a certain deposited energy, the number of *quanta* (sum of photons and electrons) generated is extracted from the well established model of low-energy recoils in LXe provided by the NEST (Noble Element Simulation Technique) package [104] for GEANT4. It comes out a constant conversion factor of 73 *quanta*/keV.

Given a deposited energy E_d, the number of quanta produced is gaussian distributed, with mean value $N_{quanta} = E_d \cdot 73$ *quanta*/keV and variance $E_d \cdot 73 \cdot 0.03$ [105]. The mean number of the photon component, i.e. the light yield $L_{Y,er}$ is also provided by NEST and depends on E_d and the electric field applied to the TPC (see figure 5.14). The number of electrons is then simply obtained as $N_{e^-} = N_{quanta} - N_\gamma$.

Nuclear recoils

In nuclear recoils the energy deposited by the incoming particle is transferred to the target nucleus as kinetic recoil energy E_r. Such nucleus will then lose such energy via collisions with other Xe atoms. A collision can lead to ionization or scintillation, like in ER events, or just to the dissipation of kinetic energy as heat in the medium. For a given deposited energy, the number of quanta produced by a NR is smaller than the one from an ER, since part of the energy goes to heat.

For NR events, the charge and light yields are determined through the comparison between XENON100 calibration measurements [106], with AmBe sources, and MC simulations. The obtained curves for L_Y and Q_Y of NR are shown in figures 5.15 and 5.16. The number of photons and electrons produced in a nuclear recoil is thus calculated as $N_\gamma = E_r \cdot L_{Y,nr}(E_r)$ and $N_{e^-} = E_r \cdot Q_Y(E_r)$.

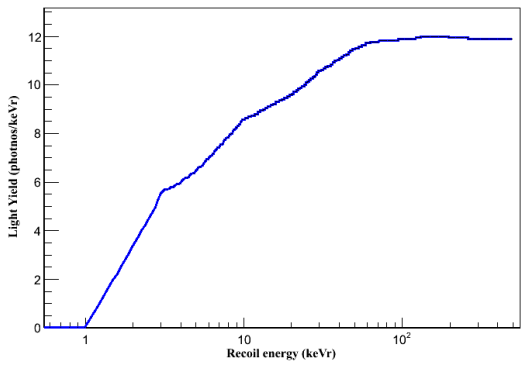

Figure 5.15: Photon yield of NR interactions as function of the recoil energy, measured from XENON100 AmBe calibration data [106].

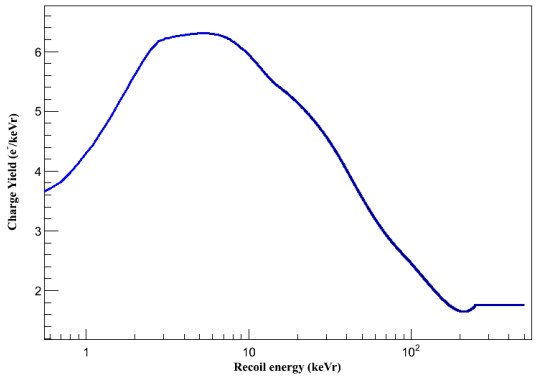

Figure 5.16: Charge yield of NR interactions as function of the recoil energy, measured from XENON100 AmBe calibration data [106].

It is important to clarify that the scintillation yield $L_{Y,nr}$ for nuclear recoils is significantly different from that for electronic recoils, $L_{Y,er}$. From the experimental point of view, what we measure is the *relative scintillation efficiency* [107, 108], defined as

$$\mathcal{L}_{eff}(E) = \frac{L_{Y,nr}(E)}{L_{Y,er}(E = 122 \text{ keV})} , \tag{5.9}$$

which express the NR light yield relatively to the one given by an ER of a photoabsorbed 122 keV γ-ray at zero electric field, corresponding to 63.4 *photons*/keV. Therefore, the NR scintillation yield $L_{Y,nr}$ is actually obtained by inverting (5.9).

5.3.2 Relative scintillation efficiency for nuclear recoils

The conversion from energy to S1 signal and vice versa is a crucial and not trivial task in the study of nuclear recoils. The phenomenology of such interactions is investigated through experimental measurements of $\mathcal{L}_{eff}$ as function of the recoil energy, from which we can establish the mean number of photons produced. Since the experimental measurement of $\mathcal{L}_{eff}$ is not simple, it represents the most important source of systematic uncertainties for XENON1T.

Direct measurements of $\mathcal{L}_{eff}$ are carried out using collimated beams of neutrons of known energy E_n, which undergo to elastic scatterings off xenon atoms. The recoil energy E_r is calculated from

$$E_r \simeq 2E_n \frac{m_n M_{Xe}}{(m_n + M_{Xe})} (1 - cos\theta) , \tag{5.10}$$

where m_n and M_{Xe} are the neutron and xenon atom masses, and θ is the scattering angle, which is experimentally measured. Hence, it is possible to know the recoil energy and to observe the related scintillation response.

Taking into account all direct measurements of $\mathcal{L}_{eff}$ [109–115], its dependence on the recoil energy is assessed from a gaussian fit, leading to the plot showed in figure 5.17. Below 3 keV

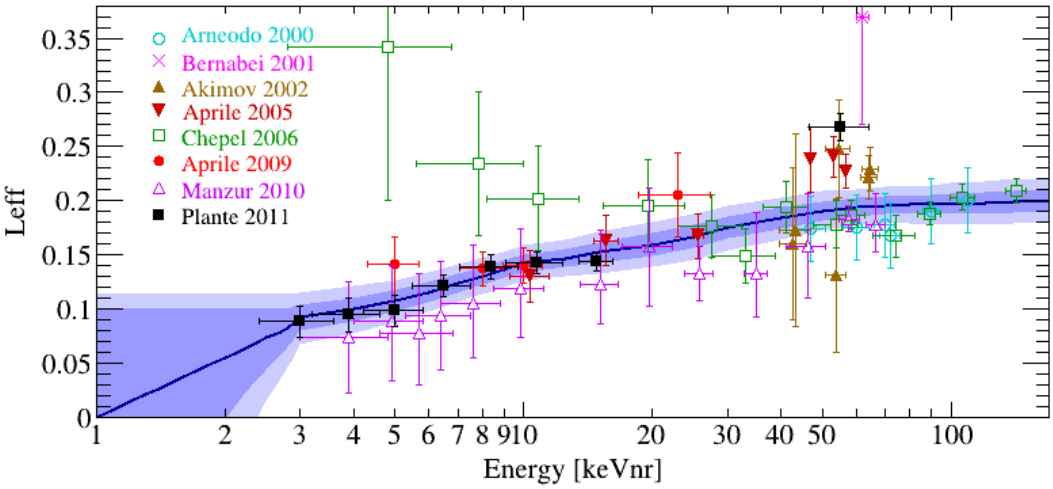

Figure 5.17: $\mathcal{L}_{eff}$ model defined by the gaussian fit (solid line) of all direct measurements [109–115] and the 1σ and 2σ bands (shaded dark and light blue, respectively).

no experimental points are available, hence the uncertainty spreads in this region. The upper bands are fixed to the value they have at 3 keV in order to reflect the guess that $\mathcal{L}_{eff}$ should not increase with lower energies. The median $\mathcal{L}_{eff}$ is exponentially extrapolated down to 1 keV, below which it is set to zero.

5.3.3 S1 and S2 yields

From the number of photons and electrons produced by ER and NR events, we can now estimate the corresponding response as S1 and S2 signals, i.e. the number of photoelectrons experimentally observed due to scintillation (S1) and ionization (S2). To properly carry out the conversion, we must take into account all those efficiencies that affect the survival probability of γ and e^- inside the TPC and the signal generation in the PMTs.

S1 signal

The amplitude of the S1 signal is related to the photons produced after ER or NR. The optical properties of the TPC, i.e. the medium and the surrounding structure, characterize the probability for a scintillation γ (178 nm) to reach one PMT. Such property is called *light collection efficiency* (LCE) and in general depends on the position of the primary event. Once a certain number of photons have reached the PMTs, the number of photoelectrons that will form the S1 signal is determined through the *quantum* (QE) and *collection efficiency* (CE) of the phototubes. Therefore the detector performance can be characterized by the global quantity named *detection efficiency*:

$$DE = LCE \cdot QE \cdot CE\,. \tag{5.11}$$

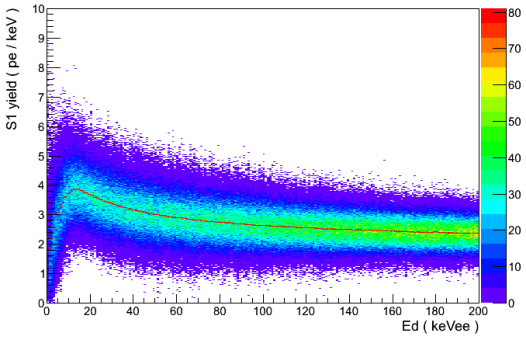

Figure 5.18: S1-yield as function of the energy for **electronic recoils**.

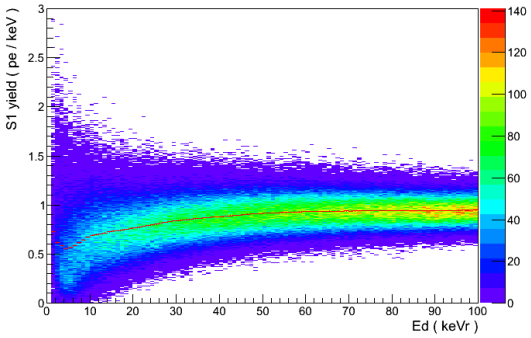

Figure 5.19: S1-yield as function of the energy for **nuclear recoils**.

The average values of these efficiencies for the XENON1T experiment are: LCE=38%, QE=36% and CE=90%.

The number of photoelectrons detected per unit energy is said *S1-yield* and is given by

$$S1_Y(E) = L_{Y,er(nr)} \cdot DE \,, \tag{5.12}$$

where the proper light yield is considered according to the nature of the event (ER or NR). The S1-yield for a γ of 122 keV at zero electric field is equal to 7.8 pe/keV$_{ee}$.

The different scintillation yields of ER and NR imply that from the same S1 signal, we get two different energy values when reconstructing the energy of an event if it is ER or NR. In other words, to produce a given S1, the recoil energy (keV$_{nr}$) required for a nuclear recoil is greater than for an electronic recoil (keV$_{ee}$).

The accurate conversion into S1 and S2 signals takes into account the fluctuations about the number of quanta (photons and electrons) produced and on the detection efficiency. The result of the S1 conversion for ER and NR events is shown in figures 5.18 and 5.19, respectively. They are expressed in the keV$_{ee}$ (keV$_{nr}$) energy scale for electronic (nuclear) recoils and the fluctuations over the median value are also reported.

S2 signal

The S2 signal is originated by the detection of the ionization produced, thus one needs to describe the detection efficiency of electrons, having established the charge yield. First of all, one must consider the probability for an e^- to not recombine during the drift path towards the anode. This is said *survival probability* and is given by

$$\frac{N_{e^-}^{anode}(t)}{N_{e^-}^{tot}} = e^{-t/\tau} \,, \tag{5.13}$$

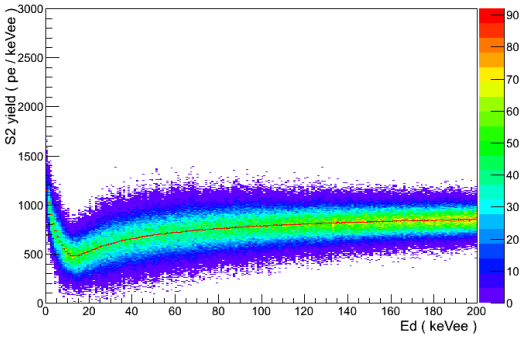

Figure 5.20: S2-yield as function of the energy for **electronic recoils**.

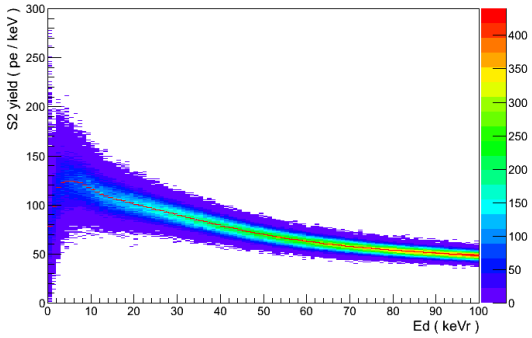

Figure 5.21: S2-yield as function of the energy for **nuclear recoils**.

where τ is the electron lifetime, which in the purification regime can be taken as infinite[3], and t is the drift time which vary with the event position.

When the electrons enter the gaseous xenon gap, they have enough energy to start avalanche ionization with the production of a certain number of photons which are finally detected by PMTs. Taking into account the quantum and collection efficiency of PMTs, the signal produced by a single electron has been estimated to be 20 ± 7 pe [116]. Thus, the median *S2-yield* as function of the deposited energy is

$$S2_Y(E) = Q_{Y,er(nr)} \cdot 20\,\mathrm{pe}/e^- \,. \tag{5.14}$$

The resulting plots for electronic and nuclear recoils are reported in figures 5.20 and 5.21.

[3]The electron lifetime depends on the level of purification of LXe. In the XENON100 experiment, it has been measured that after few purification cycles τ becomes larger than twice the drift time. Therefore, it can be considered as infinite, allowing a 100% survival probability.

Chapter 6

XENON1T sensitivity

In this final chapter we present the study of the complete, bi-dimensional statistical model of the XENON1T experiment. It can be considered an extension of the uni-dimensional case developed in chapter 4. The model is characterized by two observables: the recoil energy expressed in terms of collected photoelectrons (S1 signal) and the discrimination parameter Y, an idealized version of the observable $\log_{10}(S2/S1)$ discussed in section 2.1.3. The study of the experimental sensitivity is carried out by using both the Likelihood Ratio method (section 6.2) and the Profile Likelihood approach (section 6.3), where we introduce a nuisance parameter to take into account also systematic uncertainties.

6.1 The XENON1T statistical model

To study the XENON1T sensitivity, we build a bi-dimensional statistical model with the two observables S1 and Y. The model is composed by the signal, due to WIMP-nucleon interactions, and the ER and NR backgrounds, originated by known particles producing a single electronic or nuclear recoil inside the fiducial volume. In this chapter we define the probability distributions of each component in terms of the two observables considered.

In sections 5.1 and 5.2 we described the energy spectra of signal and backgrounds. The S1 distributions are then obtained thanks to the conversion described in section 5.3.

6.1.1 S1 distributions

In figure 6.1 we show a summary of converted spectra of ER and NR backgrounds along with three expected signal distribution of three reference WIMP masses. These latter are reported for assumed cross section values near the sensitivity limits found in this work (section 6.3). It also should be noted that in figure 6.1 we report, for convenience, the S1 spectra obtained after a discrimination cut of 99.75% of ER events, which leaves a 40% NR acceptance. However,

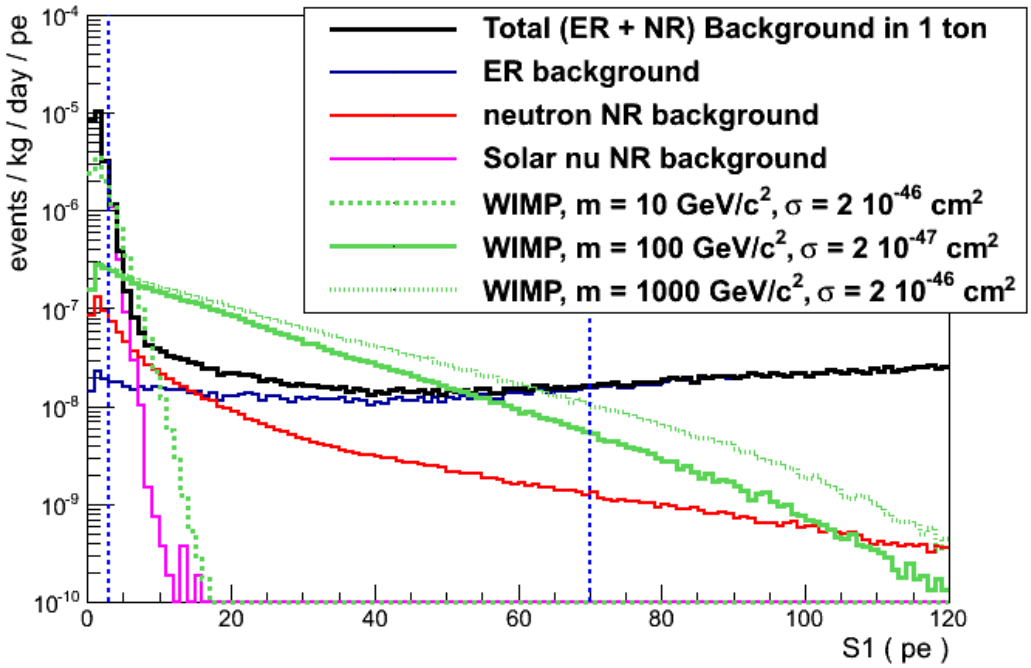

Figure 6.1: S1 distributions (after 99.75% discrimination) of ER background (blue), neutrons (red) and CNNS (pink) background (total ER+NR background in black) and WIMPs (green lines). The vertical dashed lines delimit the [3, 70] pe range.

in our study we do not apply any discrimination on simulated data. The other assumptions considered to calculate the S1 spectra of figure 6.1 are the following:

- 7.7 pe/keV Light Yield for a 122 keV γ at zero electric field, which correspond to 4.6 pe/keV at 500 V/cm field;
- $\mathcal{L}_{eff}$ extrapolated down to 1 keV;
- S2 amplification of 19.7 ± 7 pe/e$^-$;
- infinite electron lifetime;
- S2>150 pe;
- 1 tonne fiducial volume.

The expectation values of number of observed events are simply calculated from the integral of these spectra, in the S1 ROI, multiplied by the desired exposure (experiment running time $\times$ target mass). We will indicate such expectation values as μ_s, μ_{bER}, μ_{bNR} for signal, ER and NR background respectively. From here on, we fix a reference exposure of 2 tonne·years. Table 6.1 shows the expectation values of signal and background we will use and, just for comparison, the expected number of events after a 99.75% discrimination cut.

Expectation values of observed events in 2 tonne·years exposure		
	No discrimination	99.75% ER discrimination
Signal		
10 GeV/c^2 WIMP ($\sigma = 2 \times 10^{-46}$ cm^2)	4.63	1.85
100 GeV/c^2 WIMP ($\sigma = 2 \times 10^{-47}$ cm^2)	7.13	2.85
1 TeV/c^2 WIMP ($\sigma = 2 \times 10^{-46}$ cm^2)	8.85	3.54
Background		
Total ER (μ_{bER})	258	0.65
neutrons	1.10	0.44
CNNS	2.77	1.11
Total NR (μ_{bNR})	3.87	1.55
Total ER+NR	259.3	2.19

Table 6.1: Number of expected events without and with 99.75% ER discrimination from S1 spectra (figure 6.1) in the range [3, 70] pe.

6.1.2 Y distributions

The second observable characterizing our statistical model is the discrimination parameter Y. It is an idealized version of the real variable $\log_{10}(S2/S1)$ used as discrimination parameter within the XENON collaboration experiments. As a matter of fact, the distributions of electromagnetic and nuclear recoils are pretty well separated in that variable. This allows to discriminate ER from NR events and therefore to remarkably cut down the ER background which would stand far above the signal and NR background. However, rather than applying any discrimination cut to reduce ER events, we maintain all the information from data samples and we build the model adding the observable Y, which will allow us to correctly analyze ER and NR events without any a priori cut.

Indeed, the Y p.d.f.s of ER and NR are defined such as:

- ER events: gaussian distribution with mean 0 and variance 1;
- NR events: gaussian distribution with mean -2.58 and standard deviation 0.92.

With such choice, we can reproduce the XENON100 performances:

- 99.5% ER discrimination, with 50% NR acceptance;
- 99.75% ER discrimination, with 40% NR acceptance.

The difference with the real discrimination parameter $\log_{10}(S2/S1)$ stands in the correlation with S1: in our simplified model they are totally uncorrelated, while in the real case they show the behavior seen in figure 2.3.

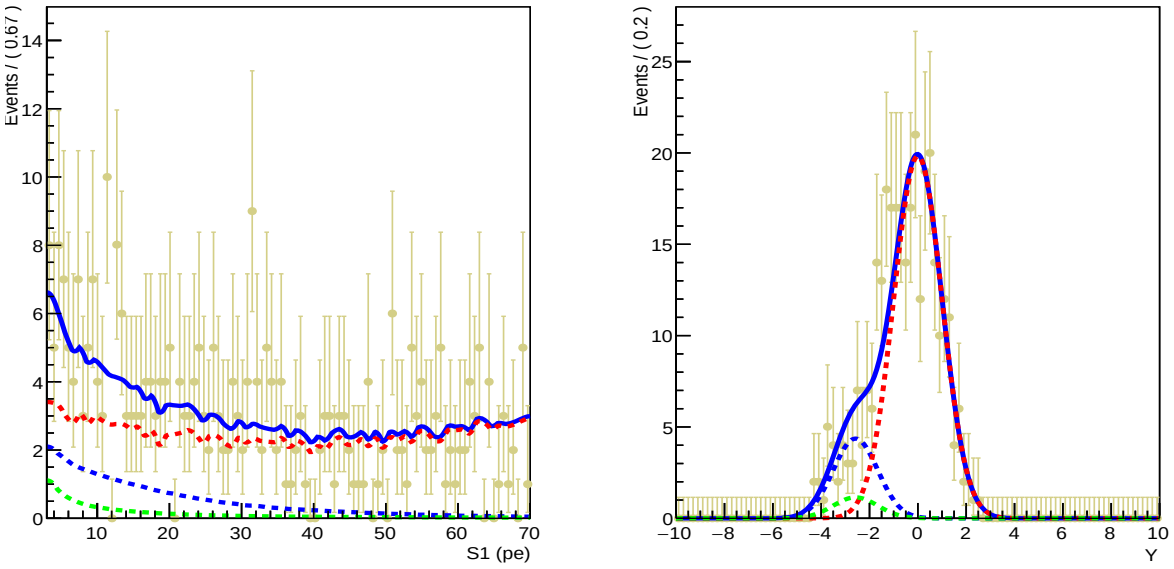

Figure 6.2: Projections into S1 (left) and Y (right) spaces. Points of the data sample generated (yellow) with the fit of each component drawn as dashed lines: signal (blue), ER background (red), NR background (green). The blue solid line accounts for the total model.

The resulting model is then bi-dimensional, composed by the two observables S1 and Y, for which we implement three components: signal, ER and NR background. Having assumed S1 and Y to be uncorrelated, the overall model is simply given by the sum of each component.

An example of a simulated data sample, with an enhanced signal ($\mu_s = 50$) from a 100 GeV/c^2 WIMP, is reported in figure 6.2, where the S1 and Y projections are shown. The S1-Y scatter plot is given in figure 6.3, where signal and NR events are respectively highlighted with red circles and blue squares.

6.2 Likelihood Ratio method

We first study the XENON1T statistical model with the simplified approach of the Likelihood Ratio method [117], where systematical uncertainties are not taken into account. Thus, no nuisance parameters are introduced and this considerably simplifies the method with respect to the Profile Likelihood case in which, instead, systematic uncertainties are involved (section 6.3).

In the previous chapter, we established signal and background spectra both in the observables S1 and Y. It is helpful to assess the terminology that will be used from here on. We call f_s, f_{bER}, f_{bNR} the probability density functions of signal, ER and NR background respectively, where f_s is intended to vary with different WIMP masses. These functions specify the *shape* of each recoil energy spectrum. To fully characterize the model, the *normalization* of such distributions is also needed, that is the expected number of events of each component, which

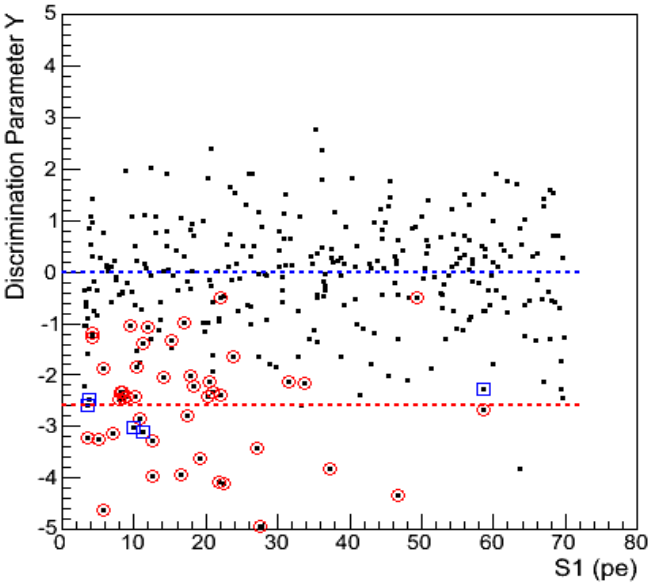

Figure 6.3: Example of a data set generated with μ_{bER} and μ_{bNR} from table 6.1 and $\mu_s = 50$ for a WIMP of mass 100 GeV/c^2. The points circled in red are signal events, those with blue squares are NR background events and the others are ER events.

are named μ_s, μ_{bER} and μ_{bNR}. Having defined the shape of S1 spectra, the number of expected events is set after the chosen exposure.

Expectation values are related only to the S1 parameter space, while the p.d.f.s in the Y space solely describe the different pattern of electronic and nuclear recoil with regard to the (idealized) discrimination parameter. We indicate the two Y gaussian distributions as g_{ER} and g_{NR}.

We perform the study through the *unbinned* and *extended* likelihood analysis, meaning that the data are sampled from the functions f and g and, thus, each event is identified by a point in the unbinned (S1,Y) bi-dimensional space. The expectation value of the total number of events in a data set N_{obs}, given the model and the exposure, corresponds to the sum of each contribution:

$$\mu_{tot} = \mu_s + \mu_{bER} + \mu_{bNR} \,. \tag{6.1}$$

The extended likelihood function (4.1), for this model, is

$$L(\mu_s) = \frac{\mu_{tot}^{N_{obs}}}{N_{obs}!}\, e^{-\mu_{tot}} \prod_{i=1}^{N_{obs}} P(S1_i, Y_i) = \frac{e^{-\mu_{tot}}}{N_{obs}!} \prod_{i=1}^{N_{obs}} \mu_{tot}\, P(S1_i, Y_i) \,, \tag{6.2}$$

where $S1_i$ and Y_i are the values of the two observables for the i-th event and $P(S1_i, Y_i)$ express the probability to measure such point. The probability of each event can be written, in terms of its components, as

$$\begin{aligned} P(S1_i, Y_i) = \frac{1}{\mu_{tot}} \big[& \mu_s\, f_s(S1_i)\, g_{NR}(Y_i) + \mu_{bER}\, f_{bER}(S1_i)\, g_{ER}(Y_i) \\ & + \mu_{bNR}\, f_{bNR}(S1_i)\, g_{NR}(Y_i) \big] \,. \end{aligned} \tag{6.3}$$

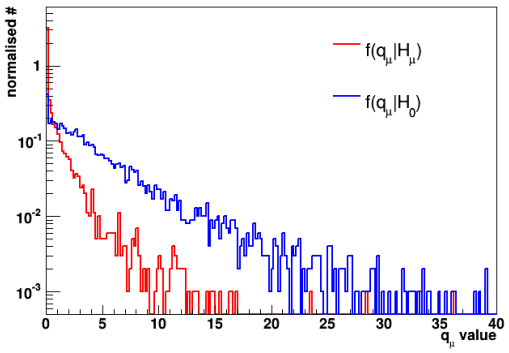

(a) Test statistic distributions $f(q_\mu|H_\mu)$ and $f(q_\mu|H_0)$ for the signal hypothesis $\mu_s = 5$.

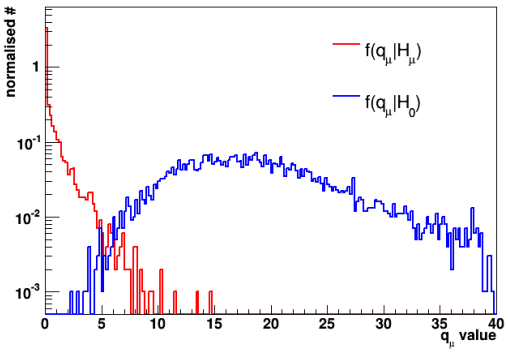

(b) Test statistic distributions $f(q_\mu|H_\mu)$ and $f(q_\mu|H_0)$ for the signal hypothesis $\mu_s = 20$.

Figure 6.4: Probability distributions of the test statistic q_μ under signal and background-only hypothesis for different μ_s tested.

Finally, considering the log-likelihood, we have

$$\begin{aligned} -2\ln L(\mu_s) &= 2\,\mu_{tot} - 2\sum_{i=1}^{N_{obs}} \ln\big[\mu_{tot}\,P(S1_i, Y_i)\big] \\ &= 2\,(\mu_s + \mu_{bER} + \mu_{bNR}) - 2\sum_{i=1}^{N_{obs}} \big[\mu_s\,f_s(S1_i)\,g_{NR}(Y_i) \\ &\quad + \mu_{bER}\,f_{bER}(S1_i)\,g_{ER}(Y_i) + \mu_{bNR}\,f_{bNR}(S1_i)\,g_{NR}(Y_i)\big]\,. \end{aligned} \tag{6.4}$$

In the model all of the parameters are fixed but the expected number of signal events μ_s, which is our *parameter of interest*.

We perform the analysis using the exclusion **test statistic** q_μ (3.11), without dependence on any nuisance parameter:

$$q_\mu = \begin{cases} -2\ln\frac{L(\mu_s)}{L(\hat{\mu}_s)} & \text{if } \hat{\mu}_s \leq \mu_s \\ 0 & \text{if } \hat{\mu}_s > \mu_s\,. \end{cases} \tag{6.5}$$

where μ_s specifies the signal hypothesis under test, while $\hat{\mu}_s$ is its MLE.

The distributions $f(q_\mu|H_\mu)$ and $f(q_\mu|H_0)$ of the test statistic under different hypotheses are produced following the procedure already discussed in section 4.3. Figure 6.4 shows two examples of the p.d.f.s obtained for a small and a large μ_s. For small μ_s, $f(q_\mu|H_0)$ approaches $f(q_\mu|H_\mu)$, while under stronger signal hypotheses $f(q_\mu|H_0)$ spreads toward larger values, indicating higher incompatibility.

6.2.1 Sensitivity results

We produced the test statistic p.d.f.s $f(q_\mu|H_\mu)$ and $f(q_\mu|H_0)$ for μ_s values, from 0 to 20, by generating 5000 independent toy experiments under each one of such hypotheses H_μ and H_0.

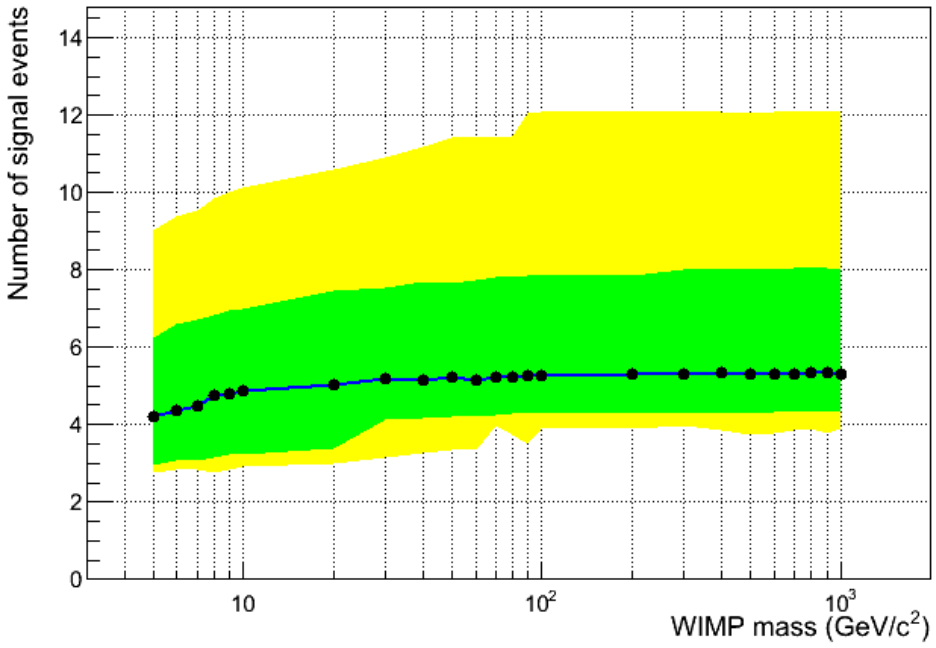

Figure 6.5: XENON1T sensitivity at 90% CL in terms of number of events in the exposure of 2 tonne·years, obtained with the Likelihood Ratio approach and using the CL_s method.

We scanned a wide range of WIMP masses, namely between 5 GeV/c^2 and 1 TeV/c^2, and we therefore repeated the estimation of $f(q_\mu|H_\mu)$ and $f(q_\mu|H_0)$ for each studied mass.

We perform the experimental sensitivity evaluation fixing the 90% confidence level and applying the CL_s correction (see section 3.2.1). The limit calculation follows the procedure already described in section 4.3. The full XENON1T sensitivity curve is achieved by finding the exclusion limits for the different WIMP masses studied.

Figure 6.5 shows the results of the scan of WIMP masses in the range [5, 1000] GeV/c^2 performed with the Likelihood Ratio method. It represents the sensitivity curve in terms of number of signal events at 90% confidence level calculated using the CL_s method. The sensitivity is between 4 and 6 events and slightly increases with the WIMP mass.

The final step consists in translating the number of signal events into WIMP-nucleon cross section values. The conversion is achieved recalling the relationship between the WIMP interaction rate and the cross section σ (equations 5.3 and 5.6). Having set the exposure to 2 tonne·years in the LXe target and having established the energy ROI, the sensitivity to σ is easily derived (figure 6.6). The red dashed curve in the figure represents the sensitivity evaluated in [99] using the Maximum Gap method [118], which is a different frequentist approach to set exclusion limits. Such curve comes from the same assumptions made in this work, with the only difference that the 99.75% ER discrimination is applied to simulated data before analyzing them. The Maximum Gap method do not allow to take into account systematic uncertainties

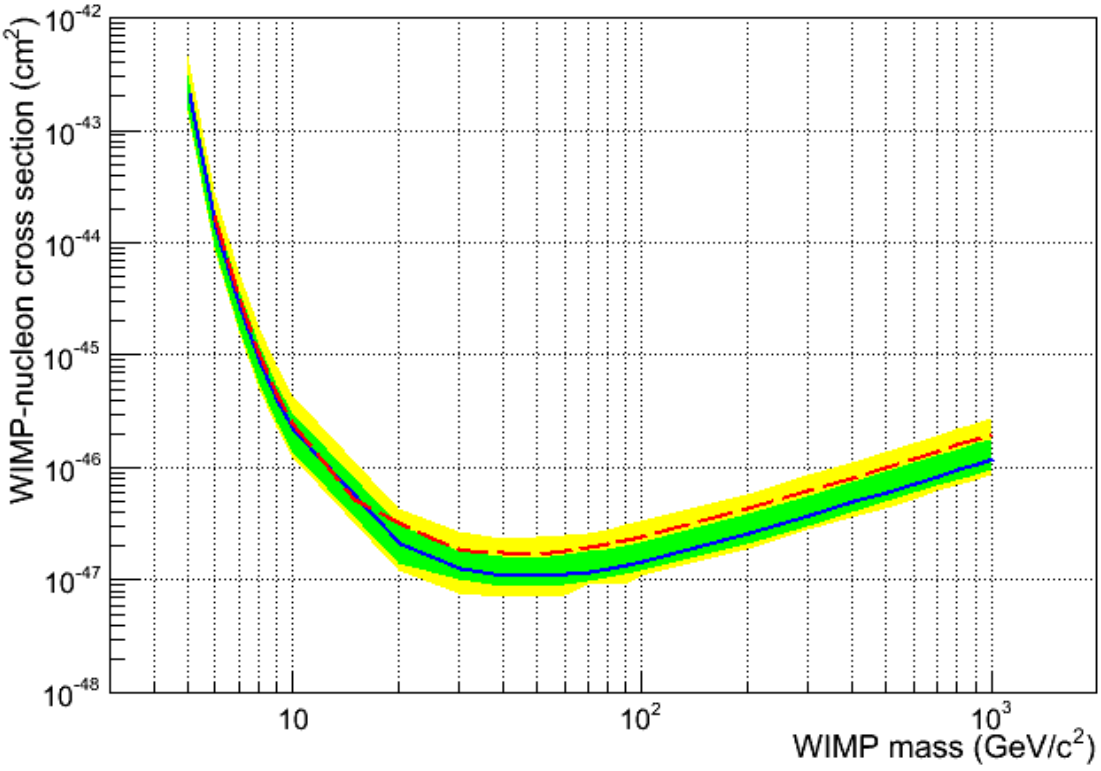

Figure 6.6: XENON1T sensitivity at 90% CL in terms of WIMP-nucleon cross section in the exposure of 2 tonne·years, obtained with the Likelihood Ratio approach and using the CL_s method. The red dashed curve is the sensitivity computed using the Maximum Gap method [99].

and it is therefore suitable to be compared with the outcome of the Likelihood Ratio approach. The median upper limits at 90% confidence level from these two methods converge at low WIMP masses, while above about 50 GeV/c^2 the LR approach is able to set stronger limits by a stable factor $\simeq 1.7$.

It is interesting to remark that, even though at low WIMP masses the limits μ_{90}^{up} are pretty small, the sensitivity in terms of cross section is strongly constrained to large values. Since WIMPs of low mass are expected to produce few nuclear recoils, of low energy only, a relatively small number of events corresponds to a rather high cross section. This explains why direct DM experiments are less sensitive to light WIMPs.

The minimum of the median sensitivity is found at 1.1×10^{-47} cm^2 for a WIMP mass of 40 GeV/c^2.

6.3 Profile Likelihood method

The simple Likelihood Ratio method can be extended to incorporate *systematic uncertainties* in the statistical data analysis. By far the main source of uncertainty for the XENON1T exper-

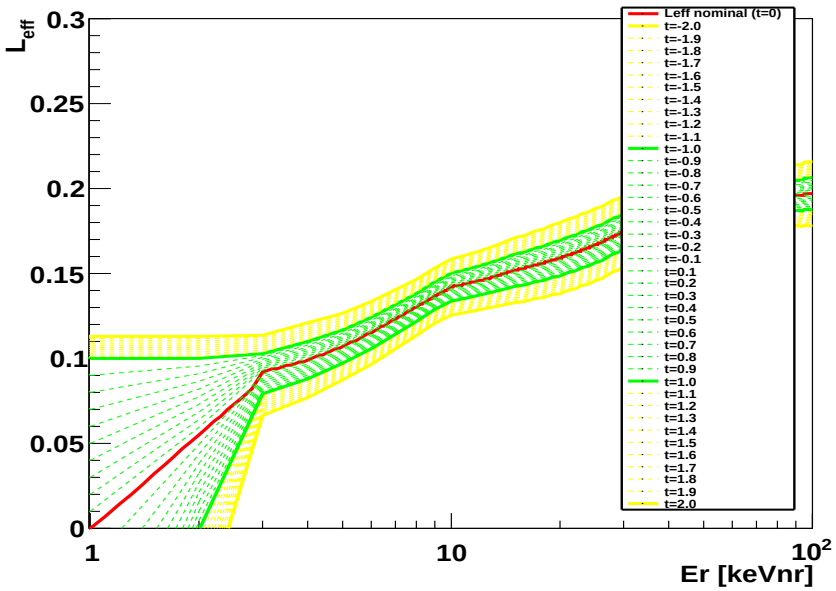

Figure 6.7: Parametrized $\mathcal{L}_{eff}$ curves as function of the nuisance parameter t up to the 2σ band.

iment is related to the relative scintillation efficiency $\mathcal{L}_{eff}$ (see section 5.3.2), which affects both WIMP signal and NR background. For this reason, it is important to perform the sensitivity calculation taking into account our not perfect knowledge of the $\mathcal{L}_{eff}$ curve, especially at very low energy. Indeed, no experimental points have ever been set below 3 keV (as can be deduced from figure 5.17).

To parametrize the uncertainty on $\mathcal{L}_{eff}$ is thus a mandatory requirement to properly set up the analysis based on the **profile likelihood** [119], which in turn provides the more natural method to handle systematics. In the LR evaluation of sensitivity we fixed $\mathcal{L}_{eff}$ to its median curve and we used those values to convert recoil energy spectra of WIMPs and NR background into S1 distributions, ultimately assuming a one to one mapping. In the following, we will assess, instead, the impact of the uncertainty on such conversion when defining the XENON1T statistical model and, in conclusion, how this affects the sensitivity.

6.3.1 Parametrization of $\mathcal{L}_{eff}$ uncertainty

In this context, our reference $\mathcal{L}_{eff}$ description, that is its median and its 1σ and 2σ error bands, is the one drawn in figure 5.17. Thus, for energy lower than 3 keV we assume an extrapolation down to 1 keV, below which $\mathcal{L}_{eff}$ is set to 0. In this range, the error bands spread quite a lot as a consequence of lack of knowledge.

We introduce a variable t with the aim of describing the displacement from the nominal $\mathcal{L}_{eff}$ curve, that we will indicate as $\mathcal{L}_{eff}$(median). The distribution of t is defined as a gaussian with mean 0 and unit variance, so as the value of t maps the number of standard deviations of fluctuations from $\mathcal{L}_{eff}$(median). Such variable represents the *nuisance parameter* to be put into

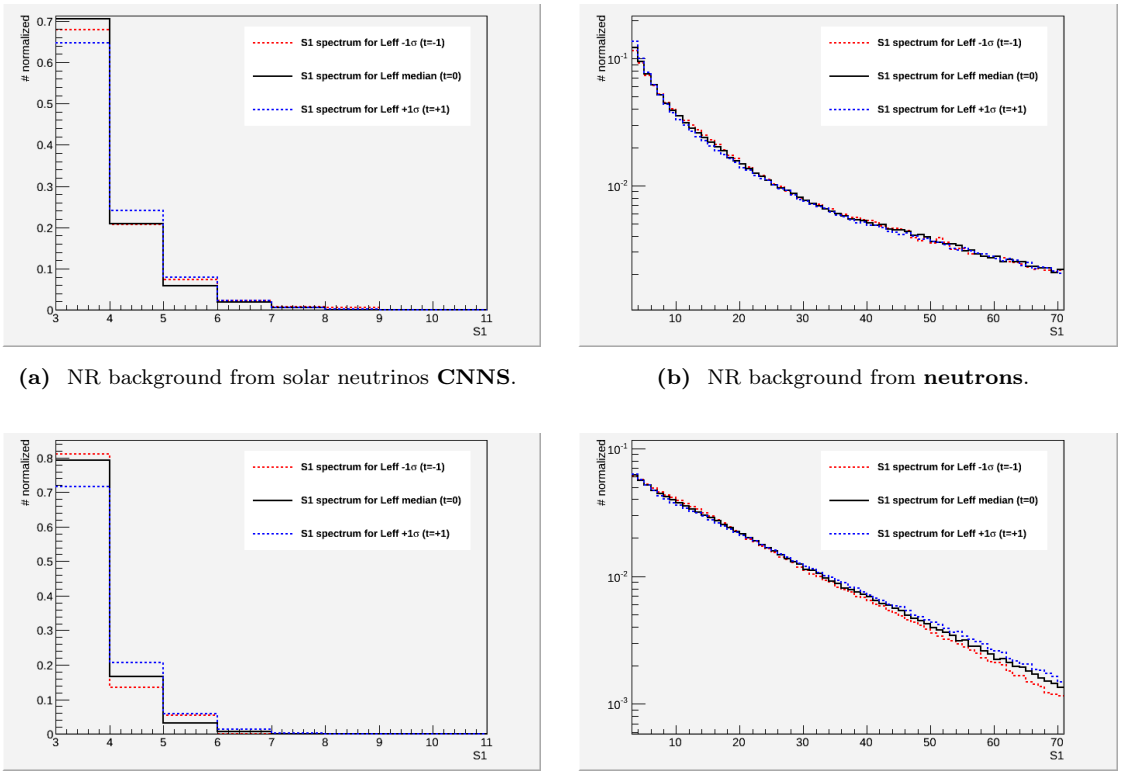

(a) NR background from solar neutrinos **CNNS**.

(b) NR background from **neutrons**.

(c) Signal from WIMPs of mass $m_\chi = 5$ GeV/c^2.

(d) Signal from WIMPs of mass $m_\chi = 100$ GeV/c^2.

Figure 6.8: Variation of S1 spectral shapes under different $\mathcal{L}_{eff}$ assumed in the conversion from energy to S1 signal: black solid for $\mathcal{L}_{eff}$(median) and dashed lines for $\mathcal{L}_{eff}(+1\sigma)$ (red) and $\mathcal{L}_{eff}(-1\sigma)$ (blue).

the PL analysis. For each t we select a different curve as $\mathcal{L}_{eff}$, accordingly shifted with respect to the median. If we call $\Delta\mathcal{L}_{eff}(\pm1\sigma)$ the point by point distance between $\mathcal{L}_{eff}$(median) and its $\pm1\sigma$ boundary curves, we can summarize our parametrization as

$$\mathcal{L}_{eff} = \begin{cases} \mathcal{L}_{eff}(\text{median}) + t \cdot \Delta\mathcal{L}_{eff}(+1\sigma) & \text{if } t \geq 0 \\ \mathcal{L}_{eff}(\text{median}) + t \cdot \Delta\mathcal{L}_{eff}(-1\sigma) & \text{if } t \leq 0 \end{cases}, \tag{6.6}$$

whose graphical view is displayed in figure 6.7. Below 3 keV the upper 2σ band is taken narrower than the lower one (see figure 5.17). Thus, to do a proper parametrization one needs to consider the distance $\mathcal{L}_{eff}(+2\sigma) - \mathcal{L}_{eff}(+1\sigma)$ rather than $\Delta\mathcal{L}_{eff}(+1\sigma)$ below 3 keV when $t > 1$.

Effects on S1 p.d.f.s

3

A variation of the $\mathcal{L}_{eff}$ curve affects and modifies both the S1 spectral shapes (f_s and f_{bNR}) and their normalization, thus implying also a fluctuation of expectation values μ_s and μ_{bNR}.

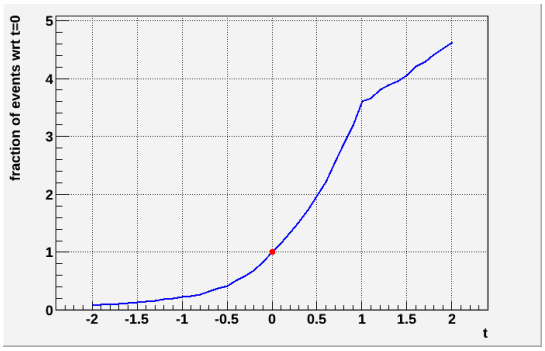

(a) NR background from solar neutrinos **CNNS**.

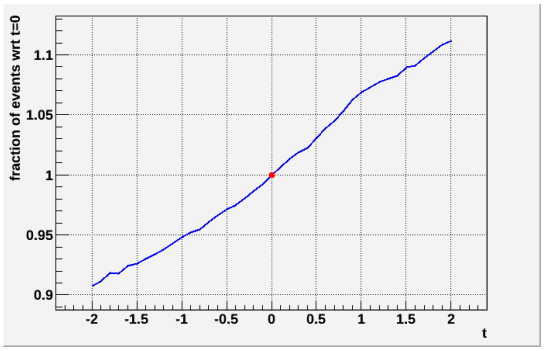

(b) NR background from **neutrons**.

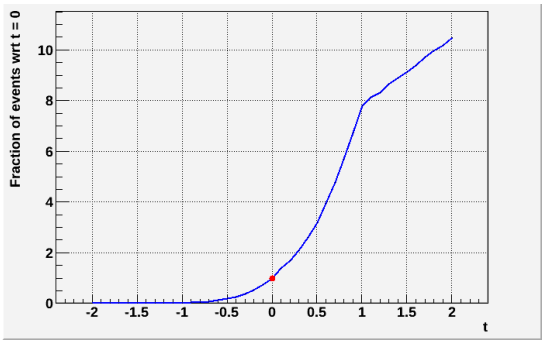

(c) Signal from WIMPs of mass $m_\chi = 5$ GeV/c^2.

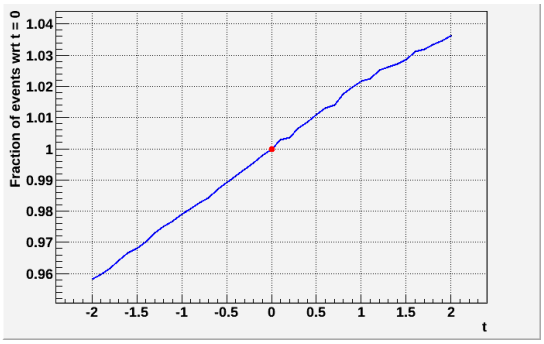

(d) Signal from WIMPs of mass $m_\chi = 100$ GeV/c^2.

Figure 6.9: Variation of expected number of events under different $\mathcal{L}_{eff}$ assumed in the conversion from energy to S1 signal. The curves represent the ratio of the number of events corresponding to different values of t compared with the one coming from the conversion with the nominal $\mathcal{L}_{eff}$(median).

Figure 6.8 shows the impact of $\pm 1\sigma$ displacements from the nominal $\mathcal{L}_{eff}$ on the shapes of S1 spectra (normalized) of NR background components (neutrons and CNNS) and WIMPs of low as well as high mass. It can be easily seen that such p.d.f.s are only slightly modified under $\mathcal{L}_{eff}$ variations. The effect is barely more evident for the neutrinos NR background and low mass WIMPs, but still rather weak. This allows to make the following assumption, which greatly reduces the amount of computational effort requested: the *shapes* of S1 spectra are kept fixed to those derived using the nominal $\mathcal{L}_{eff}$ curve even when $t \neq 0$.

Effects on the expectation values of the number of events

When we consider values of $\mathcal{L}_{eff}$ different from the median, what significantly changes in the model is the number of expected events in the [3, 70] pe window we want to study. With higher scintillation efficiency, for a given (nuclear) recoil energy, the number of photoelectrons detected increases. This means that events of low energy that gave rise to a S1 response just below the 3 pe threshold, can flow into our ROI for even better $\mathcal{L}_{eff}$. Similarly, the last part of S1 spectra

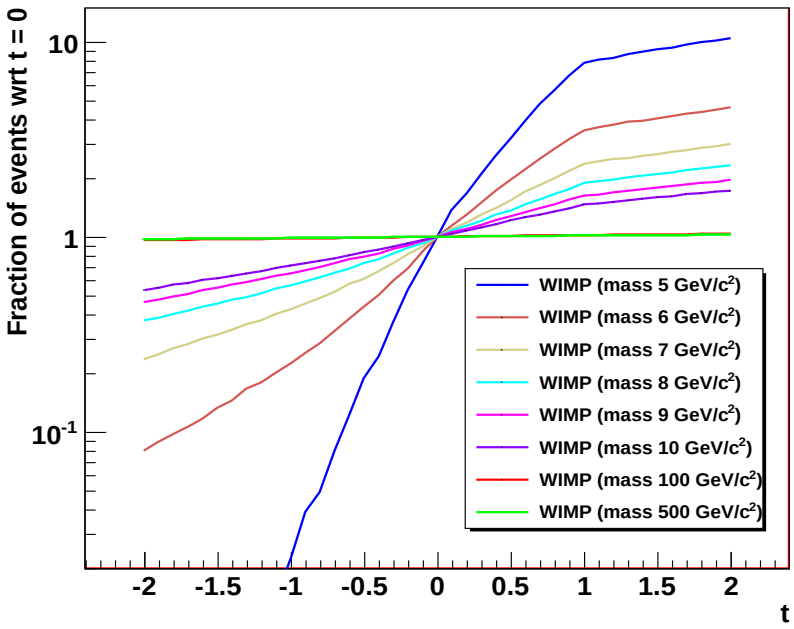

Figure 6.10: Ratio of the expected number of signal events μ_s as function of t with respect to its value for $t = 0$. The curves for different WIMP masses from 5 to 500 GeV/c^2 are plotted.

would be shifted to higher number of pe, causing some events to get out the ROI. The balance between inbound and outbound events in the [3, 70] pe window depends on the energy spectra shape. These latter drop down with recoil energy (as showed in figures 5.8 and 5.12), hence we expect the number of events to grow for increasing $\mathcal{L}_{eff}$ and vice versa.

Quantitative evaluations on number of expected events variation under different values of the nuisance parameter t are reported in figure 6.9. There is shown the fraction of events with respect to the number expected with $\mathcal{L}_{eff}$(median) for NR background and two reference WIMPs. In figure 6.10 the same plot is proposed for several WIMPs, from low to high masses.

It is clear that fluctuations of t have a huge impact on the neutrino background and on the signal from very low WIMP masses, since the main contribution to their S1 spectra comes uniquely from the lowest energy part (see figures 5.8 and 5.12), where such uncertainty becomes remarkably larger (figure 5.17). Conversely, 2σ fluctuations produce variations at most of the order of 10% for the NR backgrounds due to neutron interactions, while the impact on high WIMP masses becomes even negligible.

6.3.2 Definition of the test statistic

In the presence of a nuisance parameter, the likelihood function (unbinned and extended) must contain an additional term expressing the probability to observe a given value of such parameter and it is now referred as $L(\mu_s, t)$, in order to underline the dependence on the nuisance parameter. As t is normally distributed, its probability is described by $exp(-t^2/2)$ and, omitting

constant additive terms, the log-likelihood becomes:

$$-2\ln L(\mu_s,t) = 2\left[\mu_s(t)+\mu_{bER}+\mu_{bNR}(t)\right] - 2\sum_{i=1}^{N_{obs}}\Big[\mu_s(t)\,f_s(S1_i)\,g_{NR}(Y_i) + \mu_{bER}\,f_{bER}(S1_i)\,g_{ER}(Y_i) + \mu_{bNR}(t)\,f_{bNR}(S1_i)\,g_{NR}(Y_i)\Big] + t^2\,. \tag{6.7}$$

The parameter of interest in the likelihood is again the signal strength μ_s. Besides the gaussian term of t, the difference with respect to the LR case lies in the dependence from t of the expectation values μ_s and μ_{bNR}, while the p.d.f.s f remain fixed as previously stated.

The test statistic to be considered is here the profile likelihood ratio defined in 3.8, that is

$$-2\ln\frac{L(\mu_s,\hat{\hat{t}})}{L(\hat{\mu}_s,\hat{t})} \;=\; -2\ln L(\mu_s,\hat{\hat{t}}) \;+2\ln L(\hat{\mu}_s,\hat{t})\,, \tag{6.8}$$

to which we impose the analogous condition of (6.5), since we aim at the sensitivity evaluation:

$$q_\mu = \begin{cases} -2\ln\frac{L(\mu_s,\hat{\hat{t}})}{L(\hat{\mu}_s,\hat{t})} & \text{if } \hat{\mu}_s \le \hat{\mu}_s \\ 0 & \text{if } \hat{\mu}_s > \hat{\mu}_s \end{cases} \tag{6.9}$$

The numerator $L(\mu_s,\hat{\hat{t}})$ is the *conditional* maximized likelihood, which is obtained by *profiling out* the nuisance parameter. Given a fixed value of μ_s to test, $\hat{\hat{t}}$ is the value of t which maximizes L. Instead, $L(\hat{\mu}_s,\hat{t})$ is the *unconditional* maximized likelihood, for which both the maximum likelihood estimators (MLE) of μ_s and t are taken into account.

At this point, the procedure to compute the sensitivity reflects the one already carried out within the Likelihood Ratio method. The distributions $f(q_\mu|H_\mu)$ and $f(q_\mu|H_0)$ are constructed by generating many toy experiments, then the exclusion limits are calculated following the precepts exposed in section 4.3. However, it is worth pointing out that, in the PL case, when one simulates a data set, the nuisance parameter t must be sampled according to its p.d.f. and the expectation values $\mu_s(t)$ and $\mu_{bNR}(t)$ are redefined accordingly to the extracted t. Then one proceed with the poissonian sampling of the number of events of signal and NR background.

6.3.3 Sensitivity results

The XENON1T experimental sensitivity with the PL method has been estimated through the generation of 10000 toy experiments to build the distributions $f(q_\mu|H_\mu)$ and $f(q_\mu|H_0)$. The scan has been extended up to μ_s=50 as signal hypothesis tested and to m_χ=10 TeV/c^2 for the WIMP mass range.

In this section, we present the sensitivity result obtained using the CL$_s$ method, the $\mathcal{L}_{eff}$ model (6.6) and the test statistic (6.9). However, we will also outline how such results would vary not applying the CL$_s$ protection or under different assumptions on the parametrization of the $\mathcal{L}_{eff}$ uncertainty and on the test statistic used.

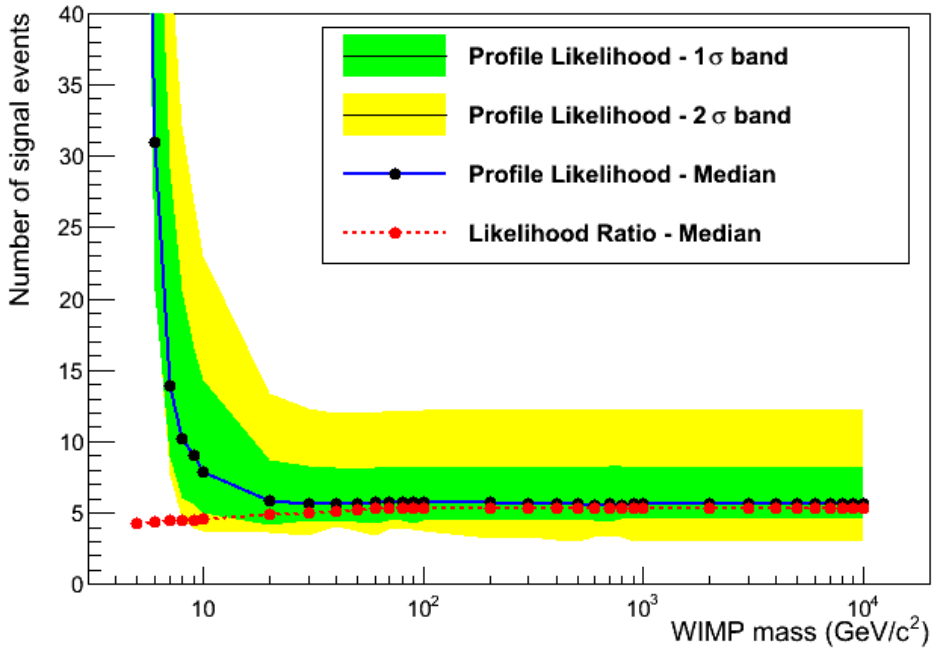

Figure 6.11: XENON1T sensitivity at 90% CL in terms of number of events in the exposure of 2 tonne·years, obtained with the Profile Likelihood approach using the CL_s method (blue curve for the median and filled areas for the error bands). The result (median) of the Likelihood Ratio method is superimposed in the red dashed curve.

The sensitivity plot of figure 6.11 shows the upper limits, in terms of number of signal events observed in 2 tonne·years exposure, at 90% confidence level with the CLs method. The red dashed lines allows the comparison with the results of the LR scan.

As one would expect, the PL upper limits are weaker than the LR ones, since systematic uncertainties are here taken into account, while they are not provided in the simple LR method. At higher WIMP masses the two curves approach themselves, while for masses below 20 GeV/c^2 the difference becomes remarkable. Indeed, the uncertainty on $\mathcal{L}_{eff}$ plays an important role especially at low masses because the corresponding WIMP spectra suddenly fall to zero and are therefore more sensitive to $\mathcal{L}_{eff}$ fluctuations (see figure 6.10).

The sensitivity as WIMP-nucleon cross section exclusion limits is achieved by converting μ_s into σ, given the studied S1 range and the 2 tonne·years exposure. In figure 6.12 the red curve shows the corresponding result from the LR approach. Again, the two method produce very similar results for high WIMP masses, while systematics have much more influence on setting limits for light WIMPs. Above m_χ=20 GeV/c^2 the ratio between PL and LR limits (figure 6.13) is always less than 1.2 and for higher masses the difference between PL and LR stands just below the 5%. At lower masses, instead, the systematic uncertainty on $\mathcal{L}_{eff}$ produce much higher limits in the PL study, up to more than 10 times larger below 6 GeV/c^2.

In conclusion, we can state that the rejection power of nuclear cross section σ for very light

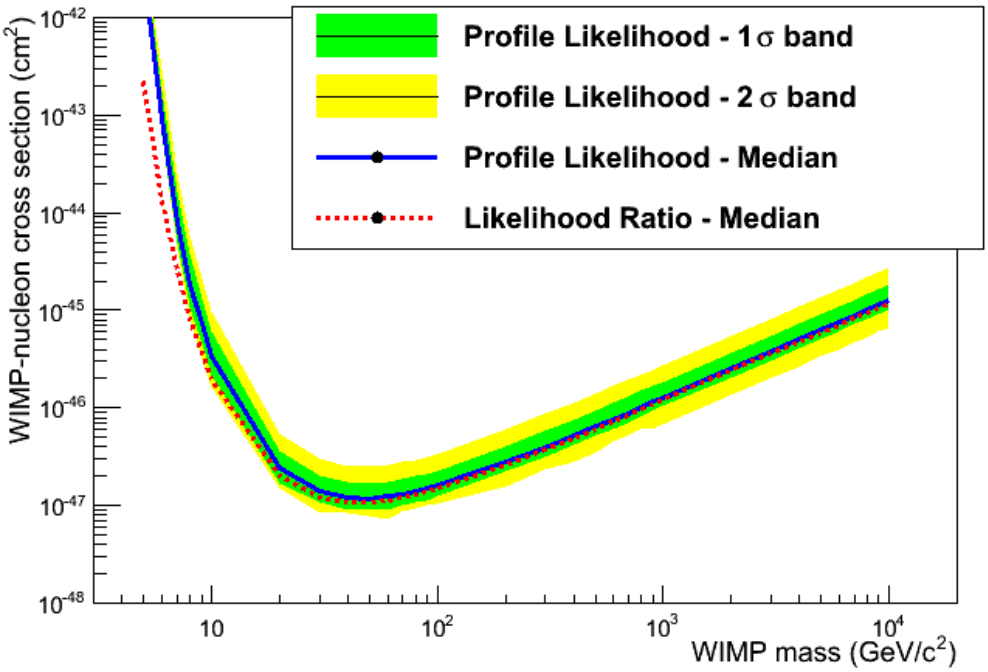

Figure 6.12: XENON1T sensitivity at 90% CL in terms of WIMP-nucleon cross section σ in the exposure of 2 tonne·years, obtained with the Profile Likelihood approach using the CL_s method. The Likelihood Ratio result in the red dashed curve.

WIMPs becomes weaker. The maximum sensitivity is found for WIMPs of mass $m_\chi = 50$ GeV/c^2, which corresponds to a cross section σ equal to 1.2×10^{-47} cm^2. With increasing masses, the exclusion limits slightly rise to higher values.

Results with $\tilde{q}_\mu$ as test statistic

It is interesting to compare the sensitivity found using the test statistic $\tilde{q}_\mu$, instead of the usual q_μ. As can be seen from figure 6.14, the difference is negligible, hence the two test statistic produce the same upper limits for our statistical model. The usage of $\tilde{q}_\mu$ introduce some complications from the computational point of view. Since the sensitivity does not change, it is more convenient to carry out the final results by means of the test statistic q_μ.

Results without CL_s

The CL_s method is used to modify the p-value of signal hypotheses h_μ in order to avoid too low sensitivity limits, since these would come from downward fluctuations of the background rather than from outstanding detector performances. This lead to more robust and conservative limits, whose confidence level is indeed higher than the declared 90%.

If the CL_s protection is released, the sensitivity results transform into those in figure 6.15.

They give the exclusion upper limits and their 1σ and 2σ band with the proper statistical 90% coverage. The median sensitivity is better than the one obtained with CL_s as expected and the lower error bands are no longer squezeed upward, but are quite symmetric. However, having found the error bands of figure 6.15, we could say that, within 2σ fluctuations of our sensitivity, we would be able to reject every signal hypothesis down to zero. Such a statement is clearly not desiderable and it represents the main motivation to the use of the modified CL_s p-value. The effect of this protection is to squeeze the exclusion limit distribution toward higher values, the stronger the lower distribution part is.

A different parametrization of $\mathcal{L}_{eff}$ uncertainty

In the estimate of the sensitivity we assumed a "gaussian" $\mathcal{L}_{eff}$ model, i.e. gaussian error bands around the median based on the measurements in literature, with an enhancement of the uncertainty below 3 keV where no experimental points are available. However, we have complete ignorance up to 3 keV, thus every assumption on $\mathcal{L}_{eff}$ distribution in the very low energy region is arbitrary, even if reasonable. A possibility to parametrize our total lack of knowledge below 3 keV is to assume a uniform distribution for $\mathcal{L}_{eff}$, i.e. every value has the same probability of any other.

Hence we present, here, the sensitivity study under an extreme assumption about the ignorance on $\mathcal{L}_{eff}$ in order to evaluate how much the limits worsen being (too much) conservative on our degree of knowledge of the relative scintillation efficiency. We take into account the 2σ contours shown in figures 5.17 and 6.7, but we suppose a flat distribution between these contours on the whole energy scale. Operationally, we keep the parametrization formula 6.6, while we assign a flat p.d.f. to the nuisance parameter t in the interval $[-2, 2]$, rather than the normal distribution. This choice reflects the total uncertainty on $\mathcal{L}_{eff}$ that we have below 3 keV, while it is an unrealistic description of the current knowledge of $\mathcal{L}_{eff}$ above 3 keV, meaning that with this approach the uncertainty is over-estimated.

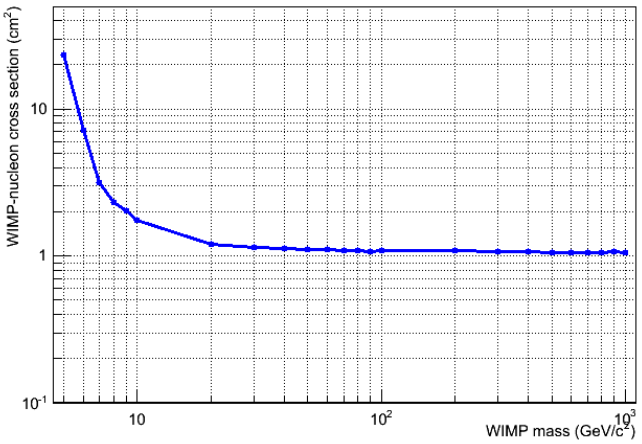

Figure 6.13: Ratio between exclusion upper limits at 90% CL obtained with the Profile and the Likelihood Ratio methods.

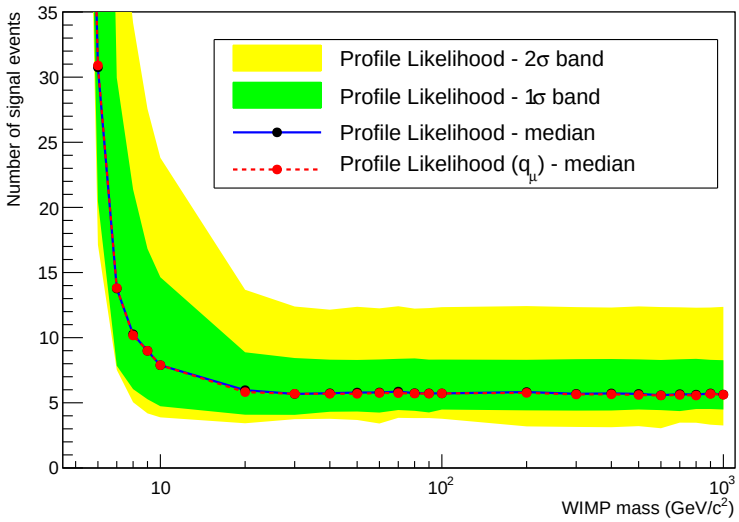

Figure 6.14: XENON1T sensitivity at 90% CL in terms of number of events in the exposure of 2 tonne·years, obtained with the Profile Likelihood approach, using the **alternative test statistic** $\tilde{q}_\mu$ and the CL$_s$ method (blue curve for the median and filled areas for the error bands). The result (median) of the computation with q_μ as test statistic is superimposed in the red dashed curve.

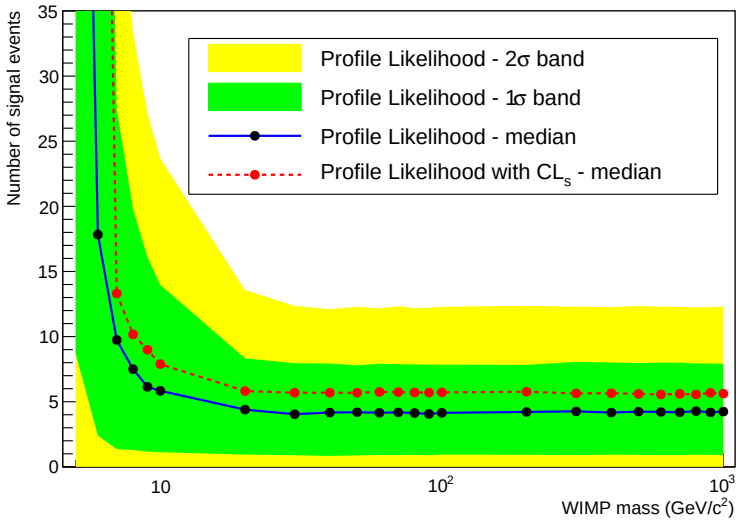

Figure 6.15: XENON1T sensitivity at 90% CL in terms of number of events in the exposure of 2 tonne·years, obtained with the Profile Likelihood approach, **not using the CL$_s$ method** (blue curve for the median and filled areas for the error bands). The result (median) of the computation with the CLs method is superimposed in the red dashed curve.

As a consequence of the change in the p.d.f. of t, the toy experiments are generated by a uniform sampling of t and the term t^2 in the log-likelihood expression (6.7) must be dropped, since the probability of t is simply a constant. The rest of the statistical procedure to get the limits remain unchanged.

The sensitivity curves obtained in the "flat" $\mathcal{L}_{eff}$ model are plotted in figures 6.16 and 6.17 along with the previous results. For WIMP masses equal or above 20 GeV/c^2 the two assumptions lead to the same upper limits, meaning that the (unrealistic) broadening of the uncertainty above 3 keV does not have a relevant impact on the median sensitivity. For $m_\chi < 20$ GeV/c^2 the results are slightly worst in the more conservative case, reflecting the increased uncertainty in $\mathcal{L}_{eff}$ and the lack of a preferred value of it.

In conclusion, the uniform parametrization of $\mathcal{L}_{eff}$ uncertainty can provide a desirable

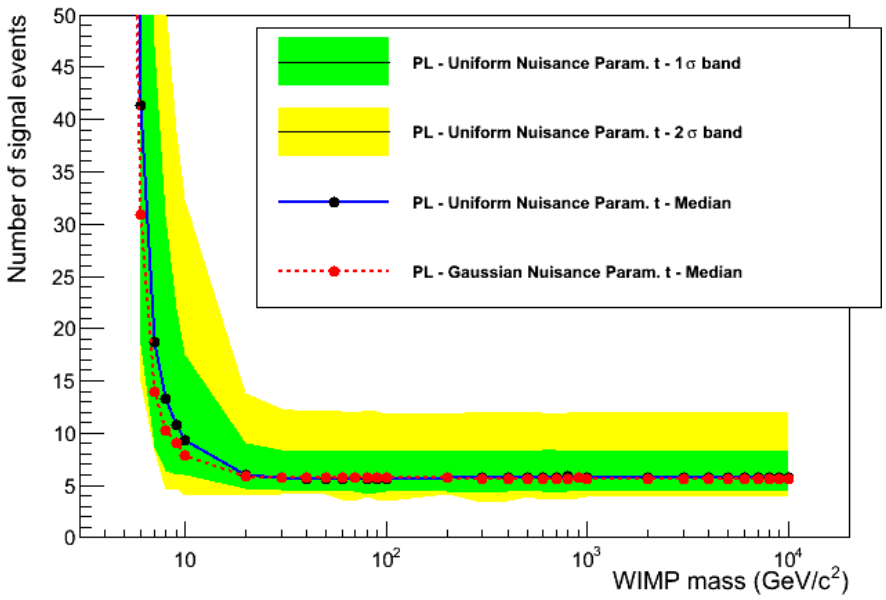

Figure 6.16: XENON1T sensitivity at 90% CL in terms of number of events in the exposure of 2 tonne·years, obtained with the Profile Likelihood approach, using the CL_s method, assuming a **"flat"** $\mathcal{L}_{eff}$ model (blue curve for the median and filled areas for the error bands). The result (median) of the computation under the standard "gaussian" $\mathcal{L}_{eff}$ model is superimposed in the red dashed curve.

solution from different aspects. On one hand, its implementation is not computationally too expensive, since it relies on only one nuisance parameter, t. On the other hand, the most appropriate description of $\mathcal{L}_{eff}$, based on the current knowledge, seems to be with a gaussian model above 3 keV (constrained by direct measurements) and uniform below 3 keV. We have seen that the flat parametrization sets the same limits with respect the gaussian one for $m_\chi \gtrsim 20$ GeV/c^2, that is in the region where systematics has a nearly negligible impact (see figures 6.11 and 6.12). At low masses, where the impact of $\mathcal{L}_{eff}$ uncertainty is much more relevant because the main part of WIMP energy spectra fall in the range of complete ignorance on $\mathcal{L}_{eff}$, the "flat" case sets more conservative limits. Therefore, the usage of the "flat" $\mathcal{L}_{eff}$ model allows to reproduce the proper behavior both at low WIMP masses, dominated by the complete lack of knowledge on $\mathcal{L}_{eff}$ (uniform uncertainty) and also at high masses (gaussian uncertainty).

Sensitivity as a function of the exposure

Using the Profile Likelihood we calculated the sensitivity, for WIMP mass $m_\chi = 50$ GeV/c^2, where the best limit is set (see figure 6.17), as a function of the exposure time of the experiment. Figure 6.18 shows the evolution of the estimated sensitivity of XENON1T with the livetime assuming a fiducial mass equal to 1 tonne.

A variation in the exposure changes both the signal and background expectation values. For very small exposures the expected background is very close to zero, hence the majority of the generated toy experiments has zero events, and the resulting upper limit is just a linear scaling with the exposure. Instead, for a large livetime the increasing background expectation value

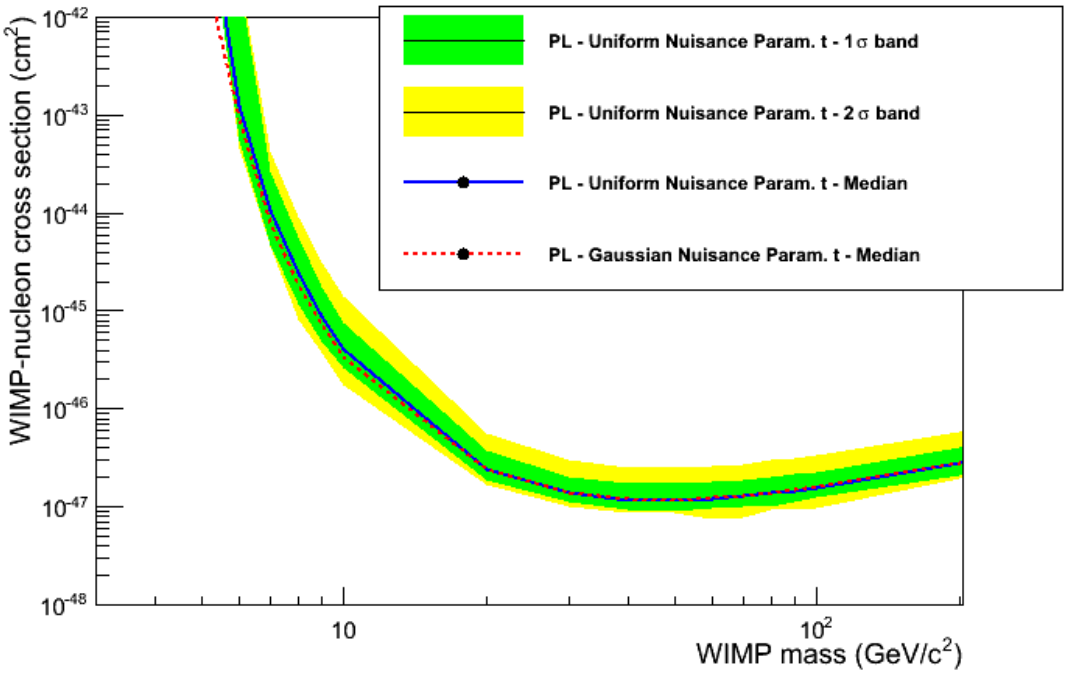

Figure 6.17: XENON1T sensitivity at 90% confidence level in terms of WIMP-nucleon cross section. The limits from the "flat" $\mathcal{L}_{eff}$ model (blue line) are slightly weaker with respect to the "gaussian" $\mathcal{L}_{eff}$ model (red dashed line).

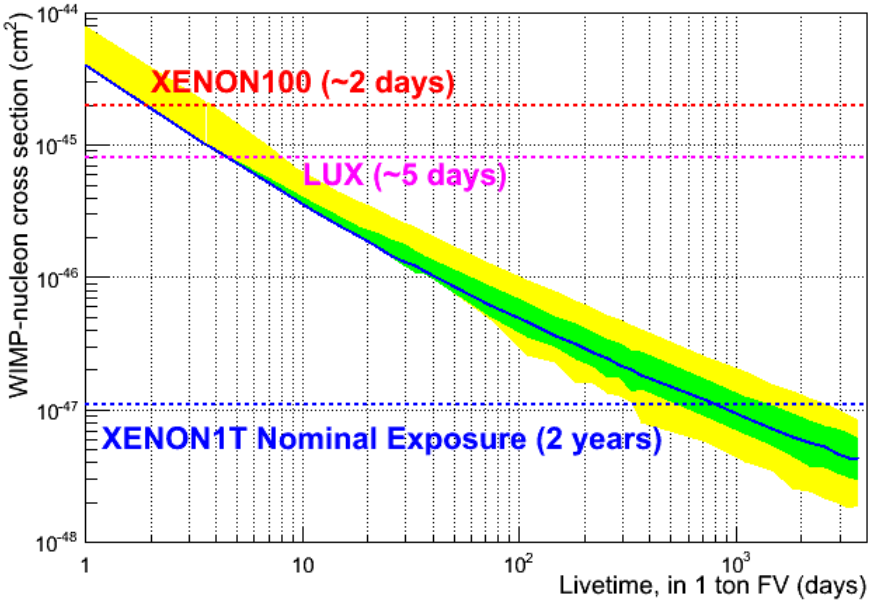

Figure 6.18: Expected XENON1T sensitivity at 90% CL, with CL_s, as a function of the exposure livetime assuming the canonical 1 tonne fiducial mass. The red (XENON100) and pink (LUX) horizontal lines marks the maximal sensitivity value achieved by the two experiments.

limits the sensitivity, even though the expected signal also grows.

With the results obtained in our study, we find that XENON1T will reach the XENON100 sensitivity (2×10^{-45} cm^2) after 1.8 days and will overcome the current world's best limit set by LUX (7.6×10^{-46} cm^2) after about five live-days of data acquisition.

Summary and conclusions (and beyond)

The XENON1T experiment marks a significant step forward for the direct Dark Matter search. The current strongest limits on the spin-independent WIMP-nucleon cross section have been set by LUX in 2013, improving the previous limit of XENON100 by a factor ~ 2.5, with a minimum of 7.6×10^{-46} cm^2 at 33 GeV/c^2 WIMP mass. Thanks to a 30 times larger target mass than XENON100, to a careful screening of the construction materials and to a variety of methods to purify the LXe from intrinsic contaminants, the background level is strongly reduced; and the ambitious goal of XENON1T to improve by two orders of magnitude the current limits can be achieved.

Indeed detailed MC simulations of the detector geometry, as well as dedicated measurements of the material radioactivity and estimations of the xenon purity, allowed to accurately predict the expected background; the results are consistent with the XENON1T aim:

- ER background: 129 ± 11 events per year,
- NR background: 1.9 ± 0.4 events per year

in 1 tonne fiducial volume.

Combining the background information with the calculation of the WIMP recoil energy spectra, we defined the bi-dimensional XENON1T statistical model based on the signal and backgrounds (ER and NR) distributions in the two observables S1, the primary scintillation signal, and Y, an idealized discrimination parameter. The statistical analysis of simulated data samples through likelihood-based hypothesis tests allows to keep inside the analysis all the ER events instead of removing them with a hard discrimination cut (as it is done in the Maximum Gap method), thus enhancing the power of the statistical inference.

We performed the study of the XENON1T sensitivity in rejecting WIMP hypotheses with the Likelihood Ratio and the Profile Likelihood method. In the first case no systematics are taken into account, while using the PL approach we profiled out the main systematic uncertainty, namely the relative scintillation efficiency ($\mathcal{L}_{eff}$) for NR, whose measurement is experimentally challenging especially in the very low energy region.

We compared the LR sensitivity with the result of the Maximum Gap study (both methods do not take care of systematics) finding, not surprisingly, improved limits by a factor 1.7 at large WIMP masses, while they converge in the low mass range.

As expected, the PL limits are always weaker than those obtained with the LR, with a remarkable discrepancy at low WIMP masses, where systematics play a dominant role.

The impact of the $\mathcal{L}_{eff}$ uncertainty on the model has been carefully studied introducing a nuisance parameter and evaluating how the expectation value and the spectral shape of both the signal and the NR background vary under different $\mathcal{L}_{eff}$ values. We initially assumed the canonical gaussian parametrization of the uncertainty on the $\mathcal{L}_{eff}$ curve. Nonetheless, below 3 keV no direct measurements are available so far, hence any choice for $\mathcal{L}_{eff}$ in this region is arbitrary. The most conservative assumption is a flat distribution, meaning that all values are equally probable. We performed the PL calculation of the sensitivity under the most penalizing parametrization: uniform distribution of $\mathcal{L}_{eff}$ between the canonical 2σ boundary curves. We found that such a choice exactly reproduces the previous results for large WIMP masses, implying that the flat assumption is substantially equivalent to the gaussian one above 3 keV. At low masses, instead, the limits worsen. Thus we decided to use as final result the limits obtained with the flat parametrization, being more conservative at low masses, and equal to the gaussian one at high masses.

The exclusion limits are computed using the CL_s method, which is basically a protection against the possibility to set too optimistic limits, widely used also in the LHC experiments. Thus, in the final chapter, we also showed the results without the conservative CL_s method, which are slightly better, as one would expect given the over-coverage property of CL_s. Moreover, we carried out the sensitivity study using the alternative test statistic $\tilde{q}_\mu$. The results do not differ from those achieved with q_μ.

The conclusive result for the expected sensitivity of the XENON1T experiment for a 2 tonne $\cdot$ years exposure shows the minimum at

$$1.2 \times 10^{-47}\ \mathrm{cm}^2 \text{ for a WIMP mass of } 50\ \mathrm{GeV}/c^2\ ,$$

which corresponds to the goal of a factor 100 improvement of the XENON100 performance. The XENON1T sensitivity curve is plotted in figure 6.19 along with the exclusion limits set by the main Dark Matter experiments. As one can see, XENON1T will provide the world's best constraints on the WIMP-nucleon cross section within the next two years. According to such sensitivity estimate, XENON1T will be able to overcome the LUX limits after about 5 days of exposure and 1 tonne fiducial volume.

Next generation experiments with even larger target masses than XENON1T, up to the order of 20 tonnes, are in project: XENONnT, LUX-Zeplin (LZ) [120] and DARWIN [121]. Their aim is to cover the entire WIMP parameter space, down to the neutrino bound (dashed line in figure 6.19).

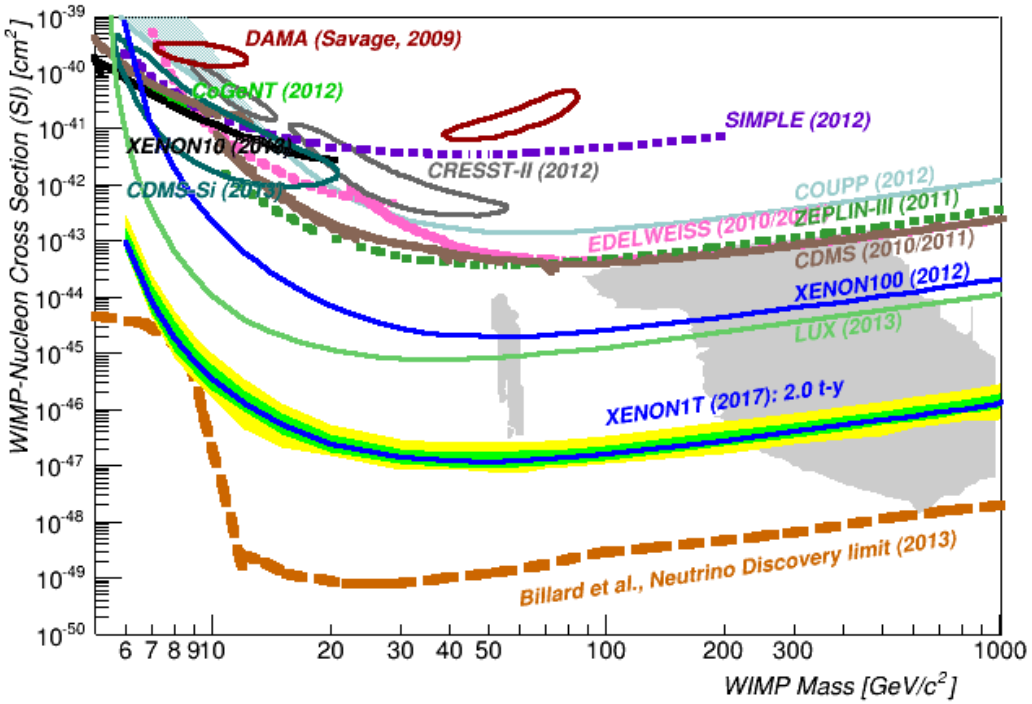

Figure 6.19: Scenario of the sensitivities, at 90% CL from different DM experiments. The more relevant are: DAMA exclusion regions [50] (dark red), XENON100 [27] (blue) and LUX [28] (green). The result of the present work for the XENON1T sensitivity (yellow and green bands with the solid blue curve inside) evaluated with the Profile Likelihood ratio method for a 2 tonne·years exposure is also reported.

The work developed in this thesis will be used to calculate the sensitivity of the future experiments of the XENON project: assuming some reference values for the diffused background in LXe and background stemming from materials, we will study in detail the expected exclusion limits that will be reached with XENONnT and DARWIN. The neutrino backgrounds (both ER and NR) will be studied with particular attention since they will be dominant for the ultimate experiment DARWIN (about 20 tonnes of LXe).

Concerning the XENON1T experiment, further extensions of the sensitivity study will be devoted to the optimization of the fiducial volume in order to maximize the sensitivity; this will be achieved by adding the position of the interaction of signal and backgrounds directly as an observable in the Profile Likelihood analysis.

Bibliography

[1] F. Zwicky. The coma cluster of galaxies. *Publications of the Astronomical Society of the Pacific*, pages 61–71, 1951.

[2] K. G. Begeman, A. H. Broeils, and R. H. Sanders. Extended rotation curves of spiral galaxies: Dark haloes and modified dynamics. *Monthly Notices of the Royal Astronomical Society*, 249(3):523–537, 1991.

[3] J. F. Navarro, C. S. Frenk, and S. D. M. White. The structure of cold dark matter halos. *The Astrophysical Journal*, 462:563, 1996.

[4] D. Clowe, A. Gonzalez, and M. Markevitch. Weak lensing mass reconstruction of the interacting cluster 1E0657-558: Direct evidence for the existence of dark matter. *The Astrophysical Journal*, 604(2):596, 2004.

[5] C. Alcock et al. The macho project: microlensing results from 5.7 years of large magellanic cloud observations. *The Astrophysical Journal*, 542(1):281, 2000.

[6] A. A. Penzias and R. W. Wilson. A measurement of excess antenna temperature at 4080 mc/s. *The Astrophysical Journal*, 142:419–421, 1965.

[7] C. L. Bennett et al. Nine-year wilkinson microwave anisotropy probe (wmap) observations: final maps and results. *The Astrophysical Journal Supplement Series*, 208(2):20, 2013.

[8] R. K. Sachs and A. M. Wolfe. Perturbations of a cosmological model and angular variations of the microwave background. *The Astrophysical Journal*, 147:73, 1967.

[9] P. A. R. Ade et al. Planck 2013 results. xv. cmb power spectra and likelihood. *Astronomy & Astrophysics*, 571:A15, 2014.

[10] O. Lahav and A. R. Liddle. The cosmological parameters 2014. *arXiv:1401.1389 [astro-ph.CO]*.

[11] W. de Boer et al. Egret excess of diffuse galactic gamma rays interpreted as a signal of dark matter annihilation. *arXiv preprint astro-ph/0602325*, 2006.

[12] J. P. Ostriker and P. J. Peebles. A numerical study of the stability of flattened galaxies: or, can cold galaxies survive? *The Astrophysical Journal*, 186:467–480, 1973.

[13] S. Riemer-Sørensen, D. Parkinson, and T. M. Davis. Combining planck data with large scale structure information gives a strong neutrino mass constraint. *Physical Review D*, 89(10):103505, 2014.

[14] J. R. Bond and A. S. Szalay. The collisionless damping of density fluctuations in an expanding universe. *The Astrophysical Journal*, 274:443–468, 1983.

[15] R. D Peccei and H. R. Quinn. Cp conservation in the presence of pseudoparticles. *Physical Review Letters*, 38(25):1440, 1977.

[16] M. S. Turner. Cosmic and local mass density of "invisible" axions. *Physical Review D*, 33(4):889, 1986.

[17] K. Zioutas et al. First results from the cern axion solar telescope. *Physical review letters*, 94(12):121301, 2005.

[18] E. Zavattini et al. New pvlas results and limits on magnetically induced optical rotation and ellipticity in vacuum. *Physical Review D*, 77(3):032006, 2008.

[19] E. Aprile et al. First axion results from the xenon100 experiment. *Physical Review D*, 90(6):062009, 2014.

[20] G. Jungman, M. Kamionkowski, and K. Griest. Supersymmetric dark matter. *Physics Reports*, 267(5):195–373, 1996.

[21] P. Gondolo. Phenomenological introduction to direct dark matter detection. *arXiv preprint hep-ph/9605290*, 1996.

[22] M. W. Goodman and E. Witten. Detectability of certain dark-matter candidates. *Physical Review D*, 31(12):3059, 1985.

[23] T. Moroi, H. Murayama, and M. Yamaguchi. Cosmological constraints on the light stable gravitino. *Physics Letters B*, 303(3):289–294, 1993.

[24] M. Bolz, A. Brandenburg, and W. Buchmüller. Thermal production of gravitinos. *Nuclear Physics B*, 606(1):518–544, 2001.

[25] V. Berezinsky, M. Kachelriess, and A. Vilenkin. Ultrahigh energy cosmic rays without greisen-zatsepin-kuzmin cutoff. *Physical Review Letters*, 79(22):4302, 1997.

[26] H. Cheng, J. L. Feng, and K. T. Matchev. Kaluza-klein dark matter. *Physical Review Letters*, 89(21):211301, 2002.

[27] E. Aprile et al. (XENON100). Dark matter results from 225 live days of xenon100 data. *Phys. Rev. Lett.*, 109(181301), 2012.

[28] D. S. Akerib et al. (LUX Collaboration). First results from the lux dark matter experiment at the sanford underground research facility. *Phys. Rev. Lett.*, 112(091303), 2014.

[29] R. Bernabei et al. The annual modulation signature for dark matter: Dama/libra-phase1 results and perspectives. *Advances in High Energy Physics*, 2014, 2014.

[30] K. Blum. Dama vs. the annually modulated muon background. *arXiv preprint arXiv:1110.0857*, 2011.

[31] R. Bernabei et al. No role for muons in the dama annual modulation results. *European Physical Journal C-Particles and Fields*, 72(7):1, 2012.

[32] S. Chang, J. Liu, A. Pierce, N. Weiner, and I. Yavin. Cogent interpretations. *Journal of Cosmology and Astroparticle Physics*, 2010(08):018, 2010.

[33] C. E. Aalseth et al. Search for an annual modulation in three years of cogent dark matter detector data. *arXiv preprint arXiv:1401.3295*, 2014.

[34] E. Armengaud et al. Search for low-mass wimps with edelweiss-ii heat-and-ionization detectors. *Physical Review D*, 86(5):051701, 2012.

[35] R. Agnese et al. Search for low-mass weakly interacting massive particles with supercdms. *Physical review letters*, 112(24):241302, 2014.

[36] G. Angloher et al. Results on low mass wimps using an upgraded cresst-ii detector. *The European Physical Journal C*, 74(12):1–6, 2014.

[37] G. Angloher et al. Results from 730 kg days of the cresst-ii dark matter search. *The European Physical Journal C-Particles and Fields*, 72(4):1–22, 2012.

[38] A. Brown, S. Henry, H. Kraus, and C. McCabe. Extending the cresst-ii commissioning run limits to lower masses. *Physical Review D*, 85(2):021301, 2012.

[39] R. Agnese et al. Search for low-mass weakly interacting massive particles using voltage-assisted calorimetric ionization detection in the supercdms experiment. *Physical review letters*, 112(4):041302, 2014.

[40] R. Agnese et al. Silicon detector dark matter results from the final exposure of cdms ii. *Physical Review Letters*, 111(25):251301, 2013.

[41] C. E. Aalseth et al. Cogent: A search for low-mass dark matter using p-type point contact germanium detectors. *Physical Review D*, 88(1):012002, 2013.

[42] C. Savage, G. Gelmini, P. Gondolo, and K. Freese. Compatibility of dama/libra dark matter detection with other searches. *Journal of Cosmology and Astroparticle Physics*, 2009(04):010, 2009.

[43] A. Gütlein. Feasibility study for a first observation of coherent neutrino nucleus scattering using low-temperature detectors. 2013.

[44] E. Armengaud et al. Final results of the edelweiss-ii wimp search using a 4-kg array of cryogenic germanium detectors with interleaved electrodes. *Physics Letters B*, 702(5):329–335, 2011.

[45] Z. Ahmed et al. Results from the final exposure of the cdms ii experiment. *arXiv preprint arXiv:0912.3592*, 2009.

[46] D. Akimov et al. Wimp-nucleon cross-section results from the second science run of zeplin-iii. *Physics Letters B*, 709(1):14–20, 2012.

[47] J. Angle et al. Search for light dark matter in xenon10 data. *Physical Review Letters*, 107(5):051301, 2011.

[48] E. Aprile et al. Dark matter results from 100 live days of xenon100 data. *Physical Review Letters*, 107(13):131302, 2011.

[49] Z. Ahmed et al. Results from a low-energy analysis of the cdms ii germanium data. *Physical Review Letters*, 106(13):131302, 2011.

[50] R. Bernabei et al. First results from dama/libra and the combined results with dama/nai. *The European Physical Journal C-Particles and Fields*, 56(3):333–355, 2008.

[51] DM Tools Limit Plotter. *http://dmtools.brown.edu:8080*.

[52] E. Aliu et al. Veritas deep observations of the dwarf spheroidal galaxy segue 1. *arXiv preprint arXiv:1202.2144*, 2012.

[53] T. Tanaka et al. An indirect search for weakly interacting massive particles in the sun using 3109.6 days of upward-going muons in super-kamiokande. *The Astrophysical Journal*, 742(2):78, 2011.

[54] G. Wikström and J. Edsjö. Limits on the wimp-nucleon scattering cross-section from neutrino telescopes. *Journal of Cosmology and Astroparticle Physics*, 2009(04):009, 2009.

[55] R. Abbasi et al. Limits on a muon flux from neutralino annihilations in the sun with the icecube 22-string detector. *Physical review letters*, 102(20):201302, 2009.

[56] G. Ingelman and M. Thunman. High energy neutrino production by cosmic ray interactions in the sun. *Physical Review D*, 54(7):4385, 1996.

[57] C. Rott, K. Kohri, and S. C. Park. Superheavy dark matter and icecube neutrino signals: bounds on decaying dark matter. *arXiv preprint arXiv:1408.4575*, 2014.

[58] R. Abbasi et al. Search for dark matter from the galactic halo with the icecube neutrino telescope. *Physical Review D*, 84(2):022004, 2011.

[59] M. Aguilar et al. Electron and positron fluxes in primary cosmic rays measured with the alpha magnetic spectrometer on the international space station. *Physical review letters*, 113(12):121102, 2014.

[60] O. Adriani et al. Pamela results on the cosmic-ray antiproton flux from 60 mev to 180 gev in kinetic energy. *Physical Review Letters*, 105(12):121101, 2010.

[61] Q.-H. Cao, C.-R. Chen, and T. Gong. Leptophilic dark matter and ams-02 cosmic-ray positron flux. *arXiv preprint arXiv:1409.7317*, 2014.

[62] E. Aprile et al. Design and performance of the xenon10 dark matter experiment. *Astroparticle Physics*, 34(9):679–698, 2011.

[63] E. Aprile et al. The xenon100 dark matter experiment. *Astroparticle Physics*, 35(9):573–590, 2012.

[64] E. Aprile et al. Limits on spin-dependent wimp-nucleon cross sections from 225 live days of xenon100 data. *Physical review letters*, 111(2):021301, 2013.

[65] E. Aprile. The xenon1t dark matter search experiment. In *Sources and Detection of Dark Matter and Dark Energy in the Universe*, pages 93–96. Springer, 2013.

[66] E. Aprile and T. Doke. Liquid xenon detectors for particle physics and astrophysics. *Reviews of Modern Physics*, 82(3):2053, 2010.

[67] E. Aprile, K. L. Giboni, P. Majewski, K. Ni, and M. Yamashita. Observation of anticorrelation between scintillation and ionization for mev gamma rays in liquid xenon. *Physical Review B*, 76(1):014115, 2007.

[68] J. Angle et al. First results from the xenon10 dark matter experiment at the gran sasso national laboratory. *Physical Review Letters*, 100(2):021303, 2008.

[69] D. S. Akerib et al. Limits on spin-independent interactions of weakly interacting massive particles with nucleons from the two-tower run of the cryogenic dark matter search. *Physical review letters*, 96(1):011302, 2006.

[70] J. Angle et al. Limits on spin-dependent wimp-nucleon cross sections from the xenon10 experiment. *Physical review letters*, 101(9):091301, 2008.

[71] A. Fowlie et al. Constrained mssm favoring new territories: The impact of new lhc limits and a 125 gev higgs boson. *Physical Review D*, 86(7):075010, 2012.

[72] Z. Ahmed et al. Search for weakly interacting massive particles with the first five-tower data from the cryogenic dark matter search at the soudan underground laboratory. *Phys. Rev. Lett*, 102(011301):0802–3530, 2009.

[73] M. Aglietta et al. Muon "depth-intensity" relation measured by the lvd underground experiment and cosmic-ray muon spectrum at sea level. *Physical Review D*, 58(9):092005, 1998.

[74] M. Ambrosio et al. Measurement of the residual energy of muons in the gran sasso underground laboratories. *Astroparticle physics*, 19(3):313–328, 2003.

[75] E. Aprile et al. Conceptual design and simulation of a water cherenkov muon veto for the xenon1t experiment. *Journal of Instrumentation*, 9(11):P11006, 2014.

[76] J. Neyman and E. S. Pearson. On the problem of the most efficient tests of statistical hypotheses. *Royal Society of London Philosophical Transactions Series A*, 231:289–337, 1933.

[77] J. Neyman and E. S. Pearson. The testing of statistical hypotheses in relation to probabilities a priori. In *Mathematical Proceedings of the Cambridge Philosophical Society*, volume 29, pages 492–510. Cambridge Univ Press, 1933.

[78] S. Brandt. Datenanalyse, bi-wiss. *Verlag, dritte Auflage*, 1992.

[79] E. Aprile et al. Likelihood approach to the first dark matter results from xenon100. *Physical Review D*, 84(5):052003, 2011.

[80] G. Cowan, K. Cranmer, E. Gross, and O. Vitells. Asymptotic formulae for likelihood-based tests of new physics. *The European Physical Journal C-Particles and Fields*, 71(2):1–19, 2011.

[81] A. L. Read. Presentation of search results: the cls technique. *Journal of Physics*, G28(10):2693, 2002.

[82] T. Junk. Confidence level computation for combining searches with small statistics. *Nuclear Instruments and Methods in Physics Research*, A434(2):435–443, 1999.

[83] L. Moneta et al. The roostats project. *arXiv preprint arXiv:1009.1003*, 2010.

[84] G. Cowan. *Statistical data analysis.* Oxford University Press, 1998.

[85] W. Verkerke and D. Kirkby. The roofit toolkit for data modeling. *arXiv preprint physics/0306116*, 2003.

[86] R. Brun and F. Rademakers. Root: an object oriented data analysis framework. *Nuclear Instruments and Methods in Physics Research*, A389(1):81–86, 1997.

[87] RooStats Web. *https://twiki.cern.ch/twiki/bin/view/RooStats/WebHome.*

[88] J. Binney and S. Tremaine. Galactic dynamics, chap. 2, 1987.

[89] E. I. Gates, G. Gyuk, and M. S. Turner. The local halo density. *The Astrophysical Journal Letters*, 449(2):L123, 1995.

[90] F. J. Kerr and D. Lynden-Bell. Review of galactic constants. *Monthly Notices of the Royal Astronomical Society*, 221(4):1023–1038, 1986.

[91] J. L. Feng, J. Kumar, D. Marfatia, and D. Sanford. Isospin-violating dark matter. *Physics Letters B*, 703(2):124–127, 2011.

[92] J. D. Lewin and P. F. Smith. Review of mathematics, numerical factors, and corrections for dark matter experiments based on elastic nuclear recoil. *Astroparticle Physics*, 6(1):87–112, 1996.

[93] F. Donato, N. Fornengo, and S. Scopel. Effects of galactic dark halo rotation on wimp direct detection. *Astroparticle Physics*, 9(3):247–260, 1998.

[94] I. D. Karachentsev and D. I. Makarov. Orbital velocity of the sun and the apex of the galactic center. *Astronomy Letters*, 22:455–458, 1996.

[95] R. H. Helm. Inelastic and elastic scattering of 187-mev electrons from selected even-even nuclei. *Physical Review D*, 104(5):1466, 1956.

[96] J. Engel. Nuclear form factors for the scattering of weakly interacting massive particles. *Physics Letters B*, 264(1):114–119, 1991.

[97] DMMC tool (J. Gascon, V. Sanglard IPN Lyon, and R. Lemrani CEA Saclay). *http://pisrv0.pit.physik.uni-tuebingen.de/darkmatter/spectra/index.php.*

[98] S. Agostinelli et al. Geant4 - a simulation toolkit. *Nuclear Instruments and Methods in Physics Research*, A506(3):250–303, 2003.

[99] F. V. Massoli. *The XENON1T experiment: Monte Carlo background estimation and sensitivity curves study.* PhD thesis, Alma Mater Studiorum - University of Bologna, 2015.

[100] E. Aprile et al. Conceptual design and simulation of a water cherenkov muon veto for the xenon1t experiment. *Journal of Instrumentation*, 9(11):P11006, 2014.

[101] W. B. Wilson et al. Sources-4a. Technical report, Technical Report LA-13639-MS, Los Alamos, 1999.

[102] W. B. Wilson, R. T. Perry, W. S. Charlton, T. A. Parish, and E. F. Shores. Sources: a code for calculating (α, n), spontaneous fission, and delayed neutron sources and spectra. *Radiation protection dosimetry*, 115(1-4):117–121, 2005.

[103] J. Billard, E. Figueroa-Feliciano, and L. Strigari. Implication of neutrino backgrounds on the reach of next generation dark matter direct detection experiments. *Physical Review D*, 89(2):023524, 2014.

[104] M. Szydagis et al. Nest: a comprehensive model for scintillation yield in liquid xenon. *Journal of Instrumentation*, 6(10):P10002, 2011.

[105] M. Szydagis et al. Enhancement of nest capabilities for simulating low-energy recoils in liquid xenon. *Journal of Instrumentation*, 8(10):C10003, 2013.

[106] E. Aprile et al. Response of the xenon100 dark matter detector to nuclear recoils. *Physical Review D*, 88(1):012006, 2013.

[107] A. Hitachi. Properties of liquid xenon scintillation for dark matter searches. *Astroparticle Physics*, 24(3):247–256, 2005.

[108] J Lindhard and M Scharff. Energy dissipation by ions in the kev region. *Physical Review*, 124(1):128, 1961.

[109] F. Arneodo et al. Scintillation efficiency of nuclear recoil in liquid xenon. *Nuclear Instruments and Methods in Physics Research*, A449(1):147–157, 2000.

[110] D. Akimov et al. Measurements of scintillation efficiency and pulse shape for low energy recoils in liquid xenon. *Physics Letters B*, 524(3):245–251, 2002.

[111] E. Aprile et al. Scintillation response of liquid xenon to low energy nuclear recoils. *Physical Review D*, 72(7):072006, 2005.

[112] V. Chepel et al. Scintillation efficiency of liquid xenon for nuclear recoils with the energy down to 5kev. *Astroparticle Physics*, 26(1):58–63, 2006.

[113] E. Aprile et al. New measurement of the relative scintillation efficiency of xenon nuclear recoils below 10 kev. *Physical Review C*, 79(4):045807, 2009.

[114] A. Manzur et al. Scintillation efficiency and ionization yield of liquid xenon for monoenergetic nuclear recoils down to 4 kev. *Physical Review C*, 81(2):025808, 2010.

[115] G. Plante et al. New measurement of the scintillation efficiency of low-energy nuclear recoils in liquid xenon. *Physical Review C*, 84(4):045805, 2011.

[116] E. Aprile et al. Observation and applications of single-electron charge signals in the xenon100 experiment. *Journal of Physics G: Nuclear and Particle Physics*, 41(3):035201, 2014.

[117] D. Drijard, W. T. Eadie, F. E. James, M. G. W. Roos, and B. Sadoulet. *Statistical methods in experimental physics*. North Holland, 1971.

[118] S. Yellin. Finding an upper limit in the presence of unknown background. *Phys. Rev.*, D66:032005, 2002.

[119] W. A. Rolke, A. M. Lopez, and J. Conrad. Limits and confidence intervals in the presence of nuisance parameters. *Nuclear Instruments and Methods in Physics Research*, A551(2):493–503, 2005.

[120] D. C. Malling et al. After lux: the lz program. *arXiv preprint arXiv:1110.0103*, 2011.

[121] L. Baudis et al. Darwin dark matter wimp search with noble liquids. In *Journal of Physics: Conference Series*, volume 375, page 012028. IOP Publishing, 2012.